X-ray spectra of highly magnetized neutron stars in binary systems

Dissertation
zur Erlangung des Grades eines
Doktors der Naturwissenschaften
der Fakultät für Mathematik und Physik
der Eberhard-Karls-Universität Tübingen

vorgelegt von

Ingo Kreykenbohm

aus Weingarten
2004

Selbstverlegt von: I. Kreykenbohm, Falkenweg 14, 72076 Tübingen
Tag der mündlichen Prüfung: 23. Juni 2004
Dekan: Prof. Dr. H. Müther
1. Berichterstatter: Prof. Dr. R. Staubert
2. Berichterstatter: Prof. Dr. K. Werner

Erweiterte deutsche Zusammenfassung

Kreykenbohm, Ingo

Hochenergie Spektren akkretierender Neutronensterne

Akkretierende Neutronensterne waren schon seit ihrer Entdeckung rätselhafte Objekte. Obwohl schon die Tatsache an sich, daß ein Stern mit gerademal der Größe einer kleinen Stadt (Radius $\sim$10 km) und einer Masse von mindestens $1.4\,M_\odot$ in höchsten Maße erstaunlich ist, wurden im Laufe der Zeit noch weitere bemerkenswerte Tatsachen über sie bekannt.

Wenn ein Neutronenstern mit einem normalen Stern ein Doppelsternsystem bildet, kann er Material von seinem Begleiter akkretieren (siehe Abschnitt 2.3). Da das Gravitationspotential des Neutronensterns sehr tief ist, wird das Material beim Fall auf den Neutronenstern stark beschleunigt. Die kinetische Energie wird beim Aufprall auf die Oberfläche des Neutronensterns in Form von Röntgenstrahlung freigesetzt. Daher werden solche Systeme Röntgendoppelsterne genannt. Wie es überhaupt zur Entstehung von Neutronensternen und insbesondere natürlich Röntgendoppelsternen kommt, ist daher Thema des Kapitels 2.

Die Entdeckung von Pulsationen bewies, daß die Neutronensterne sehr schnell rotieren: der am schnellsten rotierende Pulsar PSR 1937+21 hat eine Periode von 1.5 ms (Ashworth et al. 1983) – nur wenig oberhalb der Stabilitätsgrenze, bevor der Neutronstern durch die Zentrifugalkraft förmlich zerrissen wird. Die Pulsationen zeigten aber auch, daß die Strahlung nicht gleichmäßig auf der ganzen Oberfläche entsteht, sondern in ein oder zwei “hot spots”. Diese Erkenntnis wiederum deutete auf eine weitere bemerkenswerte Eigenschaft von Neutronensternen hin: Neutronensterne haben Magnetfelder mit einer Stärke von $\sim 10^{12}$ G.

Das Magnetfeld ist stark genug, um den Akkretionsstrom aufzubrechen. Das Material koppelt an die Magnetfeldlinien und wird entlang dieser zu den magnetischen Polen geleitet. Dort entstehen dann zwei hot spots.

Obwohl die ungefähre Stärke der Magnetfelder aufgrund theoretischer Überlegungen schon länger auf ungefähr 10^{12} G geschätzt wurde, so fehlte doch bis Mitte der 70er Jahre noch ein direkter Beweis. 1976 gelang Trümper et al. (1978) die Beobachtung einer Zyklotronresonanzlinie (engl. Cyclotron resonant scattering feature, kurz CRSF) im Spektrum von Herkules X-1. Zyklotronresonanzlinien entstehen durch die Quantisierung der Bewegungsenergie der Elektronen in starken Magnetfeldern; d.h. die Energie der Elektronen kann keine beliebigen Werte mehr annehmen, sondern nur noch vielfache der Zyklotronenergie: sie können sich nur noch auf so genannte Landau Niveaus aufhalten. Da Photonen mit $E_\mathrm{C} = h\nu$ fast instantan von einem Elektron absorbiert werden, haben sie eine extrem kleine freie Weglänge und können das Plasma im Entstehungsgebiet der Röntgenstrahlung quasi nicht verlassen. Sie können das Plasma also nur verlassen, wenn sich ihre Energie aufgrund von zahllosen Streuprozessen zu leicht höheren oder niedrigeren Werten verschiebt. Daher bildet sich im Spektrum bei der Zyklotronenergie eine Art Absorptionslinie aus. Anhand einer solchen Zyklotronresonanzlinie läßt sich mittels der 12–B–12 Regel direkt auf die Stärke des zugrunde liegenden Magnetfeldes schließen:

$$E_\mathrm{C} = 11.6 \times \frac{B}{10^{12}\,\mathrm{G}}\,\mathrm{keV}.$$

Wenn nun eine Zyklotronresonanzlinie im Spektrum eines Neutronensterns beobachtet wird, kann man von der Energie der Linie unter Berücksichtigung der Gravitationsrotverschiebung von ca. 25% direkt auf die Magnetfeldstärke schließen. Natürlich können die Elektronen nicht nur den Grundzustand und den ersten angeregten Zustand, sondern auch höhere Zustände besetzen. Daher treten in den Spektren der Neutronensterne u.U. nicht nur eine, sondern mehrere Absorptionslinien ($n \times E_\mathrm{C}$) auf (sog. harmonische Linien).

Zum Zeitpunkt der Erstellung dieser Arbeit sind 16 Quellen bekannt, die zumindest eine Zyklotronabsorptionslinie zeigen (siehe Tabelle 3.1).

In dieser Arbeit werden qualitativ hochwertige Daten von dem NASA Satelliten Rossi X-ray Timing Explorer (Beschreibung siehe Kapitel 4) verwendet. Dieser Satellit zeichnet sich durch seine große spektrale Bandbreite und hohe Zeitauflösung aus. Diese Eigenschaften machen ihn somit zu einem idealen Instrument für die Beobachtung von akkretierenden Röntgenpulsaren. Ich habe Daten von Vela X-1 (siehe Kapitel 5) und GX 301$-$2 (siehe Kapitel 6) ausgewertet; in beiden Fällen handelt es sich um Neutronensterne, die Materie von ihren entwickelten supermassiven blauen Begleitern akkretieren. Die Ergebnisse dieser Analysen wurden bzw. werden in der Zeitschrift Astronmy & Astrophysics publiziert (Kreykenbohm et al. 2002a, 2004).

Im Falle von Vela X-1 widmete ich mich der Frage, ob neben der bereits bekannten Zyklotronabsorptionslinie noch eine zweite Linie existiert. Während eine Linie bei $\sim$50 keV bereits von vielen Instrumenten beobachtet worden war, so war zwar eine zweite Linie bei der Hälfte der Energie, d.h. bei $\sim$24 keV, von Kretschmar et al. (1996) und anderen beobachtet worden, von z.B. Orlandini et al. (1997) und anderen jedoch nicht. Mithilfe von Pulsphasenspektroskopie (dabei gewinnt man Spektren von einzelnen Pulsphasenabschnitten, die man separat analysiert, um so Aussagen über die Entwicklung der spektralen Parameter im Verlauf des Pulses machen zu können) gelang es mir, die Linie in einigen Phasenbreichen nachzuweisen, während sie in anderen entweder nicht vorhanden oder nicht signifikant war. Aufgrund der resultierenden Parameter und insbesondere deren Variation im Verlauf des Pulses ist verständlich, warum die Linie nicht immer beobachtet werden kann.

Im Falle von GX 301−2 war nur eine Linie bei ~37 keV (Mihara 1995) bekannt und ich konnte auch keine weitere Linie im Spektren entdecken. Mithilfe der Pulsphasenspektroskopie entdeckte ich jedoch, daß die bereits bekannte Linie im Verlauf des Pulses sehr stark variiert. Die Variationen der spektralen Parameter waren weiterhin nicht zufällig, sondern stark miteinander korreliert: in den Phasenbereichen, in denen die Zyklotronresonanzlinie am tiefsten ist, ist ihre Partialbreite (d.h. Breite geteilt durch Energie) ebenfalls am größten. Diese Korrelation ist deshalb besonders interessant, da Coburn et al. (2002) ebenfalls eine solche Korrelation fand, als er allerdings phasengemittelte Spektren von mehreren akkretierenden Röntgenpulsaren untersuchte.

Obwohl die Interpretation dieser Korrelation sehr problematisch ist, kann man doch definitiv sagen, daß die Beobachtung einer solchen Korrelation bei phasenaufgelösten Spektren den einfacheren Theorien über akkretierende Neutronensterne widerspricht und daher bisher noch unbekannte bzw. nicht berücksichtigte physikalische Prozesse stattfinden müssen.

Das letzte Kapitel widmet sich den zukünftigen Arbeiten: es ist geplant die hier vorgestellte Arbeit fortzusetzen und weitere Röntgenpulsare mit Hilfe der Pulsphasenspektroskopie anhand von Archivdaten zu untersuchen. Damit wird es möglich die besagte Korrelation auf eine statistisch breitere Basis zu stellen und detaillierter zu untersuchen. Weiterhin werden Daten des Satelliten *INTEGRAL*, der eine bis dato unerreichte spektrale Bandbreite und Energieauflösung bietet, ebenfalls herangezogen werden. *INTEGRAL* Daten werden es ermöglichen, die Variation der Zyklotronresonanzlinien weitaus detaillierter als bisher zu untersuchen.

Abstract

Kreykenbohm, Ingo

High energy spectra of accreting neutron stars

Accreting neutron stars have been enigmatic objects from the very beginning. While the very concept of an object as small as a little town (radius $\sim$10 km) having a mass of at least $1.4\,\mathrm{M}_\odot$ is already awesome in itself, more and more mysteries were revealed with time.

If such a neutron star is forming a binary system with a stellar companion, it can accrete material from its companion (see Section 2.3). Due to the depth of the gravitational well of the neutron star, the material gains tremendous speed during the accretion process. The kinetic energy is released when the material is stopped on (or close to) the surface of the neutron star in form of hard X-rays; therefore these systems are called X-ray binaries. The formation of neutron stars and binary system is therefore discussed in Chapter 2.

The discovery of pulsations proved that the neutron stars were spinning with high frequencies: the fastest rotating neutron star known nowadays is PSR 1937+21 (Ashworth et al. 1983) with a spin period of 1.5 ms, very close to the break-up frequency. The pulsations also showed that the emission is not originating from the whole surface of the neutron star, but from one or two hot spots. This again revealed another striking feature of neutron stars: magnetic fields with a strength B of the order of $\sim 10^{12}$ G.

These magnetic fields disrupt the accretion flow and funnel the material along the magnetic field lines to the magnetic poles giving rise to two hot spots.

Although the strength of the magnetic fields of neutron stars was estimated to be of the order of 10^{12} G from the very beginning, a direct observational proof was still missing. In 1976, Trümper et al. (1978) observed a cyclotron resonant scattering feature (CRSF) in the spectrum of Hercules X-1. CRSFs are due to the quantization of the kinetic energy of electrons in B-fields of the order of 10^{12} G. This means that the energy of the electrons can only have discrete values: multiples of the cyclotron energy, so called Landau levels. Since photons with $E_\mathrm{C} = h\nu$ are (almost) instantly absorbed by an electron, they have a very small mean free path, and cannot escape the X-ray formation region. The photons can only leave the plasma if their energy has changed to slightly higher or lower energies due to numerous scattering processes giving rise to an absorption line like feature in the spectrum at the cyclotron energy – a CRSF. CRSFs allow a direct estimate of the

magnetic field strength via the 12–B–12 rule:

$$E_\mathrm{C} = 11.6 \times \frac{B}{10^{12}\,\mathrm{G}}\,\mathrm{keV}.$$

If a CRSF is observed in the spectrum of a neutron star, the strength of the magnetic field can be directly assessed from the energy of the CRSF (after taking gravitational redshift into account which amounts to ~25%). As in quantum theory, the electrons can not only occupy the fundamental and first excited level, but also higher levels ($n \times E_\mathrm{C}$), giving rise to multiple absorption features (harmonic lines) in neutron star spectra.

At time of the writing of this thesis, 16 sources are known which exhibit at least one CRSF in their spectrum (see Table 3.1).

In this thesis I used high quality data from NASA's Rossi X-ray Timing Explorer (see Chapter 4) whose spectral broad band and timing capabilities make it an ideal instrument to study accreting pulsars. I analyzed data of Vela X-1 (Chapter 5) and GX 301−2 (Chapter 6), both consisting of a neutron star and an evolved blue supergiant companion. Both chapters are based on publications in Astronomy & Astrophysics (Kreykenbohm et al. 2002a, 2004).

In the case of Vela X-1, I addressed the question of the existence of a second CRSF in the spectrum. While one line at ~50 keV has been observed by many instruments, a second line at ~24 keV had been reported by Kretschmar et al. (1996), while other observers (Orlandini et al. 1997) could not detect this line. Using pulse phase resolved spectroscopy (in pulse phase resolved spectroscopy, separate spectra are derived and analyzed for individual sections of the pulse phase, thus deriving the evolution of the spectral parameters over the pulse), I was able to detect the line in some phase bins, while the line was weak (or insignificant) in other bins. The observed spectral parameters together with the variability of the line also explain why it is not always possible to detect the line.

In the case of GX 301−2, the CRSF at ~37 keV (Mihara 1995) was already well known and no secondary line could be detected. Using phase resolved spectroscopy I, however, discovered that the CRSF is strongly variable over the pulse. The variations were not random but turned out to be strongly correlated. When the CRSF is deepest, its fractional width (sigma over energy) is also largest. This is especially interesting as Coburn et al. (2002) found a similar correlation when analyzing a set of phase averaged spectra from a set of accreting X-ray pulsars.

The interpretation of this correlation, although quite difficult, allows to conclude that it is in contradiction with simple theory of accreting neutron stars and that additional physical processes must be occurring.

The last chapter 7 is dedicated to future works: using phase resolved spectroscopy of archival *RXTE* data of many more sources will allow to study the previously discussed correlation in more detail. Furthermore, data of *INTEGRAL* with its broad band spectral coverage and unprecedented energy resolution, will be used to study the variation of CRSFs over the pulse in previously unknown detail.

Contents

1 Introduction **15**

1.1 A brief history of X-ray astronomy 15

1.2 Thesis outline 16

2 X-ray Binaries **19**

2.1 Stellar Evolution of single stars 19

2.2 Binary Evolution 28

2.3 Accretion 33

2.3.1 Roche Lobe Overflow 35

2.3.2 Be Mechanism 37

2.3.3 Stellar Wind 38

3 Magnetic Fields **45**

3.1 Origin and evolution of magnetic fields in neutron stars 45

3.2 Accretion geometry 48

3.3 Pulsars 53

3.4 Cyclotron Lines 55

3.4.1 Theory 55

3.4.2 Monte Carlo Simulations 58

3.4.3 Observations 63

4 The Rossi X-ray Timing Explorer **67**

4.1 The Spacecraft 69

4.2 Instruments 70

4.2.1 *PCA* 70

4.2.2 *HEXTE* 73

4.2.3 *ASM* 76

4.3 Software 77

4.3.1 Phase resolved spectroscopy 77

5 Confirmation of two cyclotron lines in Vela X-1 81
5.1 Introduction 82
5.2 Data 83
5.3 Spectral Analysis 86
5.3.1 Spectral Models 86
5.3.2 Pulse Phase-resolved spectra 88
5.4 Summary and Discussion 101
5.4.1 The Pulse Profile 101
5.4.2 The existence of the 25 keV line 104
5.4.3 CRSFs in accreting pulsars 106

6 The variable cyclotron line in GX 301−2 109
6.1 Introduction 110
6.2 Pulse profiles 112
6.3 Phase resolved spectra 116
6.3.1 Introduction 116
6.3.2 The spectral model 117
6.3.3 Spectral fits 121
6.4 Summary and discussion 128
6.4.1 CRSF Variability 128
6.4.2 Implications of the Line variability 131
6.4.3 Summary 133

7 The Future 135
7.1 *RXTE* 136
7.2 *INTEGRAL* 137

Bibliography 141

A Fit results for Vela X-1 151
A.1 The 1998 data 152
A.2 The 2000 data 154

Acknowledgments 161

Curriculum Vitae 163

Lebenslauf 164

List of Figures

2.1 Hertzsprung-Russell Diagram 21
2.2 Evolutionary tracks in the HRD 25
2.3 The Roche Potential 29
2.4 Evolution of a massive binary system 32
2.5 Roche Lobe Overflow 36
2.6 Sketch of a Be system 38
2.7 Orbital light curve of EXO 2030+375 39
2.8 Accretion from the wind 41
2.9 Wind accretion onto a compact object 42
3.1 Boundary Layer 49
3.2 Geometry of the accretion column 51
3.3 Fan and pencil beam 52
3.4 Cyclotron scattering cross sections 59
3.5 Monte Carlo simulations 60
3.6 Monte Carlo cyclotron line profiles 62
3.7 Spectral modeling using Monte Carlo spectra 63
3.8 Cyclotron line in Her X-1 64
3.9 Spectrum of 4U 0115+63 65
4.1 Schematic of the *RXTE* spacecraft 68
4.2 The South Atlantic Anomaly 69
4.3 Schematic of a Proportional Counter Unit 71
4.4 *PCA*-Background 73
4.5 Schematic of one *HEXTE* detector 74
4.6 *HEXTE* background spectrum 75
4.7 Schematic of one camera of the ASM 77
5.1 *PCA* and *HEXTE* fit to Crab data 83
5.2 *RXTE*-*PCA* light curve of the 1998 observation 84
5.3 *RXTE*-*PCA* light-curve of the 2000 observation 85
5.4 Energy resolved pulse profiles 89
5.5 Evolution of the fit parameters over the pulse for the 1998 observation 91

5.6 Evolution of the fit parameters over the pulse for the 2000 observation 92
5.7 Folded light-curves for the 2000 data 94
5.8 Evolution of the CRSF parameters over the pulse 95
5.9 Evolution of the CRSF parameters over the pulse 96
5.10 Spectral fit to the center of the main pulse 97
5.11 Spectral fit to the fall of the main pulse 98
5.12 Spectral fit to fall of the secondary pulse 99
5.13 Folded light-curves of the 1998 data 100
5.14 Spectral fit to the rise of main pulse of the 1998 data 103
5.15 Ratio of two raw count rate spectra 105
5.16 Correlation between E_C and E_Cut 106
6.1 Folded orbital light curve 111
6.2 Sketch of the system GX 301−2/Wray 977 112
6.3 Light curve of the periastron passage 113
6.4 Energy resolved pulse profiles 115
6.5 Definition of the phase bins 117
6.6 Residuals of fits of conventional continuum models 120
6.7 Spectrum of the rise of the secondary pulse 122
6.8 Spectrum of the rise of the main pulse 126
6.9 Variation of the CRSF 127
6.10 Variation of the CRSF parameters 128
6.11 Fractioanl CRSF width versus depth 133
6.12 CRSF width versus Energy 134
7.1 Vela X-1 as seen by *INTEGRAL* 138

List of Tables

3.1 Overview of known cyclotron lines 66
5.1 *PCA* systematic errors 86
5.2 Binning of the *HEXTE* data 86
5.3 Fit results for selected phase bins of the 2000 data 102
6.1 Systematic errors 112
6.2 Parameters for the HEC and SHEC model 121
6.3 Spectral parameters for the absorbed partial covering model . 125
6.4 Spectral parameters for the reflection model 129

Chapter 1

Introduction

1.1 A brief history of X-ray astronomy

When Giacconi tried to observe X-rays from the moon during a short rocket flight in 1962 June 18 using a simple X-ray detector, he opened a completely new field of astronomy. Instead of X-rays from the moon, he discovered X-rays from somewhere in the vicinity of the Scorpius constellation (Giacconi et al. 1962) and therefore called this new X-ray source Scorpius X-1 (Sco X-1). Since the X-ray detectors available in the 1960s did not have a good spatial resolution, optical follow up observations were required to determine the exact location of the source. It took several years until Sandage et al. (1966) could finally determine the position of Sco X-1. The nature of the process capable of producing X-rays in the observed quantity were also a mystery for quite some time after the discovery of Sco X-1. Morton (1964) was the first to suggest neutron stars as a possible X-rays source, which had been a purely theoretical construct until then. The same year, Zel'dovich (1964) and Salpeter (1964) were the first to suggest that accretion of material onto a massive object (not necessarily a compact object) could be an important astrophysical energy source. In the following years, the picture of X-rays being produced by accretion of material onto a compact object became generally accepted.

As the Earth's atmosphere is opaque for hard UV- and X-rays, X-ray sources cannot be observed from the ground. In the beginning, rockets were used to carry detectors to high altitudes such that X-rays could be observed. The major draw back is that these rocket flights only last for a few minutes such that detailed studies of X-ray sources were not possible. Only a few years after the discovery of Sco X-1, the first X-ray satellite (*UHURU*, Swahili for freedom) was launched in 1970. This satellite discovered and observed over 400 X-ray sources, which were catalogued in the fourth Uhuru-catalogs (Forman et al. 1978). The nomenclature of these catalogs is still used today: a source name like 4U 1700−377 denotes fourth Uhuru catalog, followed by the position of the source in Right Ascension and Declination.

The next major step was the *Einstein* observatory which provided X-ray imaging capabilities for the first time. This allowed to study extended sources like supernova remnants and also led among others to the discovery of the "double pulsar", two normal pulsars with a spatial separation of just 20 arc minutes (Lamb et al. 1980).

About ten years later in 1990, *ROSAT* was launched. *ROSAT* provided not only excellent imaging qualities, but also allowed to create high quality spectra over the energy range 0.1–2 keV. Apart from pointed observations, *ROSAT* also performed an all sky survey resulting in the discovery of ~120 000 previously unknown sources (Aschenbach et al. 1998).

In the mid 1990s, the Rossi X-ray Timing Explorer (*RXTE*, see Chapter 4) and *BeppoSAX* (Boella et al. 1997) were launched. Both satellites offered previously unknown broad band spectral coverage from ~1 keV up to over 100 keV. While *RXTE* has supreme timing capabilities (see Chapter 4), *BeppoSAX* had excellent spectral resolution. These features allow the study of spectral and temporal behavior of X-ray sources in unprecedented detail.

The end of the millennium was characterized by two new major instruments: NASAs *Chandra* (formerly *AXAF*; Canizares 1990) and ESA's *XMM-Newton* (Mason et al. 1995). While both instruments have imaging capabilities, the spatial resolution of *Chandra* is unsurpassed in the X-rays. *XMM-Newton*, however, covers the impressive energy range from ~200 eV up to ~12 keV with excellent energy resolution and a large collecting area.

In October 2002, ESA launched the most recent major X-ray/γ-ray observatory: *INTEGRAL* (Winkler et al. 2003). *INTEGRAL* offers unprecedented broad band coverage from ~2 keV up to 10 MeV with supreme energy resolution also at high energies (better than 3 keV at 1.7 MeV for SPI; Vedrenne et al. 2003).

1.2 Thesis outline

This thesis is dedicated to the spectral analysis of two accreting X-ray pulsars (XRPs): Vela X-1 and GX 301−2. The formation process of X-ray binaries in general will be discussed to some extent in Chapter 2. After an overview of the stellar evolution (with special emphasis on binary evolution), accretion as a source of energy is discussed. This discussion also includes a description of the three main types of mass transfer between the stellar companion and the compact object. Chapter 3 then extends the discussion to magnetic fields, which have been neglected so far in this thesis. After a short introduction into the origin and evolution of the magnetic field in compact objects, the influence of the magnetic field on the accretion process is discussed, including accretion geometry and X-ray pulsars.

The last part of Chapter 3 is dedicated to a special effect observable in a highly magnetized plasma ($B \approx 10^{12}$ G): the formation of so called cyclotron lines. In this part, an introduction into the theory of cyclotron lines is given, followed by the results of Monte Carlo simulations and observations. The study of these cyclotron lines is the main objective of this thesis.

As outlined before, a prime instrument for time resolved spectroscopy is the *RXTE*, which will be introduced in greater detail in Chapter 4. *RXTE* is especially well suited for the analysis of accreting XRPs as it offers good spectral resolution together with high time resolution which is required to study cyclotron lines.

In Chapter 5, results from a detailed analysis of phase resolved spectra of the XRP Vela X-1 derived from *RXTE* data are presented. This source was known to show one cyclotron line, while the existence of a second line remained unclear. The presented analysis shows that there is indeed a line like feature present in the data, thus allowing the confirmation of the second line.

Chapter 6 is dedicated to the analysis of the XRP GX 301−2. A cyclotron line in the spectrum of GX 301−2 had been reported before, but using phase resolved spectroscopy, I discovered a strong variability of the line over the pulse.

This thesis is concluded by an outlook in Chapter 7, giving an overview of what should or can be done in the following years.

CHAPTER 2

X-ray Binaries

X-ray binaries are stellar binary systems consisting of a “normal”, e.g., main sequence star, and a compact object. The compact object can either be a white dwarf (WD), a neutron star (NS), or a black hole (or, more precisely, black hole candidate, BHC).

Under certain circumstances, which will be discussed in more detail in Section 2.3, during some phases of the evolution of the binary system, material can be transfered from the normal star to the compact object. The kinetic energy of the material is released as X-rays.

The main focus of this chapter is the formation of these X-ray binary systems and the accretion process onto the compact object. Therefore I will first discuss the evolution of single stars in general in Section 2.1 and put special emphasis on binary systems in Section 2.2. The formation of stellar remnants, especially neutron stars will also be discussed to some extent (a full discussion of this subject is way beyond the scope of this thesis). In the following section (Sect. 2.3), I will discuss the basic principles of accretion onto compact objects in binary systems. Since the classification of X-ray binaries and the different accretion types has already been discussed numerous times (see, e.g., Kuster 2003; Benlloch-Garcia 2003; Kreykenbohm 1997; Kretschmar 1996, and references therein), this Section is kept relatively short.

2.1 Stellar Evolution of single stars

The subject of stellar evolution is very complex and many epochs during the evolution of stars, especially in the beginning and near the end of the star’s life, are not very well understood and are still under discussion. It is therefore quite impossible to give a detailed overview of the complete subject in this context, however, the most basic facts shall be summarized in the following (for a more detailed overview of stellar evolution, see, e.g., Payne-Gaposchkin 1984).

At the beginning of the twentieth century, Ejnar Hertzsprung, H. Rosenberg, and three years later, also Henry Norris Russell, published a diagram showing the absolute visual magnitude of stars over their color – later known as the *Hertzsprung-Russell diagram* (HRD; Hertzsprung 1911; Rosenberg 1911). Later on, not only absolute magnitude over color but also other parameter combinations were shown, e.g., magnitude over temperature. A modern HRD of stars in the vicinity of the sun as observed by the *Hipparcos* satellite (Perryman et al. 1989) is shown in Fig. 2.1.

The most striking feature of a HRD is that the stars are *not* distributed uniformly in the magnitude/color plane. Instead, most stars are concentrated on the *main-sequence*, extending from upper left corner (bright and hot) almost down to the lower right corner (dim and cool). But not all stars are found in this relatively narrow sequence: some stars are found in the upper right region (bright, but cool) of the HRD, while also some stars are found below the main sequence. This distribution of stars is due to the evolution of the stars from their “birth” until their “death”.

Stars are “born” in gas clouds. In the beginning, an otherwise stable gas cloud starts to contract under the influence of, e.g., the shockwaves of a nearby super nova (for a discussion of molecular clouds and star forming regions, see, e.g., Genzel 1992). As the contraction of the gas cloud continues, the material is somewhat denser in some regions inside the cloud, than in average (not necessarily at the center of the cloud). At first, the density variations in the cloud are so small, that they would be more or less undetectable by our instruments. On the other hand, the particle density of such a molecular cloud (10^3 H_2-molecules per cubic centimeter) is considered a very high density (Ostriker et al. 2001). In fact, it is so high that these clouds are completely opaque for optical light (e.g., an extinction of more than 30 magnitudes in the molecular cloud W49A, Alves & Homeier 2003), but this density is still lower than in any vacuum created on Earth (one of the best vacuums has a pressure of 10^{-9} Pa corresponding to $\sim 2.5 \times 10^5$ particles per cubic centimeter). With time, however, the still subtle influence of the gravitational force is slightly stronger in these denser regions than in the remainder of the cloud. These regions will become the condensation nuclei for the future stars.

As these nuclei continue to grow in size and mass they generate internal heat – mainly due to energy deposition of the infalling material but also to some extent due to decay of radioactive elements. With increasing mass, the gravitational force also increases resulting in the accretion of more mass onto these nuclei. Due to the angular momentum present in the material (all material has some angular momentum due to, e.g., the rotation of the galaxy; sometimes the dark cloud itself is also rotating Arquilla & Goldsmith 1986), an accretion disk forms. These “stars” still do not have a definitive form, they are more like big clumps of material with radially decreasing density and temperature. At a certain point, the pressure and

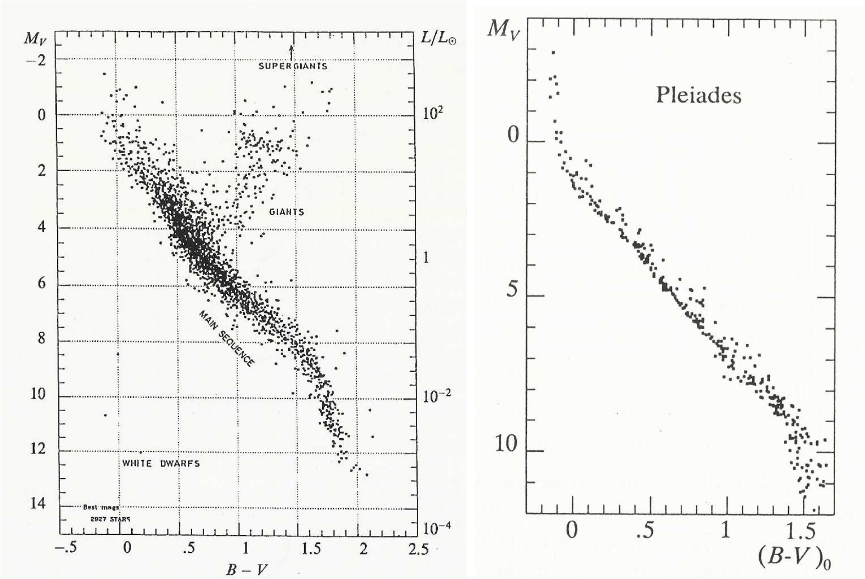

Figure 2.1: **Left**: the Hertzsprung-Russell Diagram (HRD) of stars in the vicinity of the sun. 2927 stars were observed by the *Hipparcos* satellite to construct this diagram. Most stars are found on the main sequence, where they remain for the greater part of their life. When they have used up their stellar fuel, they develop into the giants regime where they stay for a much shorter time; therefore the giant region is much less densely populated. After the giant stage the stars expel their envelope (which can be observed as a planetary nebula) and the stars move horizontally to the upper left corner and then cool down and end up in the White Dwarf regime. Since cool White Dwarfs are difficult to observe, only very few such objects are included in this diagram (figure from Lindegren 1992). **Right**: for comparison, a HRD of the very young Pleiades cluster. This open cluster is so young that almost all stars are still on the main sequence (diagram from Schatzman & Praderie 1993, p. 34). The Hayashi line is on the right border of the diagram (not shown). For a detailed discussion of HRDs, see e.g., Payne-Gaposchkin (1984) or Schatzman & Praderie (1993).

the temperature in the center of the nucleus is so high, that thermonuclear fusion becomes possible (for a more detailed discussion of star formation in molecular clouds, see, e.g., Scheffler 1988).

At this evolutionary point, the *proto-star* begins to emit radiation at first only in the infrared, later also in the optical band and thus appears on the *Hayashi line* in the HRD (see Fig. 2.1 and Hayashi 1961). This line separates the hydrogen burning stars (on the left side) from unstable, e.g., Lithium burning stars on the right side of the Hayashi line.

Since, however, these *proto-stars* are deeply embedded in the opaque gas cloud, they cannot be observed easily. (Far-)infrared radiation is, however, not absorbed by the dust and gas of the dark cloud, such that it is possible to detect these proto-stars in this energy band. As the water in the atmosphere of the Earth again prohibits observations in the infrared (and, by the way, also in the UV-, X-ray, and Gamma-ray band), these objects can only be observed by satellites, e.g. ESAs Infrared Space Observatory (ISO, Kessler et al. 1996) or the Infrared Astronomy Satellite (IRAS, Neugebauer et al. 1984). Observations using IRAS showed numerous point sources inside dark clouds (Emerson 1987; Beichmann et al. 1984, and references therein), such that not only the birth of an individual star is observed, but the birth of an entire cluster of stars.

Although most of these new stars are not very massive, the environment is definitely not calm. Instead, these young proto-stars interact strongly with their environment. The increasing radiation pressure soon separates the proto star from the molecular cloud by “boiling” the material in vicinity of the star away. Such young stars are called *T-Tauri stars* (named, as usually, after T Tauri, the first star of this group). These stars show strong material outflows and an intense stellar wind. This wind again interacts with the surrounding material of the gas cloud, compressing the medium and causing shock fronts. These fronts again give rise to the formation of even more condensation nuclei which eventually might also form proto-stars.

Apart from low mass stars, also a few massive stars are born in these clouds (e.g., the massive B2 protostar G34.4+0.23 MM in IRAS 18507+0121 Shepherd et al. 2003). Since these stars are more massive, they are also hotter; therefore they have their radiation maximum in the UV band (van Paradijs & McClintock 1995, p. 70). This very intense UV radiation boils not only the material in the vicinity of the star away, but also all the material of the gas cloud itself. This process was observed, e.g., by the Hubble Space Telescope (HST) in M16 (see `http://hubblesite.org/newscenter/archive/1995/44/image/a`).

Eventually, all the gas of the gas cloud is either condensated and has formed stars or is evaporated into the interstellar medium (ISM). Finally, a new stellar open cluster is born. An example for such an open cluster are the Pleiades which is a very young stellar cluster, that still contains lots of material that is illuminated by the hot young stars (see `http://www.cv.nrao.edu/~pmurphy/images/astro/pleiades.png`). Although usually only the massive bright stars can be seen (as in the Pleiades), these clusters contain many more low mass stars (Adams et al. 2001), which are mostly too dim to be seen easily.

The T-Tauri stars evolve very rapidly (on the astronomical timescale, that is, in some thousand years): they first appear in the HRD on the Hayashi line as infrared emitter, but evolve quickly in the direction of the main sequence. Thousands of these young stars are known today in our galaxy and all of these stars are found close to dark clouds indicating their place of birth. Since the evolution timescales are very short and the T-Tauri stars are usually also still (somewhat) enshrouded in the molecular cloud and are thus hidden from normal telescopes, they are difficult to observe.

After the star has used up all its lithium, beryllium, and boron, it now burns hydrogen and the star moves towards the main sequence. Once the (former T-Tauri) star has reached the main sequence, it will stay there for a very long time: at least millions of years; stars like the sun for about nine billion years, low mass stars even ten times as long as our sun (minimum mass for the onset of the hydrogen burning is about $0.07\,\mathrm{M}_\odot$; Voigt 1991, p. 265). This so called nuclear time scale is given by (Verbunt & van den Heuvel 1995)

$$\tau_n \approx \frac{0.1 M \epsilon_\mathrm{H}}{L} \approx 10^{10} \frac{M}{\mathrm{M}_\odot} \frac{\mathrm{L}_\odot}{L}\,\mathrm{yr} \tag{2.1}$$

where $\epsilon_\mathrm{H} \approx 0.007c^2$. Since the stellar core consists (roughly) of 80% hydrogen and 20% helium, the hydrogen burning enables the star to stay on the main sequence for a very long time.

Hydrogen can be burnt to helium in two ways: either by the *Proton-Proton-chain* (pp-chain Weizsäcker 1937; Bethe & Critchfield 1938) or the *CNO-cycle* (Weizsäcker 1938; Bethe 1939), where Carbon, Nitrogen and Oxygen are just used as catalysts and are *not* consumed during the reaction. For a detailed description of both reaction types including possible side paths, see Lang (1999, p. 407).

If the temperature in the stellar core is below $\sim 1.5 \times 10^7$ Kelvin, the pp-chain is most efficient, while at higher temperatures the CNO-cycle is preferred. Since the core temperature strongly depends on the mass of the star, the pp-chain is used by the low mass stars which are located in the lower part of the main sequence, while the CNO reaction requires high temperatures and therefore only takes place in the upper half of the main sequence. ϵ again is strongly temperature dependent (Voigt 1991, p. 265):

$$\epsilon_\mathrm{pp} \propto \rho \times T^{5.3} \tag{2.2}$$

$$\epsilon_\mathrm{CNO} \propto \rho \times T^{15.6} \tag{2.3}$$

The much higher exponent of the temperature in the CNO-cycle gives rise to an exponentially higher energy output of the star, once the CNO cycle is possible. Higher energy output also means that the star is brighter but also requires more hydrogen to sustain the nuclear reactions. A bright massive star therefore consumes its hydrogen in the core much faster than a low mass star and has thus a much shorter life time.

If the core of the star is sufficiently depleted of hydrogen, the remaining hydrogen burning can no longer sustain a nuclear reaction rate high enough to compensate the gravitational pressure. The interior of the star starts to contract and the temperature increases. If the star has a sufficiently high mass ($M > 0.26\,M_\odot$, Karttunen et al. 1990, p. 288), this contraction continues, until the temperature and the density in the core is high enough ($\sim 10^8$ K, $\sim 10^4\,\mathrm{g\,cm^{-3}}$, Iben 1991, p. 59) again to start a new type of nuclear reaction: Helium burning is ignited. Three α particles produce one carbon nucleus. In the meantime, the Hydrogen burning continues in a shell around the core, the *shell burning*. The shell burning provides the bulk of the surface luminosity (~80%). The increased radiation input into the outer layers of the star leads to the expansion of the star itself. This expansion of the star occurs on a *thermal* timescale which is given by (Verbunt & van den Heuvel 1995):

$$\tau_t \approx \frac{GM^2}{RL} \approx 3\times 10^7 \left(\frac{M}{\mathrm{M}_\odot}\right)^2 \frac{\mathrm{R}_\odot}{R}\frac{\mathrm{L}_\odot}{L}\mathrm{yr}. \tag{2.4}$$

Since the surface of the star is now significantly larger, the total luminosity increases despite the fact that the emitted radiation itself is somewhat cooler: the star evolves away from the main sequence in the HRD into a cooler but brighter region (upper right corner of the HRD): the star has become a *red giant*.

This phase lasts again comparably long: The total duration of the helium burning τ_He is ~25% of the total duration of the hydrogen burning time τ_H. The Helium burning continues until the mass of the resulting carbon-oxygen core reaches a mass of $\sim 1.4\,\mathrm{M}_\odot$. Provided that the mass of the star is high enough, the temperature increases again and around 10^9 K, carbon burning is ignited: two carbon nuclei plus a proton produce ^{23}Sodium, or two carbon nuclei plus one α produce ^{20}Neon. During this stage, almost all the energy produced in the core is radiated as (anti-)neutrinos, while the shell burning hydrogen and helium are the sole sources for the luminosity of the star (Iben 1991).

For low mass stars like our sun, the nuclear burning stops when the Helium in the core is exhausted. The mass of these stars is too low to generate enough gravitational pressure to proceed to the next stage of nuclear burning. Stars with a higher mass can generate sufficiently high temperatures such that more and more nuclear reactions become possible, as outlined by Burbidge et al. (1957). The endpoint of all energy producing reactions is ^{56}Fe (or its neighbors like Ni). To generate elements above ^{56}Fe, energy is *needed* and no longer gained by nuclear fusion reactions. Many reactions provide free neutrons which are captured by

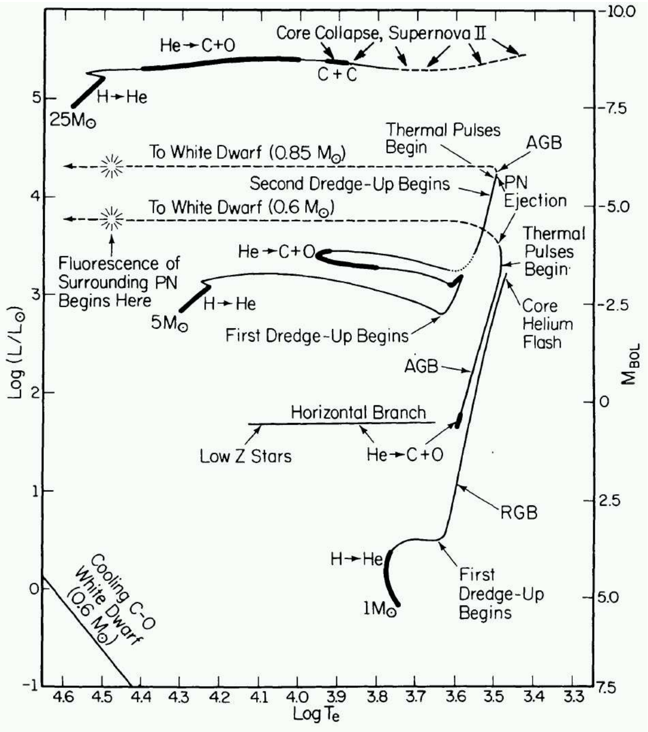

Figure 2.2: Evolutionary tracks in the HRD for low mass ($\sim 1\,M_\odot$), intermediate mass ($5\,M_\odot$) and high mass ($25\,M_\odot$) stars (Iben 1991)

heavy nuclei and elements heavier than iron can be produced. At this point the core burning ends: no energy can be gained by the formation of heavier elements than iron. When all other nuclear fuel in the core is exhausted, the nuclear burning in the core stops. As a result, no radiation is produced to balance the gravitational pressure of the star and the core starts to collapse.

Depending on the mass of the collapsing *core*, one of the following points can happen:

1. For a low mass star, the collapse stops as soon as the core has reached a density of $\rho \sim 10^6$ g cm^{-3} (Iben 1991): at this density the electron gas becomes degenerate. The pressure of the degenerate electron gas is large enough to prevent the core from collapsing further as long as the mass is below $1.4\,M_\odot$ (the Chandrasekhar limit, Chandrasekhar 1931). The core stabilizes

at a temperature of $T \sim 2 \times 10^8$ K and usually has a mass of ~0.5 $M_\odot$ (Iben 1991) and the approximate size of the Earth: a *White Dwarf* has formed. This scenario is true for all low mass stars like our sun.

2. Intermediate stars with a higher initial mass of ~5 $M_\odot$ and a lower mass limit of roughly 2 $M_\odot$ (Weidemann et al. 1992; Eggen & Iben 1988) blow most of their shell away before the core reaches a critical Chandrasekhar mass of 1.4 $M_\odot$ and is disrupted by the *carbon-oxygen flash*. The ejected material can later on be observed as a *planetary nebula*. The remaining hot CO core evolves rapidly along a horizontal track to the blue part of the HRD and is observed as the hot central White Dwarf of a planetary nebula.

3. The evolution of high-mass stars (~25 $M_\odot$) is at frist very similar to the evolution of intermediate-mass stars (Lamb et al. 1976), except that the star starts in the upper part of the main sequence. Stars of this mass consume their hydrogen in the core very rapidly (Eq. 2.1). The star evolves to even higher luminosities and moves to the bright red corner of the HRD (see Fig. 2.2). Although the star is not yet a red giant, the Helium burning is already ignited in the shrinking core. As soon as Helium is used up, Carbon burning is ignited. Nuclear burning continues up to iron: in the end, a Chandrasekhar mass nugget consisting mainly of iron class elements (Iben 1991, p. 61) forms inside the core. Upon exhaustion of all nuclear fuel, this nugget collapses. As the pressure of the degenerated electron gas cannot stop the collapse, the nugget continues to shrink: the electrons are “pressed” into the protons (inverse β decay) and a *neutron star* forms. The idea of such a neutron star has been brought up first by Baade & Zwicky (1934) in a talk given at a conference in Stanford – several decades before Giacconi et al. (1962) actually observed X-rays from the neutron star system Scorpius X-1. Neutron stars are very strange objects: usually they concentrate a mass of 1.4 $M_\odot$ in a sphere with a radius of just 10 km. This sphere then has a mean density of $\rho = 10^{14}\,\mathrm{g\,cm^{-3}}$ (Srinivasan 1997). It can either rotate relatively slowly (periods of almost 1000 s) or so fast that it is almost disrupted (periods down to milliseconds). Another intriguing feature of neutron stars is, that they can have magnetic fields up to several 10^{12} G. In recent years even stronger magnetic fields are thought possible; these objects are then called magnetars (Duncan 1992). The interior of neutron stars is, however, even more strange. While the outer layers still consist of normal atoms, the atoms become completely ionized at a density of $\rho = 10^4\,\mathrm{g\,cm^{-3}}$. At $\rho \sim 10^7\,\mathrm{g\,cm^{-3}}$, the electron gas is degenerate. At this density, ^{56}Fe is already in an excited state. With increasing density, more and more neutron rich nuclei are preferred. First ^{62}Ni, then ^{64}Ni, followed by ^{84}Se up to ^{76}Fe,

^{124}Mo, and ^{118}Kr (Srinivasan 1997, p. 141). ^{118}Kr is already so neutron rich, that with increasing density, the neutrons are no longer actually bound to the nucleus. At a density of $2.5 \times 10^{14}\,\mathrm{g\,cm^{-3}}$, the nuclei start to merge into each other forming a degenerate fluid of neutrons, protons, and electrons. At the center of the neutron star, a density of $\rho = 5 \times 10^{14}\,\mathrm{g\,cm^{-3}}$ is reached. What happens at these densities is largely unknown. To derive a real description of the interior of a neutron star, the equation of state is needed. The exact form of this equation of state at these densities is (unlike for White Dwarfs) unknown. For a thorough discussion of this subject, see Pethick & Ravenhall (1991a) and Pethick & Ravenhall (1991b). For a very detailed discussion of the physics of neutron stars, see Srinivasan (1997, Chapter 3) and for a general discussion of compact objects with special emphasis on neutron stars, see Shapiro (1983).

If the pressure exerted by the gravitational collapse cannot be balanced by the degenerate neutron fluid, the nugget collapses completely and a *black hole forms*. The envelope of the star (containing most of the mass) is completely ejected in a *supernova Type II* explosion. For a very detailed discussion of the physics of supernova explosions, see Woosley et al. (2002); Woosley & Weaver (1986, and references therein).

4. Stars with even higher mass (M >40–50 $\mathrm{M}_\odot$) loose much of their initial mass already during the later stages of their evolution such that even the deep burning shells are exposed (Maeder 1982) – these stars are probably *Wolf Rayet* stars. They evolve like normal high mass stars.

In the end, every stars life ends either as a White Dwarf, a neutron star, a black hole, or the star is disrupted completely (e.g., by a catastrophic carbon-oxygen flash). Hot white dwarfs reside for a short time in the hot blue corner in the HRD and then slowly cool down. As the temperature of the White Dwarf decreases, it becomes fainter and thus more and more difficult to observe. A cold White Dwarf is practically unobservable and is located below the main sequence in the red dark corner of the HRD, the stellar graveyard.

Since neutron stars are very small ($r_{\mathrm{NS}} \sim 10\,\mathrm{km}$), they are very difficult to observe from the beginning. Only if they are still hot and thermally radiating they can be observed directly with X-ray, UV, or optical telescopes. Very few isolated neutron stars are known and even if they are relatively close to the Earth, only the HST or other very large telescopes (like ESOs VLT) can observe these objects as the their visual magnitude is usually $m_{\mathrm{V}} \sim 23$ or weaker (see, e.g., Motch & Haberl 1998; Pavlov et al. 1996). Similar to white dwarfs, these objects also cool down with time and end in the stellar graveyard.

Isolated black holes, however, cannot be observed directly by definition, therefore they cannot be shown whatsoever in the HRD. To observe isolated black holes (and dim isolated neutron stars), a different approach is to search for light bending effects caused by their mass. E.g., the search for massive compact halo objects project (MACHOs, that is, black holes and neutron stars in the galactic halo) scans the Large Magellanic Cloud and if a MACHO enters the line of sight to a star in the LMC, the star will flicker due to the light bending, thus enabling us to estimate the mass of the MACHO (Paczyński 1986).

2.2 Binary Evolution

In principle, the evolution of stars in a binary system follows similar tracks as the evolution of single stars, however, there are surprising differences, which will be discussed in the following.

How binary systems come into existence is still not fully understood; however, there are three main possibilities (Voigt 1991, p. 348):

1. capture of a low mass star by a high mass star
2. fragmentation of a fast rotating high mass star
3. two close condensation nuclei in the molecular cloud giving birth to the binary system, which instead of merging, both separately accrete gas and evolve into stars

The capture of stars can be ruled out as a solution since a close enough encounter is a very rare event (which then also has to take place under certain circumstances), so this possibility cannot explain the large number of close binary systems observed. The fragmentation of a big star is also not likely since fast rotating high mass stars are thought to form either some sort of envelope or a *decretion* ring. Such decretion torii cause *emission* lines in the optical spectrum of the star (usually a B star; a small "*e*" in the spectral classification denotes such emission lines; for a complete discussion of these *Be*-stars, see Porter & Rivinius 2003). This leaves only the simultaneous formation of both stars in the same cloud as possibility.

After the binary system has formed in the gas cloud, both stars follow the same evolutionary tracks as outlined in Section 2.1: they both appear on the Hayashi line and then evolve quickly onto the main sequence, where they stay for a long time. The more massive star, however, evolves faster than the less massive star – and this is where the differences compared to single star evolution starts.

A binary system has a much more complicated gravitational potential than an isolated star: an idealized version (the stars are considered to be point masses) of such a system is known as *three-body-problem*. This potential has two gravita-

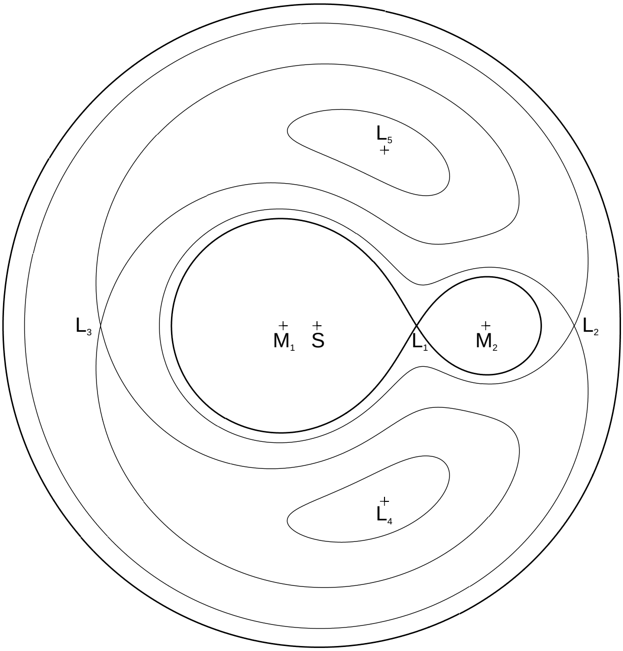

Figure 2.3: Equipotential surfaces of the Roche potential with a mass ratio $M_1 : M_2 = 5$; M_1, M_2 are the masses of the two stars. L_1 to L_5 are the *Lagrange points* and S is the center of mass of the system (from Kretschmar 1996).

tional wells (one for each of the two stars) and five points of equilibrium. This potential was first conceived by Eduard Albert Roche in 1849ff in Paris (unfortunately, the original references Roche 1849a,b, were not available). In a co rotating frame of reference, this *Roche potential* is given by (Frank et al. 1992):

$$\Phi(r) = -\frac{GM_1}{\vec{r} - \vec{r_1}} - \frac{GM_2}{\vec{r} - \vec{r_2}} - \frac{1}{2}(\vec{\omega} \times \vec{r})^2 \tag{2.5}$$

where M_1, M_2 are the masses of the two stars, $\vec{r_1}$, $\vec{r_2}$ the position of the point masses, and ω the angular velocity. An example for such a potential is shown in Fig. 2.3 for a mass ratio $M_1 : M_2 = 5$. Of special interest are the *Lagrange Points* $L_1 - L_5$ and the innermost equipotential surface encompassing both stars, the *Roche surface* (for a detailed discussion of the Roche geometry, see Frank et al. 1992, p. 50). The Lagrange points denote positions in the potential where all gravitational forces nullify each other, meaning that a force-free body will stay at these points forever. This is also of special interest for satellites (the Earth and the sun are also in a Roche potential!), as fuel requirements for keeping the satellite in this position would be minimal. Another application are so called interplanetary superhighways[1] connecting the Lagrange points of the planets resulting in faster and/or less fuel consuming flight paths for interplanetary missions (e.g., the Genesis mission uses such a flight path, Jurewicz et al. 2000). Although these Lagrange points are of such vital interest and the Roche potential looks quite simple, the problem is quite complicated. It is usually solved numerically or approximations are used (see, e.g., Morris 1994). Only very recently Seidov (2003) pointed out some interesting analytical relations.

The Roche surface represents the maximum size of the stars. If either of the two stars exceeds its *Roche Volume*, the material outside the Roche surface is no longer bound to the star and can either drift away or be accreted onto the other star. How can a star exceed its Roche Volume or *Roche Lobe*? Iben (1991) mentions four ways:

1. growth, e.g., due to the stellar evolution
2. orbital shrinking due to loss of angular momentum
3. ignition of previously non burning material
4. collision with another star

In the context of this work, only the first two points are relevant.

The more massive star ($M_1 \gg M_2$, as in Fig. 2.3), will evolve significantly faster. After it has left the main sequence, it will start to expand as discussed in Section 2.1. Since the star is in a Roche potential it cannot grow beyond its Roche lobe. Any exceeding material is no longer bound to star #1 and is transferred to the low mass companion. Depending on the phase in which the massive star exceeds its Roche volume, the outcome of this event is different. In most cases, the massive star looses so much material, that the remaining core evolves into a White Dwarf. According to Iben, Jr. & Tutukov (1985), a 9–11 $\mathrm{M}_\odot$ star evolves into a Oxygen/Neon White Dwarf if mass loss occurs before the ignition of Helium. Intermediate mass stars possess a helium core when the mass transfer begins and will evolve into a CO white dwarf. Less massive stars will evolve into a Helium-white dwarf.

After this phase, the system now consists of a white dwarf and a normal star. If the normal star is despite the mass transfer still a low mass star ($\sim$1 $\mathrm{M}_\odot$ or less), the system will take billions of years to evolve. But in general, the initially less massive star is now more massive and also evolves faster. Since the previous mass transfer also caused orbital shrinkage, the system is now a very close binary, and the normal star will exceed its Roche volume even before igniting Helium

---

[1] see `http://www.spacehike.com/superhighway.html`

(Iben 1991, p. 73). Another common-envelope phase follows and in the end, a second white dwarf (less massive than the first) will emerge. The result is a binary system of two white dwarfs. This type is the most common "end product" of binary evolution (~90 %, Iben, Jr. & Tutukov 1984).

A very interesting evolutionary branch is the development of a *Cataclysmic Variable* (CV; see, e.g., Kraft 1962, for the description of several CVs). If the system is close enough that tidal forces cause an almost locked rotation (orbital and rotational period of the components are the same), the loss of orbital momentum will cause the secondary star to fill its Roche lobe while still retaining hydrogen in its core (Iben 1991). The white dwarf is accreting material from the low mass donor star and the accreted hydrogen is ignited on the surface of the white dwarf. It is possible that if the White Dwarf is massive enough and the transfer rate high enough, that the white dwarf will eventually exceed the Chandrasekhar mass of $1.4\,\mathrm{M}_\odot$. Upon reaching this critical mass limit, the gravitational pressure finally overcomes the pressure of the electron gas, the white dwarf starts to collapse, and explodes as a supernova (Starrfield et al. 1985). For a detailed discussion of cataclysmic variables, see Córdova (1995) and Iben (1991, , Section XII), and references therein.

If the initial stars are both very massive, even more dramatic events happen during the evolution than the formation of a CV. As before, the more massive star evolves earlier on the nuclear time scale (see Eq. 2.1), fills its Roche lobe, and subsequently mass is transfered onto the not so massive companion. The evolved star looses up to 50 % of its initial mass which is mostly transfered to the companion. The evolved star, stripped of its envelope, continues to evolve and depending on the circumstances, even more material is transfered to the companion which, in the meantime, is more massive than the "primary". The evolved core of the primary continues on its evolutionary path and if it still has sufficient mass (e.g., $3\,\mathrm{M}_\odot$), explodes as supernova leaving a neutron star behind. Such explosions are catastrophic events for a binary system: mass will be lost from the system and the orbit will at least change; a complete disruption of the system is also possible. The new eccentricity is then given by (Verbunt & van den Heuvel 1995):

$$e = \frac{\Delta M}{M_1 + M_2 - \Delta M} \tag{2.6}$$

Eq. 2.6 shows that the maximum mass that can be lost during this process must not exceed a total of 50% of the mass of the system for the system to remain bound. If more than 50 % of the mass is lost, the resulting eccentricity e will be greater than 1, meaning that the system will be disrupted. Therefore, mass transfer is required *before* the supernova explosion, if the system is to survive the supernova event. As neutron stars have a relatively small mass of $1.4\,\mathrm{M}_\odot$

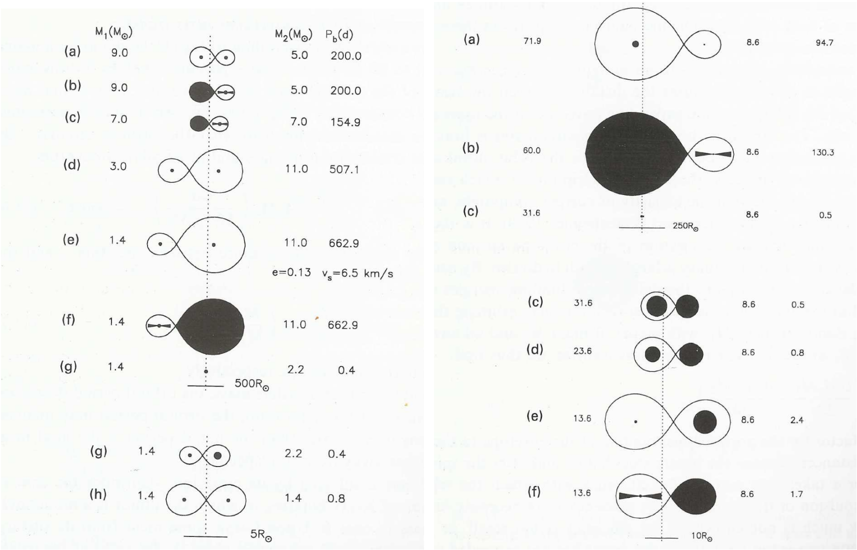
M1(M⊙)
M2(M⊙)
Pb(d)
(a) 9.0 5.0 200.0
(b) 9.0 5.0 200.0
(c) 7.0 7.0 154.9
(d) 3.0 11.0 507.1
(e) 1.4 11.0 662.9
e=0.13 vs=6.5 km/s
(f) 1.4 11.0 662.9
(g) 1.4 2.2 0.4
500R⊙
(g) 1.4 2.2 0.4
(h) 1.4 1.4 0.8
5R⊙
(a) 71.9 8.6 94.7
(b) 60.0 8.6 130.3
(c) 31.6 8.6 0.5
250R⊙
(c) 31.6 8.6 0.5
(d) 23.6 8.6 0.8
(e) 13.6 8.6 2.4
(f) 13.6 8.6 1.7
10R⊙

Figure 2.4: Evolution of a massive binary system. **Left**: First the more massive star evolves earlier and exceeds its Roche volume and material is transfered onto the companion. Finally the more evolved star explodes as supernova, leaving a neutron star in an eccentric orbit behind. As the second star evolves, some mass is transfered onto the neutron star, but most mass is expelled. The secondary star also explodes as supernova, leaving a second neutron star behind. **Right**: same as before, but for a non mass conserving scenario. If the initial mass of at least one component is very large, a lot of mass must be lost during the evolution of the massive star, otherwise the system will be disrupted according to Eq. 2.6. Such a massive system usually produces black holes instead of neutron stars (after van den Heuvel & Habets 1984).

up to $\sim 3\,M_\odot$ (the Oppenheimer-Volkoff limit, Oppenheimer & Volkoff 1939), the mass difference to the progenitor star has to be removed. Observations show that massive optical companions of neutron stars in *eccentric* orbits are almost always Be-stars (Verbunt & van den Heuvel 1995). This is also readily explained by Eq. 2.6: the larger eccentricity means, that a large amount of material has been transfered from the primary to companion star. This material of course carries angular momentum which is thus also transfered onto the companion star – the companion star is *spun up*. This high rotation frequency easily results in the formation of a decretion torus which again gives rise to the observed emission lines.

Since the less evolved companion star has gained mass, it evolves more quickly and will “soon” exceed its Roche volume, too. Some mass is then transfered onto the neutron star, while most of the envelope is expelled. The finally remaining core of the secondary star will also explode as a supernova, leaving a second neutron star in a wide eccentric orbit around its companion behind. See Fig. 2.4 for a sketch of the evolution of a binary system consisting of two massive stars.

If the primary is initially extremely massive (more than $40\,M_\odot$), not all mass can be transfered to the companion. The evolving core is significantly heavier than in the previous scenario, such that the supernova explosion leaves a *black hole* behind. A proto type example for such a system is Cygnus X-1, consisting of the optical star HDE 226868 (Hjellming & Wade 1971; Braes & Miley 1971), an O9.7Iab star with a mass of $\sim 18\,M_\odot$ (Herrero et al. 1995), and a compact object with a mass of $\sim 10\,M_\odot$ (Herrero et al. 1995), which is therefore generally believed to be a black hole (see Pottschmidt 2002, for a very detailed description of the system), although not everybody in the scientific community is convinced that Cygnus X-1 contains a black hole (see, e.g., Kundt 2001). Such a high mass system continues to evolve as described above; in the end the secondary star also evolves into a Neutron Star or a black hole, resulting in a black hole / neutron star or a black hole / black hole binary.

2.3 Accretion

Gravity was the only stellar energy source known in the nineteenth century – previously to nuclear fission and fusion reactions. Chemical energy was already known to be insufficient to power stars (it would be impossible to power our sun using coal burning for more than a few million years). Thermal energy could only sustain the current energy output of the sun for about 10 Million years. Potential energy could, however, power the sun for about 30 Million years, which at least was considerably longer than chemical or thermal energy, but was still a short lived energy form (see, e.g., Herbig 2002). The big problem, however, was that geologists had already shown that the age of the oldest sedimentary rocks was at least 1.3 billion years – forty times older than the sun could be powered by potential energy (or any other form of energy known at that time). Eddington (1930) already remarked, that “…the main source of a star’s energy is subatomic”. This conundrum was finally solved by Bethe in 1938, when he described the pp-chain (Bethe & Critchfield 1938). During the hydrogen burning, hydrogen is burnt to helium. Helium, however, is a little bit lighter than four protons: ~1% of the original mass is missing (Voigt 1991, p. 262). Following Einsteins famous equation (Einstein 1905)

$$E = mc^2 \tag{2.7}$$

the formation of one Helium nucleus sets 26.72 MeV or 4.3×10^{-5} erg free. If only 10% of the Sun's hydrogen is converted into helium, $\sim 2\times10^{51}$ erg are released – enough to power the sun for about *10 billion* years. On the other hand, this process is quite inefficient: It uses less than 1% of the available energy; only the mass difference between four protons and one helium core is converted into energy.

Under the right circumstances, gravitation, however, is far more efficient. Consider the accretion of a test particle with mass m from infinity onto a neutron star. The energy gain is given by:

$$\Delta E_{\mathrm{acc}} = \frac{GMm}{R_{\mathrm{NS}}} \tag{2.8}$$

A neutron star has a radius of ~10 km and usually a mass of $1.4\,\mathrm{M}_\odot$. For a test mass of 1 gram, the energy yield is $\Delta E_{\mathrm{acc}} = 1.86\times10^{20}$ erg. The energy gain for converting 1 g of hydrogen into helium is "just" $\sim 6\times10^{18}$ erg, making accretion more efficient by a factor of ~30. According to Eq. 2.8, the efficiency of accretion strongly depends on the mass *and the size* of the accreting object. Accretion is therefore obviously very important for neutron stars and black holes. Unlike neutron stars, black holes, however, have no surface. Instead, their radius is given by the *Schwarzschild*-radius[2]:

$$R_{\mathrm{BH}} = R_{\mathrm{S}} = \frac{2GM}{c^2} \approx 3\,\mathrm{km}\frac{M}{\mathrm{M}_\odot} \tag{2.9}$$

Already for typical white dwarfs, nuclear burning is much more efficient than accretion, but still of some importance, e.g., in the case of CVs. For all normal stars, accretion is utterly unimportant as an energy source (but can still be observationally interesting).

So in principle, the energy release depends for a given compact object, e.g., a neutron star, only on the amount of material, $\dot{M}$ accreted. Zel'dovich (1964) and Salpeter (1964) were the first to suggest that accretion of material onto a massive object could really be an important astrophysical energy source.

As always, these statements are only valid in a certain regime. If the accretion is assumed to be spherically symmetric (which is, of course, not the case in real objects), the pressure of the outgoing radiation is no longer negligible: Thomson scattering (cross section $\sigma_{\mathrm{T}} = 6.7\times10^{-25}$) becomes important for the electrons. The coulomb forces again force the protons to follow the electrons, otherwise the neutron star would soon be no longer a neutron star and the protons would expelled by electrostatic repulsion. With growing luminosity, the radiation pushes more and more against the infalling material, while the gravitation pulls at the material. At a certain luminosity, the *Eddington Luminosity*, these two forces become equal:

---

[2] The Schwarzschild radius is only valid for non-rotating black holes; the radius of rotating Kerr black holes is somewhat smaller (see Longair 1997, Eq. 15.43).

$$GMm_\mathrm{p} = \frac{L\sigma_\mathrm{T}}{4\pi c} \tag{2.10}$$

$$L_\mathrm{Edd} = 4\pi GMm_\mathrm{p}c\sigma_\mathrm{T} \approx 1.3\times10^{38}\frac{M}{\mathrm{M}_\odot}\,\mathrm{erg\,s}^{-1} \tag{2.11}$$

This simply means that once the Eddington Limit is reached, the accretion rate cannot grow any more. A slight increase of the luminosity and the material will be blown away by the increased radiation pressure, switching the source off. As result the observer would see a non-steady source.

It is important to note that the Eddington Luminosity is valid for a steady accretion flow and a spherically symmetric accretion only. If the material is accreted only on a fraction f of the compact object, the resulting maximum luminosity is roughly given by $f \times L_\mathrm{Edd}$. For very small fractions, this is again not true: while the material is accreted onto the small fraction, the radiation can escape sideways without exerting too much pressure on the infalling gas. This *local Super-Eddington* flux becomes more important in the following.

Before, however, discussing the actual geometry of the accretion process onto the compact object itself, it is necessary to discuss the origin of the accreted material. The source of the accreted material is, of course, the optical companion of the compact object. The optical companion can donate material to the compact object by three (main) means (or combinations thereof), which shall be discussed in the following.

2.3.1 Roche Lobe Overflow

As already discussed to some extent in Section 2.2, in certain phases of the binary evolution, mass transfer between the two stars is possible: when the optical companion evolves, it will also expand (see Section 2.1 and 2.2). If the star exceeds its Roche volume (see Fig. 2.3 and Eq. 2.5), the material outside the Roche volume is no longer gravitationally bound to the star. This material can now be captured by the compact object or expelled into the interstellar medium.

The material captured by the compact object cannot, however, be accreted directly. Due to, e.g., the rotation of the donator star, the material has too much angular momentum. As result, an *accretion disk* forms, where the material is stored; see Fig. 2.5 for a graphical illustration of such a system. The circulation radius of the material is given by (King 1995):

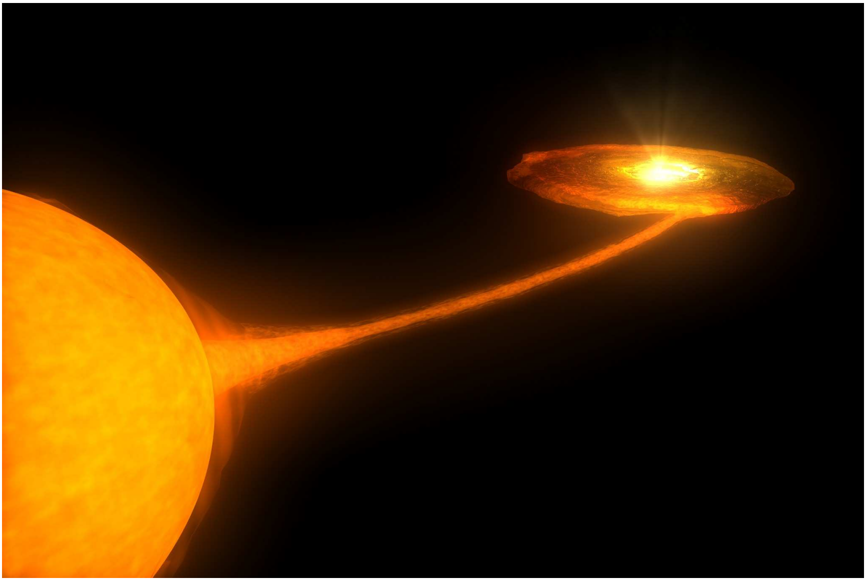

Figure 2.5: A simulation of a low mass X-ray binary system. The low mass optical companion has reached its Roche Volume and is loosing material. The material forms an *accretion stream* and flows from the star to the accretion disk around the compact object. The material moves inward and is finally accreted onto the compact object. Image from UCSD computing center.

$$R_{\mathrm{circ}} = \frac{J^2}{GM_{\mathrm{X}}} \tag{2.12}$$

where J is the angular momentum. This also implies that the radius of the accretion disk cannot be larger than the radius of the Roche lobe of the optical companion; usually it is smaller by a factor of two or three (Frank et al. 1992, p. 56)[3]. In this disk the material looses slowly its angular momentum such that it can move further inwards. However, since the angular momentum must be conserved, some material will also move outwards and can finally escape from the disk. With decreasing radius, the density in this disk grows resulting together with the ongoing inward movement of the material in increased friction. Increased friction again leads to higher temperatures in the inner parts of the disk. A simple way to model a spectrum from such a disk is a *multi temperature black body* – a superposition of several simple black body spectra (Makishima et al. 1986).

---

[3] Since Eq. 2.12 also applies if the accreting star is a normal star, it is possible that R_{circ} is smaller than the radius of the star. The accretion disk therefore crashes into the accreting star, as is probably the case in Algol systems (King 1995).

The actual structure of these accretion disks is very complex; starting from the fundamental α-*disk* model of Shakura (1973), many different geometries and radiation processes have been proposed to explain the observed spectral and temporal features of accretion disks (e.g., a warped accretion disk in the case of Her X-1 Schandl & Meyer 1994, , hot coronae sandwiching a cold accretion disk, slab vs. sphere plus disk geometries, etc). See Wilms (1998, and references therein) and also Pottschmidt (2002) for a review of various geometries and radiation processes.

2.3.2 Be Mechanism

The companion star can also be a *Be-star*. As discussed in Section 2.2, Be-stars in binary systems are all known to rotate very rapidly. Probably due to this fast rotation, a decretion torus is formed around the Be star giving rise to certain emission lines (for more information on such Be- and envelope stars, see Kaler 1994, p. 240). Due to the large percentage of material transfered during the evolution of the progenitor of the compact object, the compact object is usually in an eccentric orbit around the Be star (see Section 2.2).

While the compact object, e.g., a neutron star, is relatively far away from the Be star, it cannot accrete material from this decretion torus. When the neutron star approaches periastron, it will enter the torus or envelope of the Be-star (see Fig. 2.6) and a significant amount of material is now available for accretion. After the accretion disk of the compact object has filled, material is accreted onto the neutron star and X-rays are released; the observer sees an X-ray outburst. When the neutron star leaves the torus again after periastron passage, $\dot{M}$ decreases rapidly. The accretion disk is able to sustain accretion onto the compact object for a short time, but soon after the neutron star has left the circumstellar disk, the X-ray source will become fainter and then stay at a very low level until the next periastron passage.

Such systems show periodic outbursts spaced by the orbital period. An example for such a system is EXO 2030+375 (see Parmar et al. 1989a,b, and references therein). The source, as observed by the All Sky Monitor onboard the Rossi X-ray Timing Explorer (for a description of the instrument, see Chapter 4, Section 4.7), usually brightens considerably every periastron passage for a short time (every ~46 days, see Fig. 2.7).

Some systems, however, are so dim outside periastron, that they are close to being unobservable. Such systems are called *transient sources*.

Depending on the geometry of the orbit of the compact object and especially

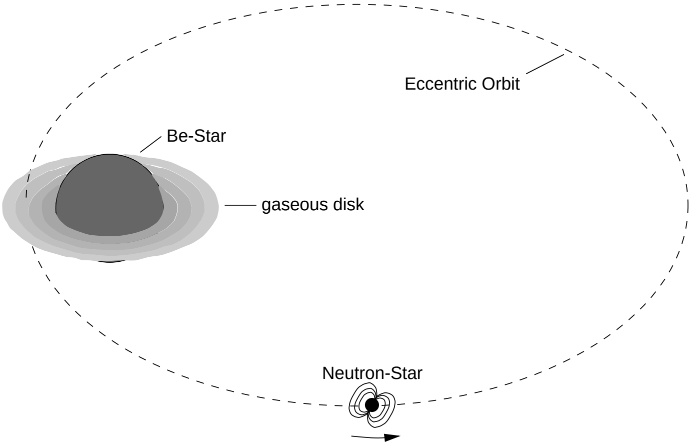

Figure 2.6: A neutron star (or black hole) in an eccentric orbit around a Be star. If the neutron star enters the circumstellar disk of the Be star, an X-ray outburst is observed. While the source is outside the torus, it is in quiescence and either very dim or completely shut off (from Kretschmar 1996).

the stability of the Be star, it is possible that despite the fact that the neutron star approaches periastron, no X-ray outburst is observed. An example for such a system is A 0535+26 which is so dim that it is practically unobservable in quiescence. Although the orbital period is 111 d (Priedhorsky & Terrell 1983), no major outburst has been observed since 1994. But when this source goes into outburst (especially a giant burst as in 1994), it is so bright, that it can significantly outshine most of the brightest X-ray sources (during the maximum the source was about eight times brighter than the Crab, Wilson et al. 1994; Finger et al. 1994b). The reason for this behavior is not yet completely understood; since, however, the emission lines of the Be star almost disappeared (Haigh et al. 1999), it is reasonable to assume that the Be star has lost its torus or envelope such that the neutron star is unable to accrete material. Although the companion of A 0535+26 started to show emission lines again in 1999, a torus is probably present again, it is quite impossible to predict the time of another outburst of this source.

2.3.3 Stellar Wind

So far, the most obvious method of mass loss of the optical companion has not been discussed: mass loss via stellar wind. All normal stars have weak stellar winds. If, however, the optical companion is an O or B star, this wind can be very intense. If the companion is already evolved and its radius has significantly

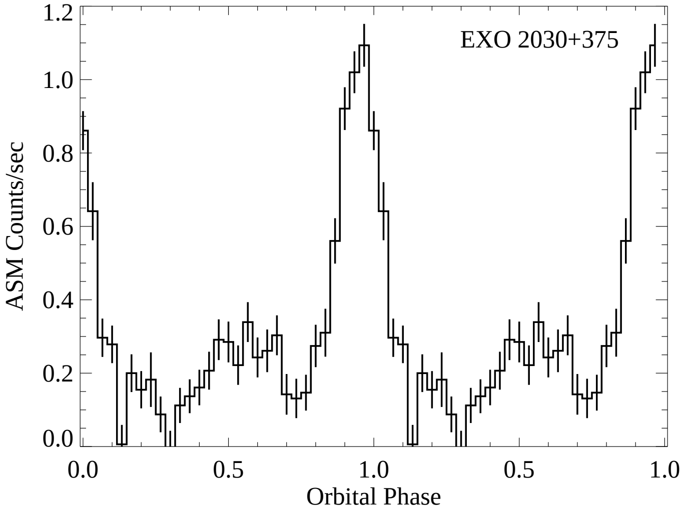

Figure 2.7: Orbital light curve of EXO 2030+375 as observed by the *ASM* instrument of the Rossi X-ray Timing Explorer. The *ASM* light curve has been folded with orbital period of ~46.1 days. Note that the source is usually very dim. During periastron passage, the source brightens suddenly by a factor of 5. After periastron passage, the luminosity of the source decreases again very quickly.

grown, these stellar winds can carry up to $10^{-5}\,M_\odot\ \mathrm{yr}^{-1}$ – $10^{-6}\,M_\odot\ \mathrm{yr}^{-1}$ away. In a typical system, the compact object orbits its optical companion in a height above the surface of the optical star of less than one stellar radius. It is thus deeply embedded in the stellar wind of its optical companion. The compact object then accretes from the dense stellar wind and causes the formation of an accretion wake by focusing a significant fraction of the stellar wind (see Fig 2.8 and Bondi & Hoyle 1944, for a description of this mechanism). Since the compact object is very close to the optical companion, a tidal gas stream might form between the two stars (as has been suggested for Vela X-1 by Taam & Fryxell 1988). The compact object can either accrete directly from the stellar wind (which carries almost no angular momentum) or since some angular momentum is almost always present due to the compact object orbiting the optical companion, an accretion disk or an accretion stream forms. Furthermore, the released X-rays ionize the stellar wind resulting in the formation of an ionization wake which is trailing behind the X-ray source. An artist's impression of such a wind accreting system is shown in Fig. 2.9. In summary, accretion from the stellar wind is a very complicated process which is not yet fully understood and therefore only the most relevant facts can be discussed in the following.

Since the surface of an evolved OB stars is very large, it is not obvious that a neutron star (radius ~10 km) can accrete enough material to power an observable X-ray source. To calculate the reachable X-ray luminosity, the amount of material that can be accreted and therefor the parameters of the wind has to be calculated.

The velocity of the wind is approximately the escape velocity from the surface of the star (Frank et al. 1992), which is given by:

$$v_{\text{wind}} \approx \sqrt{\frac{2GM_\star}{R_\star}} \tag{2.13}$$

where $M_\star$ and $R_\star$ are the mass and the radius of the star. For low mass main sequence stars like our Sun, Eq. 2.13 yields v_{wind} around 600 km s^{-1} which matches nicely the typical observed values between 400 km s^{-1} and 800 km s^{-1} as measured by NASA's *SOHO* mission [4] (Domingo et al. 1995). For main sequence OB stars it is with a few 1000 km s^{-1} much higher. Since the optical companion is usually already evolved, Eq. 2.13 predicts much lower velocities; for, e.g., GX 301−2 which harbors an evolved B star, velocities of the order of 400 km s^{-1} are observed.

The compact object will accrete material from a cylindrical region with radius r_{acc} (see Fig. 2.8), where the gravitational pull of the compact object overcomes the momentum of the wind. This radius is given by (Davidson & Ostriker 1973):

$$r_{\text{acc}} \sim \frac{2GM_{\text{NS}}}{v_{\text{wind}}^2 + v_{\text{NS}}^2} \tag{2.14}$$

where M_{NS} is the mass and v_{NS} the velocity of the neutron star. Since the velocity of the neutron star is usually much smaller than the velocity of the wind, it will be neglected in the following. The fraction f of the stellar wind that is accreted by the compact object is then given by (Frank et al. 1992, Eq. 4.35):

$$f \approx \frac{1}{4}\left(\frac{M_{\text{NS}}}{M_\star}\right)^2 \left(\frac{R_\star}{a}\right)^2 \tag{2.15}$$

where a is the binary separation. Using the typical parameters of wind accreting systems, e.g., Vela X-1 (see Chapter 5), f is of the order of ~ 0.01%, rendering wind accretion a very inefficient process since most of the material is lost to interstellar space. As the stellar wind carries up to $10^{-4}\,\text{M}_\odot\,\text{yr}^{-1}$ away, the total mass accreted onto the neutron star amounts to $\sim 10^{-8}$ per year. If all kinetic energy of

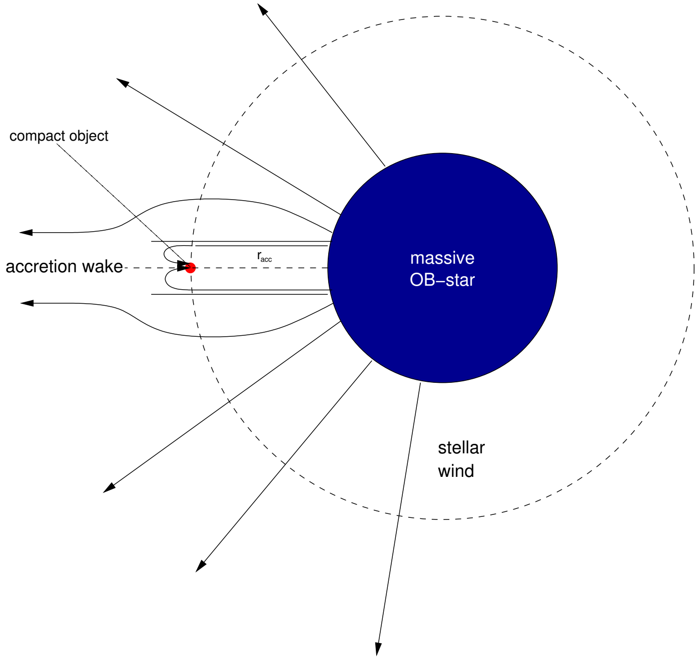

Figure 2.8: Accretion from the wind of an OB star onto a neutron star according to Bondi & Hoyle (1944). All material within the accretion radius $r_{\rm acc}$ will be accreted, leaving an accretion wake behind. Note that this figure is *not* to scale! The neutron star itself is so small that it could not be printed at all: if the evolved star ($\sim$20 $R_\odot$) in the figure has a diameter of $\sim$3 cm, the neutron star would have a diameter of $\sim$200 Å.

all infalling material $\dot{M}$ is converted into radiation, the luminosity of the source is simply given by:

$$L = \frac{G M_{\rm NS} \dot{M}}{R_\star} \tag{2.16}$$

Together with Eq. 2.15:

$$L = \frac{G M_{\rm NS} f \dot{M}_{\rm Wind}}{R_\star}. \tag{2.17}$$

Replacing the constants with numbers results typically in (using $f = 10^{-4}$ and

---

[4] for the latest measurements, see `http://www.sec.noaa.gov/ace/MAG_SWEPAM_24h.html`

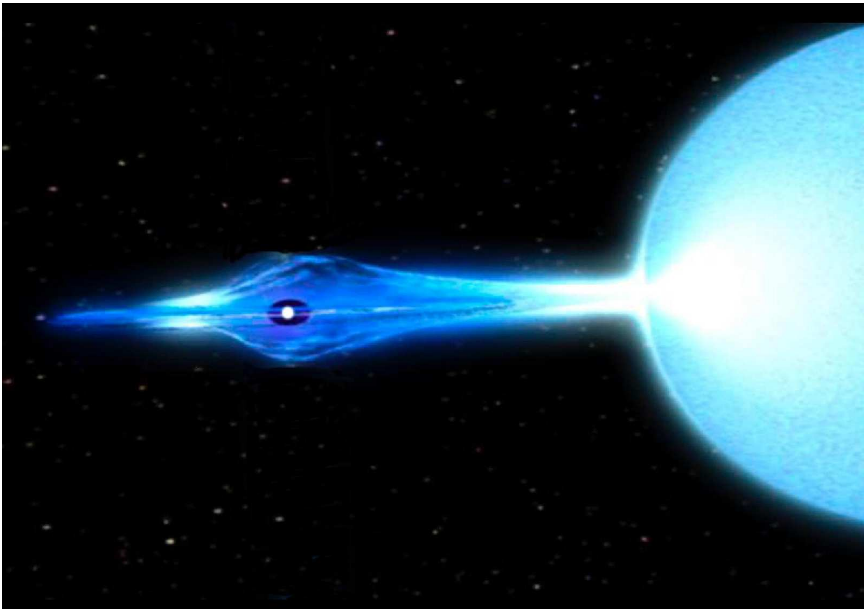

Figure 2.9: Artist's impression of a compact object accreting from the stellar wind of an OB giant companion. Note how deeply the compact object is embedded in the stellar wind. The gravitational pull of the compact object focuses the stellar wind. Compare with the sketch in Fig. 2.8. Image credit: NASA.

$\dot{M}_{\rm Wind} = 10^{-5}\,{\rm M}_\odot$):

$$L \sim 10^{37}\left(\frac{\dot{M}}{10^{-4}\dot{M}_{\rm Wind}}\right)\left(\frac{\dot{M}_{\rm Wind}}{10^{-5}\,{\rm M}_\odot{\rm yr}^{-1}}\right){\rm erg\ s}^{-1} \quad (2.18)$$

$$= 10^{37}\,{\rm erg\ s}^{-1} \quad (2.19)$$

which is a significant fraction of the Eddington luminosity (compare Eq. 2.11). So despite the fact that accretion from stellar wind is very inefficient, wind driven sources are among the brightest X-ray sources in the sky. Typical examples for pure wind accreting systems are Vela X-1 or 4U 1700−377, and wind accretors can account for many of the bright galactic X-ray sources (Lamers et al. 1976).

It should be noted that accretion from the stellar wind does *not* exclude the presence of an accretion disk similar to the Roche lobe overflow scenario. The actual circularization radius $R_{\rm circ}$, however, is smaller by a factor

$$R_{\rm circ,wind} \sim \frac{1}{4} r_{\rm acc}^2 \cdot R_{\rm circ,Roche}. \quad (2.20)$$

This makes the formation of an accretion disk under the appropriate conditions unlikely, if not impossible. Since for an accurate calculation of $R_{\mathrm{circ,Wind}}$ a very good understanding of the stellar wind is required; which is not a simple matter; for details of the formation of an accretion disk in wind driven systems, see, e.g., Börner et al. (1987), and references therein. The stellar wind of evolved giants is still poorly understood, and often observations cannot be explained by standard theoretical models. It is, however, worthwhile to note that some wind driven sources most probably do have an accretion disk, while others do not, and for some sources the evidence is contradicting or does not match the models at all (e.g., Vela X-1, Tjemkes et al. 1986). The situation is even worse for Be/X-ray binary system where it is very difficult to describe the accretion disk and the accretion process onto the neutron star due to the variability of $\dot{M}$ and the variability of the optical star in general, such that it is not a priori clear that an accretion disk is always present in these systems and how this disk evolves with $\dot{M}$ and time (for a discussion of this problem, see Hayasaki & Okazaki 2003, using the Be/X-ray binary system 4U 0115+63 as example).

As a concluding remark, it shall be mentioned that for a given system not only one of the three processes discussed is applicable, but also two (or maybe even all three) at the same time. If the optical companion is a high mass OB star (a high mass X-ray binary, HMXB) which emits an intense wind from which the compact is accreting, this optical star will soon also evolve and finally exceed its Roche volume. Additionally to wind accretion, the compact object will now also be fed by Roche lobe overflow. If a high mass star exceeds its Roche lobe, the resulting mass transfer rate $\dot{M}$ can exceed $10^{-3}\,\mathrm{M}_{\odot}\,\mathrm{yr}^{-1}$. At such high accretion rates, the X-ray source will simply be drowned by too much material, such that the X-ray source will be extinguished (Zuiderwijk et al. 1974).

In many HMXB the optical companion is a Be star. If the compact object is near periastron of the Be star, the compact object will accrete from the envelope of the star and an X-ray outburst is observed. When the compact object, however, is outside this envelope the source would normally be close to unobservable (as, e.g., A 0535+26). Since the Be star usually also has a strong wind, the compact object can feed from the stellar wind when outside the periastron and still remain observable, however, with a reduced luminosity.

If the optical companion of the compact object is a low mass star (a low mass X-ray binary, LMXB), only mass transfer via Roche lobe overflow is possible since the wind of low mass stars is not strong enough to feed a compact object and these stars also are not known to have envelopes similar to Be stars, such that Be mechanism is not applicable.

CHAPTER 3

Magnetic Fields

3.1 Origin and evolution of magnetic fields in neutron stars

So far, the influence of magnetic fields of the accreting objects on the accretion process has not been discussed in this thesis. As I will show in this chapter, the presence of magnetic fields can change the observational properties of a neutron star significantly.

To discuss the influence of magnetic fields on neutron stars, a rough estimate of the strength of the field is required. When the evolved progenitor star of the neutron star collapses, the magnetic flux is conserved. The magnetic field of possible progenitor stars ($M > 9\,\mathrm{M}_\odot$), has, however, up to now never been measured (Bhattacharya & Srinivasan 1995). But since the magnetic field strength is proportional to

$$B \propto R^{-2} \tag{3.1}$$

already Woltjer (1964) and Ginzburg (1964) concluded that the B-field of a neutron star has to be enormously powerful. Assuming that the B-field of a progenitor star has about the same strength as the magnetic field as solar type stars of $B \sim 100\,\mathrm{G}$ (Schatzman & Praderie 1993), Equation 3.1 results in B-fields as strong as $10^{12}\,\mathrm{G}$ up to $10^{14}\,\mathrm{G}$, which is about a million times stronger than the strongest magnetic field that can be produced on Earth (see, e.g., Bichenkov & Shvetsov 1997). Even if the progenitor has a very weak magnetic field or no magnetic field at all to begin with, it is still possible that a B-field develops during the evolution of the star. Since OB stars have a convective core, this core can generate a magnetic field using the *dynamo process* (Borra et al. 1982), similar to the core of the Earth generating the magnetic field of the Earth. It is also possible that the magnetic field is not even present during the main sequence phase of the star: the magnetic field develops when the star has already evolved off the main sequence.

A carbon burning core is very convective such that the magnetic field could also be generated alone during this quite short phase (Ruderman & Sutherland 1973), which is then almost directly followed by the core collapse. This leads to two conclusions:

1. it is unnecessary (and impossible) to relate observed field strengths of main sequence stars to observed magnetic fields of neutron stars
2. it explains why almost all young neutron stars have a very similar magnetic field strength: the magnetic field generated during the carbon burning phase would result in a field strength of $\sim 10^{12}$ G in the newly formed neutron star (Ruderman & Sutherland 1973).

Indeed observations have shown, that the bulk of known neutron stars has a field strength around 10^{12} G (Bhattacharya & Srinivasan 1995). The next major question after we have assessed the strength of the magnetic field is how these fields evolve with time after the formation of the neutron star. Shortly after the confirmation of the existence of neutron stars by the observation of an extra solar X-ray source in 1962 (Scorpius X-1, Giacconi et al. 1962), followed by the discovery of radio pulsars in 1967 by Anthony Hewish and Jocelyn Bell (Hewish et al. 1968), Ostriker & Gunn (1969) concluded that the magnetic fields of neutron stars decays on time scale of just $\sim 10^6$ years. This theory seemed to fit the (very few) observations available at that time and soon became generally accepted, although already Baym et al. (1969) showed that the conclusions of Ostriker & Gunn (1969) are probably wrong. Baym et al. (1969) argue that if the interior of the neutron star is not superconducting, the conductivity of the neutron star would be decaying due to ohmic dissipation due to electrons scattering on neutrons. For a typical neutron star they derive a timescale of $\tau_\mathrm{d} \sim 4\pi\sigma R^2/c^2 \sim 10^{13}$ years (a similar value was also derived by Sang & Chanmugam 1987); a time scale which is much longer than the age of the universe and therefore no decay due to this process should be observable. If the interior on the other hand would indeed be superconducting, the magnetic flux cannot simply leave the superconducting region – fluxoids have to wander to the boundary of the superconducting region. According to Bardeen & Stephen (1965), this process also takes longer than the age of the universe. Therefore Baym et al. (1969) conclude, that the magnetic fields of neutron stars do *not* decay without exterior influence. This conclusion is nowadays also backed by many observations and examinations (Bhattacharya et al. 1992; Srinivasan 1989), which show that there is indeed no decay of the magnetic fields in *solitary* neutron stars on a timescale of ~100 million years, which again is longer than the lifetime of a pulsar anyway (Srinivasan 1997).

This conclusion, however, is not valid for neutron stars in binary systems.

While the magnetic fields of neutron stars cannot decay spontaneously, the magnetic field can decay due to external influences. Srinivasan et al. (1990) suggest a spin down of the neutron star due to accretion as cause for the decay of the magnetic fields. The solid crust of the neutron star and its core are strongly coupled by electrons. When the crust spins down, some magnetic vortices will move outwards and be annihilated at the boundary between the crust and the core resulting in a decay of the magnetic field (it is impossible to discuss this matter deeper here, see Bhattacharya & Srinivasan 1995; Srinivasan et al. 1990, and references therein for a detailed discussion of this problem). Bisnovaty-Kogan et al. (1979) suggest hydrodynamic flows on the surface of the neutron star which could also result in a decay of the magnetic field. Geppert & Urpin (1994) suggested again accretion as the reason for the fast field decay: if the accretion rate is sufficiently high and the accretion phase lasts sufficiently long, the neutron star is heated by the accretion (Fujimoto et al. 1984; Mészáros et al. 1983) thereby decreasing the conductivity of the neutron star. Reduced conductivity again results in a decrease of the magnetic field. According to Urpin & Geppert (1995) this mechanism is able to account for the low magnetic fields observed in many neutron stars in binary systems.

Neutron stars in X-ray binaries exhibit rotational periods from the millisecond regime (e.g., A 0538−66, Skinner et al. 1982) up to over 800 s (e.g., X-Per, White et al. 1976b). Nevertheless, all these objects do (sometimes) have a magnetic field of at least 10^{12} G. The explanation of this apparent contradiction is, however, quite simple. The long periods of some pulsars are due to “fast” electromagnetic braking in the stellar wind of the optical companion and the fast transfer of angular momentum from the companion onto the neutron star. Observations show that these objects are all very young (the companion usually being an evolved B star, the system cannot be much older than a few million years at maximum according to Eq. 2.1) and therefore the magnetic field simply did not have enough time to decay. Given a sufficient amount of time (some million years), the magnetic fields in these systems will also decay.

This turns the attention again on the details of the accretion process in neutron stars X-ray binary systems, which will be discussed in the next Section 3.2, followed by an overview of *pulsars* in Section 3.3. In the last Section 3.4, I will address a very special effect, that can be observed in X-ray spectra of highly magnetized neutron stars: cyclotron resonant scattering features (CRSFs). I will first discuss the theory of these CRSFs, followed by the results of Monte Carlo simulations, and then end this section by discussing observational results.

3.2 Accretion geometry

In Section 2.3 I discussed the various possibilities of mass transfer from the optical companion onto the neutron star including the possibility of disk formation. How does this picture change if the neutron star exhibits a strong magnetic field (e.g., $\sim 10^{12}$ G)?

Assuming a dipole geometry, the strength of the magnetic field B at radius r from the neutron star is given by

$$B \sim \frac{\mu}{r^3} \tag{3.2}$$

where μ is the magnetic moment.Although the strength of the magnetic field strongly decays with increasing r, the influence of r on the infalling material in the vicinity of the neutron star is very strong. According to Frank et al. (1992), the magnetic pressure at radius r is given by (units in cgs):

$$P_{\mathrm{mag}} = \frac{\mu^2}{8\pi r^6}. \tag{3.3}$$

Therefore the magnetic pressure P_{mag} on the infalling material is increasing strongly the closer the material gets to the surface of the neutron star. This increasing magnetic pressure will at a certain radius, the Alfvén radius, be equal to the ram pressure of the infalling gas

$$\frac{\mu^2}{8\pi r_{\mathrm{M}}^6} = \frac{(2GM)^{1/2}\dot{M}}{4\pi r_{\mathrm{M}}^{5/2}} \tag{3.4}$$

For a typical neutron star, the Alfvén radius is given by (in terms of the luminosity of the source):

$$r_{\mathrm{M}} = 2.9 \times 10^8 M_1^{1/7} R_6^{-2/7} L_{37}^{-2/7} \mu_{30}^{4/7}\,\mathrm{cm} \tag{3.5}$$

At the Alfvén radius (also called the magnetospheric radius), the magnetic field disrupts the incoming gas stream (be it a disk, a gas stream, the stellar wind, or something else) and forces the material to follow the magnetic field lines. This transition region from, e.g, a stable disk to the material following the field lines and where the disk ceases to exist, is also known as *boundary layer* (see Fig. 3.1 for a schematic of the boundary layer[1]).

The radius where the angular velocity of the magnetosphere and the Keplerian velocity of the disk are equal is known as *co-rotation radius* (Frank et al. 1992):

$$R_{\mathrm{c}} = \frac{GM_{\mathrm{X}}}{\omega^2} \approx 2.8 \times 10^8 m_{\mathrm{X}}^{1/3} p^{2/3}\,\mathrm{cm} \tag{3.6}$$

---

[1] Note that the term boundary layer is used for a wide range of conditions, including for the transition from a disk to neutron star on the surface of a neutron star.

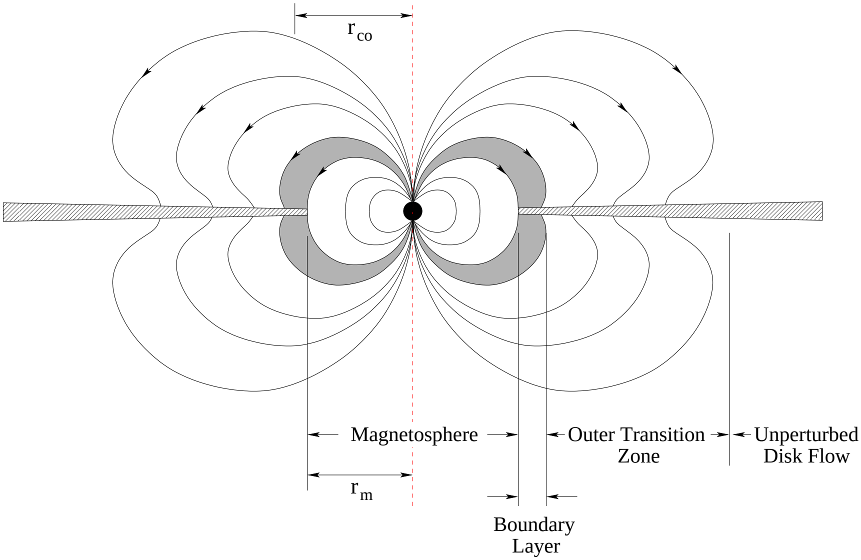

Figure 3.1: Schematic of the accretion from an accretion disk onto a strongly magnetized neutron star (Ghosh & Lamb 1978). At the transition layer the magnetic field disrupts the disk and the material follows the magnetic field lines onto the neutron star (figure from Kuster 2003).

where p is the rotational period of the neutron star in seconds. The description of this boundary layer and its physics is very complicated and has only been discussed for some special cases (e.g. Keplerian α disk). Ghosh and Lamb were the first to try to calculate this transition from the disk to the field lines in their fundamental works (Ghosh & Lamb 1978; Ghosh & Lamb 1979a,b). For more information on the boundary layer, see also Lipunov (1992).

Since the neutron star and its magnetic field lines are a *solid* rotator, the material will be frozen in the magnetic field and forced to co-rotate with the same frequency as the neutron star itself. This allows for an interesting problem: the material can of course only co-rotate, if the rotational velocity of the neutron star is smaller than the Keplerian velocity:

$$\omega R < \sqrt{\frac{GM_{\mathrm{X}}}{R}} \tag{3.7}$$

If the neutron star is rotating faster than the Keplerian velocity, the material cannot follow the magnetic field lines and a *centrifugal barrier* arises, which prevents the accretion of material onto the compact object (Pringle & Rees 1972). Illarionov & Sunyaev (1975) discuss the case where the neutron star is rotating *much* faster than the material and therefore the material gets expelled by the magnetic field, also known as the *propellor effect*. Naturally this effect is difficult to observe as non-accreting sources are extremely dim by definition. If, however, the neutron star is rotating only somewhat faster than the Keplerian velocity at the Alfvén radius, an increase of $\dot{M}$ will also increase the ram pressure and thus change the Alfvén radius (see Eq. 3.5) and accretion becomes possible resulting in observable X-rays. If $\dot{M}$ decreases again, the magnetosphere expands again and the accretion flow will be cut off resulting in a sudden switch off of the X-ray source. White (1989) suggested that this process is the reason for the behavior of some Be/X-ray binaries which are completely unobservable outside periastron. More information on the propellor effect can be found in Lipunov (1992).

Assuming that Eq. 3.7 is fulfilled such that the material can co-rotate with the magnetic field and the material is then accreted, how does the accretion geometry close to the surface of the neutron star look like then?

The physical conditions close to the magnetic poles are very extreme: radiative transfer and radiation hydrodynamics have to be taken into account plus the strong gravitational field requiring a fully relativistic treatment and last but not least a magnetic field of $\sim 10^{12}$ G whose effects on atoms are mostly poorly understood, as such strong magnetic fields cannot be created in the laboratory. Therefore a self-consistent model of the accretion process close to the polar caps is missing; in the past, this problem (or at least some aspects of it) has been addressed by many authors (see Nagel 1981a,b; Mészáros & Bonazzola 1981; Wang & Frank 1981; Harding & Mészáros 1984; Burnard et al. 1990; Lamb et al. 1990, and references therein) using various techniques (analytical solutions vs. numerical Monte Carlo simulations) and making various simplifications (e.g., ignoring relativistic effects, ignoring magnetic fields, etc), however, the results were either too simple or were unable to describe the multitude of observed spectra and light-curves.

Since the material is coupled to the magnetic field lines, it is no longer important, whether it was accreted directly from the wind or from a disk. The material is deposited on the surface of the neutron star at the magnetic poles where the magnetic field lines submerge into the neutron star itself forming a *polar cap*. Lamb et al. (1973) calculate the radius of these polar caps to be approximately one kilometer under the assumption that the magnetic field lines close to the poles are undistorted dipole lines.

But even this simple calculation is already questionable, since the the *accretion column* above the polar cap is probably a hollow cylinder as suggested already by Basko & Sunyaev (1975); for a schematic of this geometry, see Fig. 3.2. In this model, the infalling plasma is funneled within a hollow cylinder onto the surface

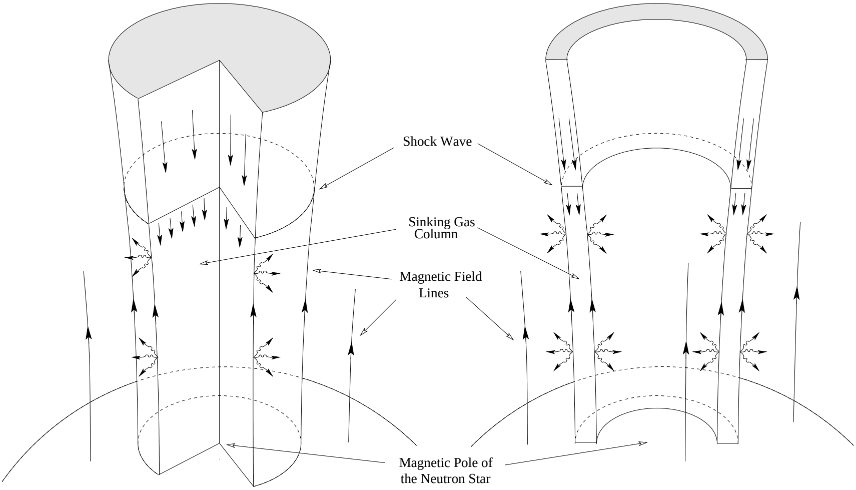

Figure 3.2: Schematics of two geometries of the accretion column above the polar caps of the neutron star, as proposed by Basko & Sunyaev (1976). **Left**: a simple model consisting of a "solid" accretion column. **Right**: the infalling plasma is constrained to a hollow cylinder. The walls of this cylinder are small compared to its radius. The figure is from Kuster (2003).

of the neutron star, where it is stopped by Coulomb forces. This hollow cylinder is due to the material coupling only to field lines of a specific field strength: if the field is too weak, the coupling does not take place. If a certain field strength is reached, more or less all material couples to the magnetic field such that no material is left that could couple to the stronger magnetic field closer to the neutron star. Since magnetic field lines of similar strength also emerge at a similar radius around the magnetic pole, the accretion column should indeed be a hollow cylinder. The width of this funnel turns out to be much smaller than the radius of the whole cylinder (Basko & Sunyaev 1975).

This geometry is independent of the actual accretion rate $\dot{M}$, however, depending on this accretion rate, a shock front may form above the surface of the neutron star: if the accretion rate is high, the infalling plasma interacts with the emitted photons. This results in the formation of a shock front as already discussed by Zel'dovich & Shakura (1969) and later Shapiro & Salpeter (1975) for the case of a spherically symmetric accretion without magnetic fields (see also Fig. 3.2 and Fig. 3.3). The height of the shock front depends on the accretion rate and

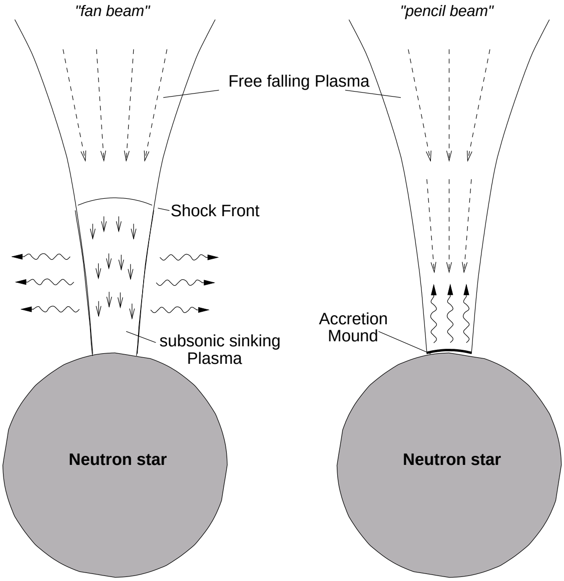

Figure 3.3: Schematic for the case of low and high accretion rates: if $\dot{M}$ is very high, the emitted photons interact with the infalling plasma and a shock front forms above the neutron star, where the plasma is decelerated. Below the front the hot plasma sinks "slowly" to surface emitting X-ray photons perpendicular to the column resulting in a wide fan beam. If $\dot{M}$ is relatively small, no shock forms, and the material falls directly onto the surface of the neutron star and the photons are emitted parallel to the column resulting in a narrow pencil beam. The figure is from Kretschmar (1996) after Harding (1994).

can reach several neutron star radii. The actual structure of this shock, however, is not known, except that it must be some kind of collisionless shock (Harding 1994). According to Frank et al. (1992) a normal collisional shock is ruled out, as the mean free path is much larger than the neutron star itself (Mészáros 1992). Collisionless shocks, however, are poorly understood even without the presence of strong magnetic fields, since another mechanism than viscosity must be called upon that is able to dissipate the energy.

The infalling plasma which has a supersonic speed of roughly $10^{10}\,\mathrm{cm\,s^{-1}}$ (King 1995) is then stopped or decelerated to subsonic speed in this shock front getting thereby very hot. This hot gas sinks down to the surface of the neutron star. During this sinking process, it radiates X-ray photons perpendicular to the column as the column itself is almost opaque to X-ray photons resulting in a very broad emission geometry, a *fan beam* (see Fig. 3.3). If $\dot{M}$ is much lower, the X-ray photons can emerge without interacting with the infalling plasma such that no shock is formed; i.e., the plasma is falling directly onto the surface of the neutron star where it is stopped by Coulomb interactions below the photosphere of the neutron star (Kirk & Stoneham 1982; Kirk & Galloway 1981) and X-ray photons are produced by thermal bremsstrahlung and Compton cooling. The material settles in an accretion mound which is up to 15 m high (Brown & Bildsten 1998). Since the emerging X-ray photons have a very narrow emission characteristic, this emission scenario is called *pencil beam* (see Fig. 3.3).

3.3 Pulsars

After Baade & Zwicky (1934) suggested that there might be some sort of "neutron star", it took quite some time, before this theoretical construct was really related to astronomical observations. Exactly 30 years later, Hoyle et al. (1964) proposed that such a neutron star could reside in the center of the Crab nebula. Another three years later, Pacini (1967) suggested that the energy source responsible for the strong radiation from the Crab nebula could be the rapid rotation of a highly magnetized neutron star.

The "direct" observation of a neutron star was made by pure chance and by people who were not even searching for neutron stars. Instead, Anthony Hewish and the research student Jocelyn Bell were investigating interplanetary scintillation (see, e.g., Little & Hewish 1966). In the first month of the project, Jocelyn Bell discovered strong radio signals that did not look like scintillations. Further analysis revealed a period of 1.335 s. After some initial doubts about the origin of the signal, Hewish published the discovery, suggesting that the source could be a neutron star (Hewish et al. 1968)[2]. Shortly after the publication, it became clear, that these radio pulsars are indeed rotating neutron stars (Gold 1968; Pacini 1968). The explanation for the radio pulses is quite simple: similar to the Earth, the magnetic axis of the neutron star can be offset from the rotational axis. In such a configuration, the magnetic poles and with them the magnetosphere is revolving around the spin axis of the neutron star. The radio emitting region is thus tightly locked with the rotation of the neutron star. Since the radiation of radio pulsars is highly collimated or *beamed*, this radio beam sweeps across the line of sight of the observer, like the light of a lighthouse (that's why this is called the lighthouse effect), resulting in an observable radio pulse whenever the radio beam is directed at observer and quiescence when the beam is pointing somewhere else.

The discovery of the Vela pulsar with a period of 89 ms (Large et al. 1968) and the Crab pulsar with a period of just 33 ms (Stailin & Reifenstein 1968) completely ruled out the still discussed possibility of rotating White dwarfs, as the breakup frequency of a White Dwarf is just ~1 Hz, while Neutron stars are stable up to ~1 kHz (Lyne & Graham-Smith 1998). Again just one year later, also optical pulsations were detected from the Crab pulsar (Cocke et al. 1969). The same year, X-ray pulsations were discovered during rocket flights (Fritz et al. 1969; Bradt et al. 1969) from the same source. Furthermore these teams found that the total luminosity in the X-rays was at least 10 times higher than in the optical band.

---

[2] This source is nowadays known as PSR B1919+21 (Lyne & Graham-Smith 1998).

Shortly after these discoveries, the first X-ray satellite *UHURU*[3] (Giacconi et al. 1971; Kellogg 1975) was launched in 1970. Shortly after launch, Oda et al. (1971) discovered pulsations from the X-ray source Cygnus X-1 which had been discovered some years earlier during a rocket flight (Bowyer et al. 1965) with a period of ~73 ms. Unfortunately (in some sense), the compact object in Cygnus X-1 turned out to be a black hole (see, e.g., Paczyński 1974; Mauder 1973) which does not show pulsations; instead, the observed pulsations were simply due to shot noise (Terrell 1972): the data was consistent with many overlapping short random pulses of ~0.5 s duration

A few months later, *UHURU* discovered the really *pulsating* X-ray sources Centaurus X-1 (pulse period ~4.8 s, Giacconi et al. 1971) and Hercules X-1 (pulse period ~1.24 s, Tananbaum et al. 1972).

The emission mechanism of X-ray pulsars is, however, completely different from the emission mechanism of radio pulsars. While radio pulsars draw their energy from their rotation (rotation powered pulsars; they therefore slow down with time Lyne & Graham-Smith 1998), X-ray pulsars are driven by accretion of material from a nearby star as discussed in Section 2.3. The explanation for the radio pulses, however, also holds true also for these sources: if the magnetic axis is offset from the rotational axis, the X-ray emitting accretion column or accretion mound revolves in and out of sight due to the rotation of the neutron star (Davidson & Ostriker 1973). Since the radiation of X-ray pulsars is not so tightly beamed as the radiation of radio pulsars (see fan vs. pencil beam in Fig. 3.3), the X-ray pulse profiles are very different from the pulse profiles of radio pulsars.

Today, a total of more than 800 pulsars are known, most of these (~700) are rotation powered radio pulsars (Lyne & Graham-Smith 1998) and ~100 are driven by accretion.

---

[3] for more information on the *UHURU* satellite, see `http://heasarc.gsfc.nasa.gov/docs/uhuru/uhuru.html`

3.4 Cyclotron Lines

3.4.1 Theory

As discussed before, the strength of the magnetic field close to the magnetic poles is of the order of 10^{12} G for a typical neutron star. Under these extreme conditions, the motion of the electron is quantized as in quantum mechanics:
under classical "laboratory" conditions, electrons in a magnetic field follow the field lines on a "screw" trajectory. The frequency of this *gyration* is given by the Larmor frequency

$$\omega_{\text{Larmor}} = \frac{v_\perp}{r} = \frac{e}{m}B \tag{3.8}$$

where $v_\perp$ is the velocity perpendicular to the magnetic field. From Eq. 3.8, the gyration radius can be simply derived:

$$r_{\text{Gyration}} = \frac{mv_\perp}{eB} \tag{3.9}$$

Eq. 3.9 shows that with increasing B, r_{Gyration} gets smaller. Applying Eq. 3.9 to the magnetic field strengths found close to the surface of neutron stars, r_{Gyration} gets close to the *de Broglie* wavelength

$$\lambda_{\text{de Broglie}} = \frac{\hbar}{mv} \tag{3.10}$$

thus resulting in quantum effects becoming important in this regime. This means that the motion (or better the kinetic energy) of the electrons perpendicular to the magnetic field can no longer be continuous but is *quantized* (see, e.g. Lai 2001, and references therein) in *Landau levels*:

$$E_{\text{n}} = m_{\text{e}}c^2\sqrt{1 + \left(\frac{p_{||}}{m_{\text{e}}c}\right)^2 + 2n\frac{B}{B_{\text{crit}}}} \tag{3.11}$$

where n is the quantum number with $n \in \mathbb{N}$, $p_{||}$ the momentum of the electrons parallel to the magnetic field, and B_{crit} is the critical magnetic field strength.

As long as $B \ll B_{\text{crit}}$, the difference between any two Landau levels is given by (using Eq. 3.8):

$$E_{\text{cyc}} = \hbar\omega = \frac{\hbar eB}{m_{\text{e}}}. \tag{3.12}$$

(i.e., the Landau levels are equally spaced in the non-relativistic regime). When replacing the constants with numbers, Eq. 3.12 can be approximated in a simple and easy to remember way (**12-B-12 rule**):

$$E_{\mathrm{cyc}} = 11.6 \times B_{12} \tag{3.13}$$

where B_{12} is the magnetic field strength in units of 10^{12} G. This enables the observer to directly derive the strength of the magnetic field from the observed cyclotron energy. Therefore, knowing the correct *fundamental* energy of the CRSF is important for inferring the correct magnetic field strength. Knowing the correct magnetic field strength also helps in understanding the emission mechanisms of accretion powered X-ray pulsars and the effects of the magnetic field on the X-ray production.

When a photon with $E_{\mathrm{cyc}} = h\nu$ interacts with an electron, the electron is raised from its present level n to the next higher Landau level $n+1$ and the photon vanishes (it is “absorbed”). This process gives in principle rise to an absorption line like feature in the spectrum at E_{C}. The decay rate from excited to lower levels is given by (Latal 1986):

$$\nu_r = \left(\frac{\alpha m_{\mathrm{e}} c^2}{\hbar}\right)\left(\frac{B}{B_{\mathrm{crit}}}\right)^{1/2} \tag{3.14}$$

where α is the fine structure constant. As the decay rate is very high (typical values are $\sim 10^{15}\, B_{12} \mathrm{s}^{-1}$), the lifetime of an electron in excited levels is very short, such that an excited electron almost instantly de-excites emitting again a photon with $h\nu = E_{\mathrm{cyc}}$. Since the photon is almost immediately re-emitted after being absorbed by an electron this process is rather a *scattering* process than an absorption process. When de-exciting from a higher level n, it can de-excite directly to the ground level $n = 0$, emitting a photon of n times the cyclotron energy E_{cyc}. An alternative possibility is a cascade: first the decay to the next lower level $n-1$, emitting a photon having just the cyclotron energy E_{cyc}. From $n-1$ the electron again decays to the next lower level $n-2$ until it reaches the ground level. Since several photons are emitted during the decay, this process is called *photon spawning*. Since any excited electron is almost instantly returning to the ground level, this process is rather a scattering than an absorption process. Since the lifetime of the excited states is so short, most electrons will be in the ground level $n = 0$. As photons of the energy of $n \times E_{\mathrm{C}}$ are emitted during de-excitation, it was generally believed at first, that this process would result in an *emission* line in the spectrum at E_{C} (Mészáros 1977; Yahel 1979). Further analysis showed, however, that the free mean path of the photons is so small (Herold 1979) that photons of the cyclotron energy practically cannot leave the plasma: upon emission they will excite another electron. The photons can almost only escape from this region once their energy has changed somewhat (to higher or lower energies) due to the numerous scattering processes such that their free mean path increases. This results in the formation of an absorption line like feature in the spectrum around E_C (Nagel 1981b) and due to the decay from higher levels also at $n \times E_\mathrm{C}$. The line at E_C is usually called *fundamental*, while the other lines are called first, second,... *harmonics*[4]. Note that these lines are not "real" absorption lines, they are due to a scattering process, therefore they are designated as Cyclotron resonant scattering features (CRSFs).

The exact location of the X-ray emitting region depends on the accretion geometry assumed for that source (see Section 3.2). In addition to this uncertainty, the location of the region where these cyclotron processes take place, is also completely unknown; it should, however, be comparably close to the surface of the neutron star, where the magnetic field has the required strength (see Eq. 3.2). Close to the neutron star, however, gravitational redshift becomes important:

$$E_\mathrm{cyc}^\mathrm{obs} = \frac{E_\mathrm{cyc}}{1+z} \tag{3.15}$$

where z is the gravitational redshift, given by:

$$(1+z)^{-1} = \sqrt{1 - \frac{2GM_\mathrm{NS}}{Rc^2}} \tag{3.16}$$

with R being the distance between the center of the neutron star and the cyclotron region. If we assume that the cyclotron region is located at the bottom of the accretion column, just above the surface of the neutron star, R is just the radius of the neutron star. In this case, the canonical value of $R = 10\,\mathrm{km}$ can be used. The the neutron star can usually also assumed to have the canonical mass of $1.4\,\mathrm{M}_\odot$, except for some specific cases, where the mass is known to be higher. One of these cases is Vela X-1 (which is also one of the main objects of this thesis), where the neutron star is definitely known to have a mass of greater than the canonical $1.4\,\mathrm{M}_\odot$: while the mass of the neutron star in Vela X-1 has been measured to be higher than $1.4\,\mathrm{M}_\odot$ for quite some time (van Paradijs et al. 1977; van Kerkwijk et al. 1995), the canonical value could not be completely ruled out due to the uncertainties. Recent measurements by Barziv et al. (2001) and confirmed by Quaintrell et al. (2003), however, yield a mass of at least $1.88 \pm 0.13\,\mathrm{M}_\odot$ (if the inclination is 90°; for smaller inclinations, the mass is even higher), putting Vela X-1 significantly above the canonical value.

When applying these numbers to Eqs. 3.16 and 3.15, a redshift of ~25% is derived, i.e., the intrinsic cyclotron energy and therefore the magnetic field is higher by factor of ~ 1.3.

---

[4] some authors use a different notation: they designate the first line at E_C as the fundamental line as well, but they already call the line at $2 \times E_\mathrm{C}$ the *second* harmonic!

Note that Eq. 3.11 (and all formulae based on it) are only valid as long as the magnetic field is below the critical magnetic field strength B_{crit}. For

$$B \sim B_{\mathrm{crit}} = \frac{m_{\mathrm{e}}^2 c^2}{e\hbar} = 4.414 \times 10^{13}\,\mathrm{G} \tag{3.17}$$

the resulting cyclotron energy will be of the order of 511 keV, the electron rest mass, requiring a relativistic treatment of the problem.

In the relativistic regime, the Landau levels are no longer equidistant, and the cyclotron energies also depend on the angle between the magnetic field and the path of the photon θ (Harding 1994; Harding & Daugherty 1991):

$$E_n = \frac{m_{\mathrm{e}} c^2}{\sin^2\theta}\left(\sqrt{1 + 2n\frac{B}{B_{\mathrm{crit}}}\sin^2\theta} - 1\right) \tag{3.18}$$

Since the individual Landau levels depend on θ, the harmonics are no longer equally spaced. θ itself, however, is not a simple parameter: the resulting energies of the Landau levels now depend strongly on the distribution of the electrons in the plasma and the orientation of the magnetic field lines in the plasma – with other words: the geometry of the CRSF formation region.

3.4.2 Monte Carlo Simulations

As discussed before, theorists tried to solve this problem analytically by using various simplifications (see, e.g., Yahel 1979; Nagel 1980; Wang & Frank 1981; Mészáros & Nagel 1985; Wang et al. 1989, 1993) until the early 1990s. With the availability of fast computers, these semi-analytical models were replaced by Monte Carlo simulations. Nevertheless these models also (have to) use some simplifications. The models of Araya & Harding (1996), Isenberg et al. (1998b,a), Araya-Góchez & Harding (2000) try to model the cross sections as exact as possible and also include thermal broadening of the CRSF lines and the photon spawning from the higher harmonics.

Before using Monte Carlo simulations to calculate the actual spectra, Araya & Harding (1999) calculate the relativistic magnetic Compton cross sections as a function of the angle θ between the movement of the photons and the magnetic field. An example for these cross sections is shown in Fig. 3.4. If the photons are moving almost perpendicular to the magnetic field (i.e., $\theta \approx 90^\circ$ corresponds to $\cos\theta \approx 0$). For such smaller $\cos\theta$, the cross sections around the cyclotron energies are very narrow and similar to a spike. For larger $\cos\theta$ (i.e. smaller θ), the cross sections become broader due to the thermal motions of the electrons along the field lines.

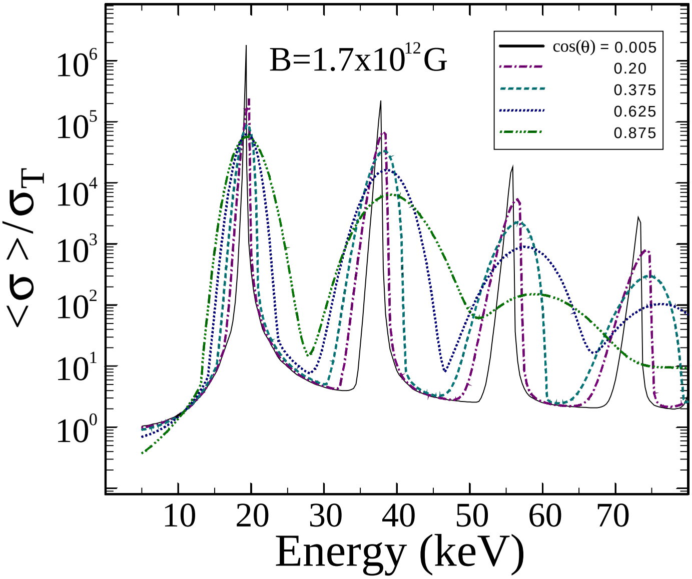

Figure 3.4: Cyclotron scattering cross sections calculated by Araya-Góchez & Harding (2000) for a magnetic field with a strength of $B = 1.7 \times 10^{12}$ G. θ is the angle between the motion of the photons and the magnetic field. Note that with increasing $\cos\theta$ (i.e. decreasing angle), the resonances become broader due to thermal broadening.

Araya & Harding (1999) and Araya-Góchez & Harding (2000) used these cross sections again in their Monte Carlo simulations. Unlike the earlier analytical examinations of the problem (e.g., Mészáros & Nagel 1985), the spectra resulting from these simulations show a much more complicated behavior, which is mainly due to the inclusion of the photon spawning and the non-isotropic redistribution of the photons. Especially the fundamental line is subject to many alterations from a simple absorption line like profile. Most interestingly, *emission wings* are observed in these spectra (see Fig. 3.5). These wings can also fill in the fundamental line completely, such that no absorption line can be observed any more. Under specific circumstances, these emission wings not only fill in the line, but also overlap resulting in an *emission line* (see Fig. 3.5). While these are extreme cases, the photon spawning, however, is usually responsible for almost always filling in the fundamental to some degree resulting in broad but shallow absorption features.

The model on which the Monte Carlo code of Araya-Góchez & Harding (2000); Araya & Harding (1999) is based assumes a highly magnetized plasma with low

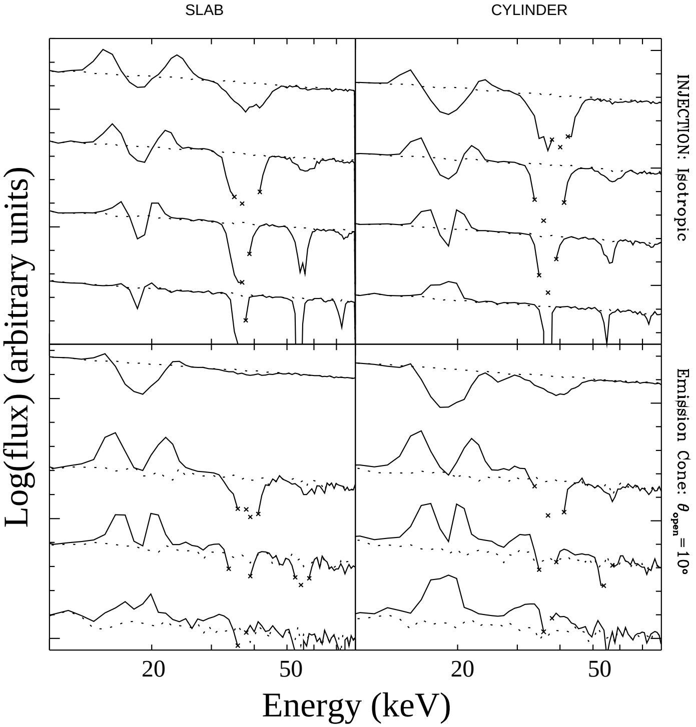

Figure 3.5: Monte Carlo simulations of cyclotron lines by Araya-Góchez & Harding (2000) for a magnetic field strength of $B = 1.7 \times 10^{12}$ G as for the cross sections (see Fig. 3.4). The source spectrum is shown as dotted lines, the emergent spectrum as solid lines. The panels show the results for cylinder and slab geometries and isotropic and non-isotropic injection of the seed photons. The graphs in each quadrant represent different $\cos\theta$ (from top to bottom): $\cos\theta > 0.75$, $0.75 > \cos\theta > 0.5$, $0.5 > \cos\theta > 0.25$, and $\cos\theta < 0.25$. Note the strong variation of the fundamental line which not only can have wings, but also appear in emission.

density. The magnetic field strength is also assumed to be below the critical magnetic field strength $B_{\rm crit}$. The electrons are initially in the fundamental Landau level. The code allows the user to choose between a slab and cylinder emission geometry in analogy to the accretion geometries (see Fig. 3.2 Basko & Sunyaev 1976). Other relevant input parameters of the code are the strength of the magnetic field, the electron temperature, the optical depth of the electron gas, and the photon index α of the incident spectrum.

Major drawbacks of the Monte Carlo code of Araya-Góchez & Harding (2000) and Araya & Harding (1999) are that they use a power law to model the input photon distribution which is very untypical for typical accreting neutron stars. This model produces a very hard spectrum that results in much more photons at higher energies giving rise to higher harmonics and thus also giving more importance to photon spawning. Other major drawbacks are of a more technical nature, but nevertheless limit the usefulness of the code and the produced simulations:

1. the number of energy bins in the input and output spectra is limited/fixed to 80 thus prohibiting the selection of a finer energy binning
2. the number of angles is also fixed to 4. Since the dependence on θ is very strong (compare different angles in Fig. 3.5), a much finer angular resolution is desirable.
3. the simulated line profiles should be compared directly to observed spectra
4. the software itself is very difficult to handle
5. the code itself (written in C) turned out be only sparsely commented (thus difficult to understand) and quite error prone resulting in numerous and sometimes un-reproducable crashes

Peter Kretschmar and I were able to obtain the code itself from Rafael Araya and after many problems due to errors in the code put to work on the computers in Tübingen. After completing a grid of parameters, we observed that the resulting line profiles not only depend simply on the magnetic field strength, but also especially on the viewing angle and the electron temperature. We also found that while the fundamental line usually shows all kinds of emission wings, the higher harmonics show a relatively simple absorption line like profile. The presence and strength of the emission wings depend strongly the angle, the electron temperature, the spectral hardness, and the geometry (see Fig. 3.5).

To compare the resulting spectra with our observational data, we divided the resulting spectra by the incident spectrum to obtain pure line profiles (see Fig. 3.6). These were then incorporated into a a table model for *XSPEC* (Arnaud 1996), which was then applied to our data (Kretschmar et al. 2000) of Vela X-1. We discovered that a significant fraction of the available line profiles can be excluded as they are too different from observed line shapes. While we found it possible to use this model to fit the data, it, however, turned out pretty soon that probably due to the limitations mentioned above and the energy resolution of the available spectra, the fits did not actually improve over using phenomenological models like simple Gaussian absorption lines.

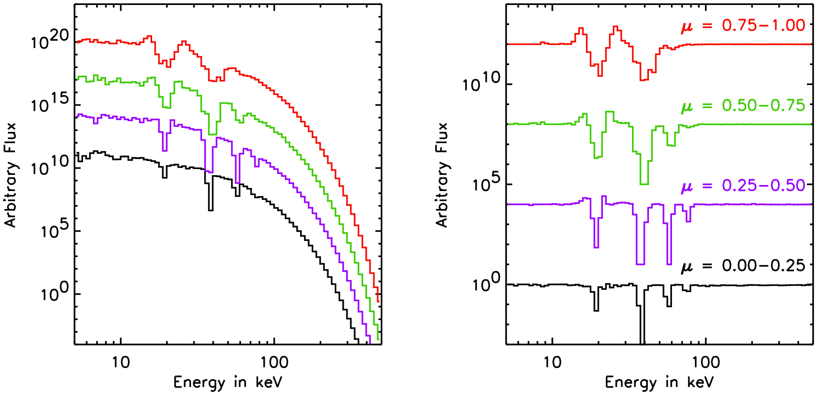

Figure 3.6: Simulated line profiles using the Monte Carlo code of Araya & Harding (1999). As an example, the electron temperature was set to 5 keV. The left panel shows the resulting spectra. The right panel shows the line profiles or relative spectra derived by dividing the resulting spectrum by the incident spectrum. The spectra are sorted from top to bottom with increasing $\mu = \cos\theta$ where θ is the angle between the direction of the photon and the magnetic field.

It turned out that a much finer grid would be required to derive sensible physical parameters, but nevertheless we were able to demonstrate that the results derived from the Monte Carlo simulations of Araya-Góchez & Harding (2000) can be used to fit actual observational data (Kretschmar et al. 2000): we used this table model to fit spectra of the accreting high mass X-ray binary Vela X-1 (for a detailed description of the source, see Chapter 5) taken with the Rossi X-ray Timing Explorer (see Chapter 4). The spectrum of this peculiar source exhibits a strong CRSF at 50 keV and a shallow CRSF at ~24 keV (see Chapter 5). After fitting the continuum using the Negative Positive Exponential (Mihara 1995), we applied our new CRSF table model to the data to fit the two cyclotron features. Since our data does not exhibit significant wings, a large fraction of the parameter grid showing strong wings was immediately excluded. The few remaining grid points showing no or only small wings were able to fit the data (see Fig. 3.7) reasonably well, however, no improvement over the conventional Gaussian absorption line could be achieved and the parameters of the model could not be constrained very well.

While this “proof of concept” shows that it is possible to use these Monte Carlo spectra to fit observational data, it is still a long way until this model is really a

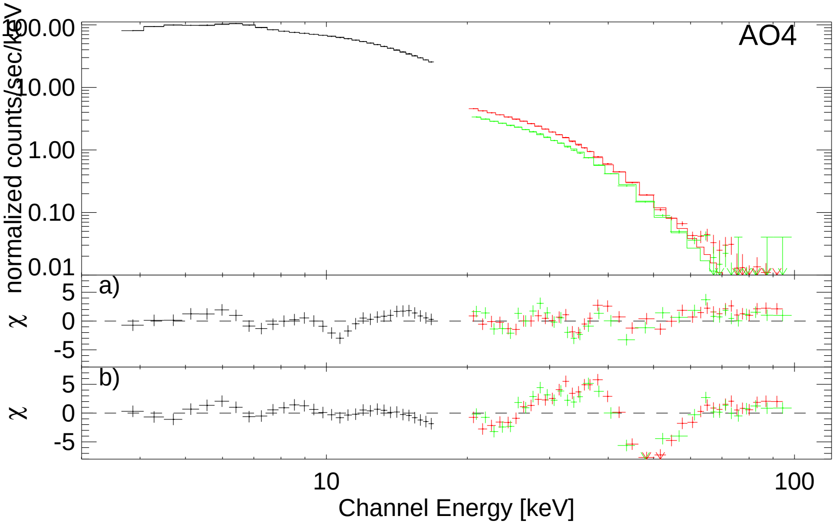

Figure 3.7: Fit using our CRSF model based on Monte Carlo simulations using the code of Araya & Harding (1999). The top panel shows the *PCA* and *HEXTE* data of Vela X-1. **a** shows the residuals when including our Monte Carlo model in the fit. This Monte Carlo model can fit the data very well, however, it was not possible to derive sensible physical parameters from the fit. **b** shows the same model without the inclusion of the CRSF model for comparison.

useful tool for scientific analysis: a much finer grid must be calculated with an improved version of the code.

3.4.3 Observations

Until the mid-1970s, no direct evidence for the cyclotron processes described in this chapter had been observed. Therefore the effects of the strong magnetic field on the plasma was discussed in theoretical papers only and all conclusions about emission/absorption of cyclotron photons were hypothetical (see, e.g., Lodenquai et al. 1974).

On May 3, 1976, Trümper et al. (1977) observed the pulsating X-ray source Hercules X-1 using a balloon borne X-ray detector (“Ballon-HEXE”). They observed a very strong emission feature at ~58 keV in the spectrum of this source (see Fig 3.8). The following years, however, showed that cyclotron lines do not appear in emission but in absorption (Voges et al. 1982; Mihara et al. 1990), meaning that Trümper et al. (1978) actually did not observe an emission line at ~58 keV but an absorption line at ~42 keV. Modern instruments with better energy resolu-

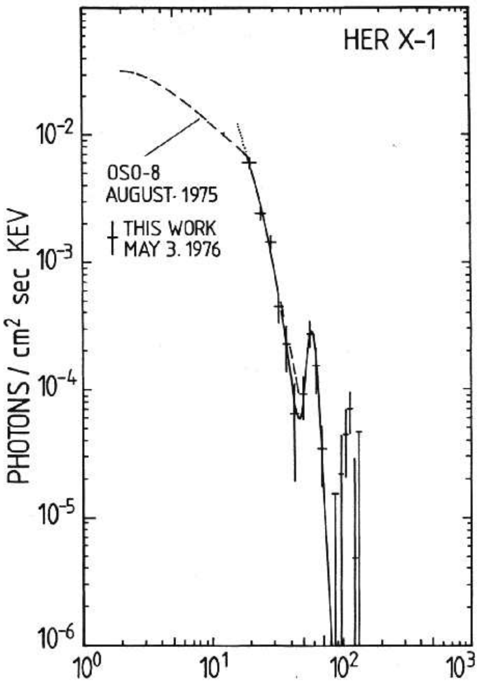

Figure 3.8: First observational evidence for a cyclotron line Hercules X-1 (from Trümper et al. 1978). These authors find an emission line at ~58 keV. In the following years it turned out that cyclotron lines do not appear in emission, but in absorption. Therefore Trümper et al. (1978) did not observe an emission line at ~58 keV but actually an absorption line at ~42 keV.

tion show clearly that this line is in absorption (see, e.g., Kuster 2003; Dal Fiume et al. 1997; Kunz 1996, and references therein); nevertheless, several graduate level books still quote the line as emission line (see, e.g., Unsöld & Baschek 1991; Gerthsen & Vogel 1993).

Only shortly after the discovery of the cyclotron line in Her X-1, Wheaton et al. (1979) reported the discovery of an absorption feature in the spectrum of 4U 0115+63. In a more detailed re-analysis of the data, White et al. (1983) discovered, that in fact *two* cyclotron absorption lines are present in the data.

After these discoveries, no more cyclotron sources were discovered in the following decade. But with the availability of the Japanese X-ray satellite *Ginga*

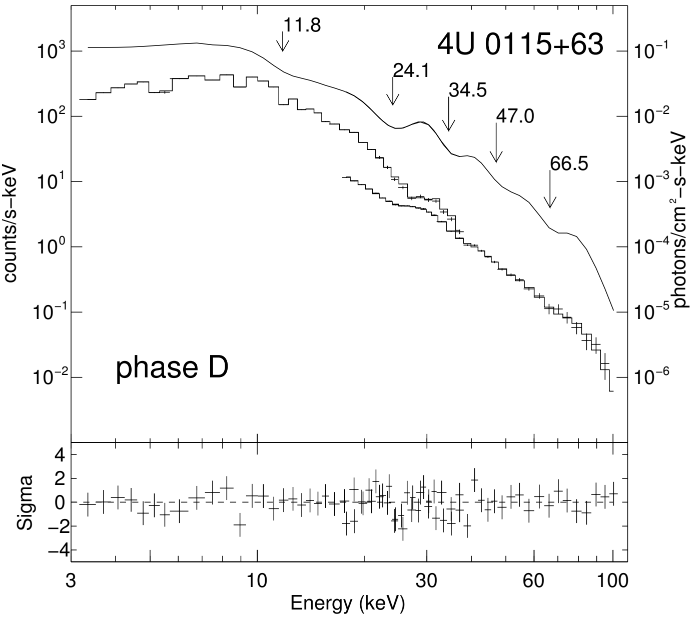

Figure 3.9: The spectrum of 4U 0115+63 as observed by *RXTE*. The upper panel shows the count rate spectrum and the spectral model. The model clearly shows the presence of the five cyclotron lines, which are almost harmonically spaced (except the last one). The residuals in the lower panel show that the fit is excellent.

and the *Mir-HEXE* (a direct successor of the Ballon-HEXE, built in collaboration between MPE and IAAT) in the late 1980s and early 1990s, five new cyclotron line sources were discovered (see Table 3.1), including the sources Vela X-1 and GX 301−2, which are the main objects of this thesis.

Only a few years later the X-ray satellites *RXTE* and *BeppoSAX* were launched in 1995 and 1996, respectively. These observatories offered broad band spectral coverage from ~1 keV to over 100 keV (for a description of *RXTE* see chapter 4 and for a description of *BeppoSAX* see Boella et al. 1997) and were thus especially well suited for the search for cyclotron features in the spectra of accreting X-ray pulsars. These two satellites discovered eight new cyclotron lines (not counting multiple lines). An overview of the cyclotron lines known at the time of the writing of this thesis is given in Table 3.1.

But not only new cyclotron sources were discovered in the recent years, but also previously unknown higher harmonics were discovered. Not only 4U 0115+63

Table 3.1: Overview of all sources which are known to exhibit cyclotron lines. The question mark in the case of LMC X-4 and OAO 1657−415 denotes that a cyclotron line has been reported for these sources, but not yet confirmed. The references given refer to the discovery of the fundamental or harmonic lines or their confirmation. This list also includes the newly discovered cyclotron line of the transient source MX 0656−072.

Source name	E_{cyc} keV	References
4U 0115+63	14, 24, 36, 48, 62	Wheaton et al. (1979, HEAO-1), Heindl et al. (1999b, RXTE) Santangelo et al. (1999, SAX)
4U 1907+09	18, 38	Cusumano et al. (1998, SAX)
4U 1538−52	20	Clark et al. (1990, Ginga)
Vela X-1	24, 52	Kendziorra et al. (1992, Mir-HEXE), Kreykenbohm et al. (2002a, RXTE)
V 0332+53	27	Makishima & Ohashi (1990, Ginga)
Cep X-4	28	Mihara et al. (1991, Ginga)
Cen X-3	29	Santangelo et al. (1998, SAX), Heindl & Chakrabarty (1999, RXTE)
X Per	29	Coburn et al. (2001, RXTE)
MX 0656−072	35	Heindl et al. (2003, RXTE)
XTE J1946+274	36	Heindl et al. (2001, RXTE)
OAO 1657−415	36?	Orlandini et al. (1999, SAX)
4U 1626−67	37	Orlandini et al. (1998b, SAX), Heindl & Chakrabarty (1999, RXTE)
GX 301−2	37	Mihara (1995, Ginga)
Her X-1	41	Trümper et al. (1978, Ballon-HEXE)
A0535+26	50, 110	Kendziorra et al. (1992, 1994, HEXE), Maisack et al. (1997, CGRO)
LMC X-4	100?	Barbera et al. (2001, SAX)

showed a secondary line, but also 4U 1907+09, Vela X-1, and A 0535+26 (see Table 3.1). An outburst of 4U 0115+63 observed by *RXTE* and *BeppoSAX*, however, revealed in a detailed analysis not only the two lines already found by White et al. (1983), but *three* additional higher harmonics – a total of five cyclotron lines (see Fig. 3.9 and Heindl et al. 1999a; Santangelo et al. 1999; Heindl & Chakrabarty 1999), making this source the record holder among the cyclotron sources.

CHAPTER 4

The Rossi X-ray Timing Explorer

The Rossi X-ray Timing Explorer (*RXTE*) was named after Bruno B. Rossi, the Italian born American astrophysicist who worked in the field of solar X-ray emission. In this chapter, the most important characteristics of the satellite and its instrument will be described, while the the satellite itself and the mission objectives are described in great detail by Bradt et al. (1993) and technical details in XTE-Staff (1995).

RXTE covers a broad energy range from 2 keV to over 200 keV. Since this cannot be accomplished using just one single instrument, *RXTE* uses two different instruments for pointed observations:

1. at lower energies (2–60 keV) the *Proportional Counter Array* (*PCA*; Jahoda et al. 1996), built at the Goddard Space Flight Center (GSFC), and
2. at higher energies (15–250 keV) the *High Energy X-ray Timing Experiment* (*HEXTE*; Rothschild et al. 1998) built at the Center for Astrophysics and Space Sciences (CASS) of the University of California at San Diego (UCSD).

Furthermore, as outlined in chapter 2, the X-ray sky is strongly variable: previously unknown sources might appear for a short time period (e.g., the newly discovered *INTEGRAL* source IGR J17544−2619 Sunyaev et al. 2003), a previously seen but due to very long quiescence lost source might suddenly reappear (e.g., MX 0656−072 was recently rediscovered with *RXTE*; the last data on this source are *Ariel* observations of the 1975 outburst Remillard & Marshall 2003), a known transient might have an outburst (e.g., XTE J1550−564 Dubath et al. 2003), or A 0535+26 where many scientists are eager awaiting the next (major) outburst; almost 10 years passed since the last outburst of this source in 1994 (Finger et al. 1994a), or a well known source might do something unusual or unexpected, e.g., the anomalous low state of Her X-1 (Oosterbroek et al. 2001; Still et al. 2001). Therefore *RXTE* has a third instrument: the All Sky Monitor (*ASM*; Levine et al. 1996). As soon as the *ASM* discovers something unusual or

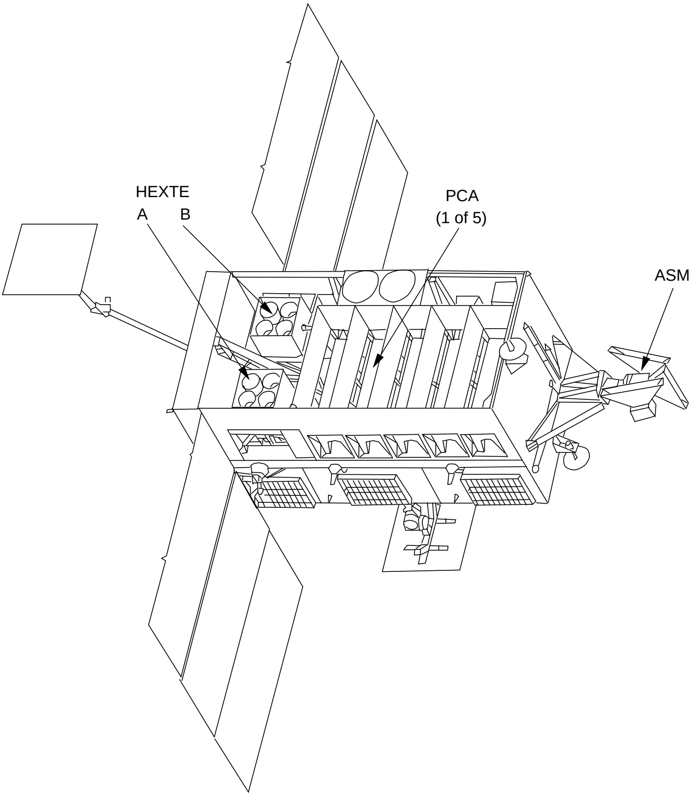

Figure 4.1: Schematic of the *RXTE* spacecraft. The five rectangle structures taking up most of the satellite are the five Proportional Counter Units (PCUs) composing the low to medium energy instrument, the Proportional Counter Array (*PCA*). The two square instruments left of the *PCA*, consisting of four detectors each are the two High Energy X-ray Timing Experiment (*HEXTE*) clusters A and B. The All Sky Monitor (*ASM*) is located at the right side of *RXTE* with a clear view to most of the sky. Above the *PCA* are the two star trackers used for positioning the satellite located. The two antennas extend to the left and the bottom. On the right and left side of the satellite are the solar panels. Figure from Wilms (1998).

of otherwise great importance, the project scientist can decide to abort the current observation and point the satellite at the region of interest. *RXTE*'s high slewing speed of ~6°/minute allows to point the satellite in almost any direction in less than one hour.

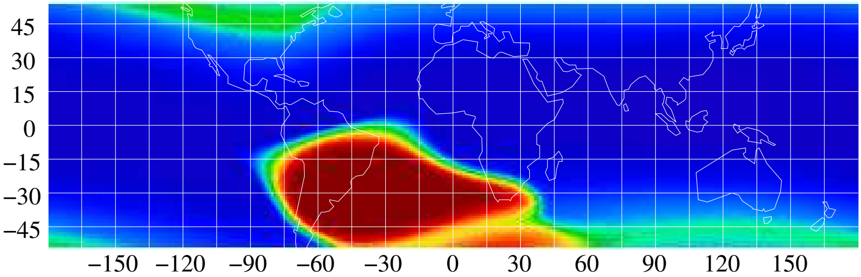

Figure 4.2: The South Atlantic Anomaly as measured by *ROSAT* (Snowden 1996). The most intensive particle flux is located south-east off the Brazilian coast.

4.1 The Spacecraft

RXTE was launched in 1995 December 30 by a Delta II rocket from the Kennedy Space Flight Center into a low earth orbit (LEO), about 580 km above the earth with an inclination of ca. 23 degrees (see `http://rxte.gsfc.nasa.gov/docs/xte/XTE.html`). This corresponds to an orbital period of about 90 Minutes; it therefore cannot keep contact with a fixed ground station; instead the TDRSS-System is used to stay in contact with the satellite. *RXTE* uses a steady downlink of about 20 kbits per second and has access to a high speed downlink of 256 kbits per second once a day for about half an hour and/or 512 kbits per second for 15 minutes through its (originally two) high gain antennas – while one antenna transfers data, the other one locks onto the next TDRSS satellite. Unfortunately, only one of these antennas is still working. For details on telemetry and on-board electronics, see the technical appendix F, available at `ftp://legacy.gsfc.nasa.gov/xte/nra/appendix_f/global`.

A very serious problem for all satellites, but especially for X-ray satellites are the radiation and particle belts around the earth discovered by the first US satellite, Explorer 1 (van Allen 1958; van Allen et al. 1959). These radiation belts, named after their discoverer "*van Allen belts*" are due to the specific configuration of the magnetic field. Since the *RXTE* is in low Earth orbit, it is far below the lowest van Allen belt which is found at a height of about 1000 km and therefore *RXTE* is protected from the aggressive particle radiation. In the south Atlantic south-east off the coast of Brazil, however, the configuration of the magnetic field of the Earth is slightly different: the magnetosphere has a dent in this area such that the high energy particles usually captured inside the van Allen belts can enter this zone. As a result, a very intense particle background is present in this area (the South Atlantic Anomaly, SAA; see Fig. 4.2). This particle background is responsible for very high count rates in the detectors of the satellite and thus renders any scientific observations useless and in the case of proportional counters even endangers the instruments themselves. Therefore the instruments are usually shut off or lower the high voltage of the proportional counters when the satellite passes through the South Atlantic Anomaly.

4.2 Instruments

4.2.1 PCA

The *PCA* consists of five co-aligned Xenon proportional counter units (PCUs). Each of these units again consists of several layers: at the top a propane layer which acts as a Veto Layer. The propane layer is followed by three Xenon detector layers. At the bottom is another veto layer, filled with Xenon gas (see Fig. 4.3). Each of these five layers is a full featured proportional counter (for a detailed description of the physics of proportional counters, see Grupen 1993, p. 97). Due to the size of these layers, a net of anodes is used instead of the classical single anode (see Fig. 4.3). The outermost anodes of the three detection layers are not connected to the detection net, but also act as veto counters. The two veto layers (top and bottom) and the veto counters on each side of each layer allows to discriminate between unwanted photons (or particles) entering the *PCA* from the side or below the instrument and source photons from above. To make sure that only source photons get detected from above, a collimator in front of each PCU limits the field of view (FOV) to 1 degree. A FOV of 1 degree is usually limited enough to distinguish between two X-ray sources, even in crowded fields like the Galactic center. If, however, two sources are located closely together, e.g., AGN in the Marano field (Marano et al. 1988) or the so called "double pulsar", two pulsars with an angular separation of just 15 arc minutes (consisting of the two pulsating sources 2E 1145.1−6141 and 2S 1145−619, Lamb et al. 1980; White et al. 1978, 1980), *RXTE-PCA* is unable to make separate observations of these sources, although off-center observations (such that always one source is outside the field of view) have been tried. Such observations are, however, very difficult to analyze as the ancillary response is badly known for such source positions.

Taking all source detection layers of all PCUs together the *PCA* has a total effective area of ~6000 cm^2 and a nominal energy range from 2 to 60 keV with an energy resolution of 18% at 6 keV in the beginning. As time wore on, however, certain PCUs (PCU 4, at first, followed by PCU 3) started to show unexpected behavior: breakdowns were observed occasionally. Jahoda et al. (1996) proposed that this was caused by sparks within the Xenon/Methane chambers resulting in polymerization of the quenching gas. To increase the lifetime of the PCUs, several measures were taken:

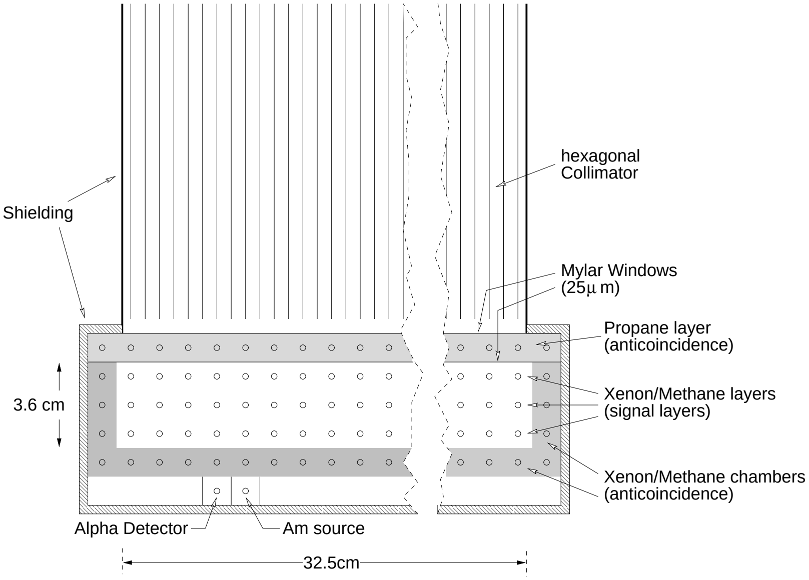
hexagonal Collimator
Shielding
Mylar Windows (25µ m)
Propane layer (anticoincidence)
3.6 cm
Xenon/Methane layers (signal layers)
Xenon/Methane chambers (anticoincidence)
Alpha Detector
Am source
32.5cm

Figure 4.3: Schematic of one of the five Proportional Counter Units (PCUs) of the *PCA*. Figure from Wilms (1998).

1. the detectors in question were sometimes switched off to let them rest even during science observations. Later on, all detectors were affected such that all detectors are periodically switched off. While at the beginning of the mission, *five* PCUs were available to the observer, in the most recent announcement of opportunity (AO9), in average only *two* PCUs are switched on at the same time.

2. Until 1996 March 21, the high voltage of the PCUs was lowered to 1000 V during SAA passage. After 1996 March 21 they were switched off completely.

3. The high voltage during science observations was also changed: it was lowered from 2000 V in the beginning to about 1950 V in two steps on 1996 March 21 and 1996 April 15. On 1999 March 22, the voltage was lowered to setting 4 instead of setting 5.

A side effect of the voltage changes is an increased nominal energy range from 2 keV to 60 keV to now to 2 keV to over 100 keV. This, however, resulted in a deterioration of the energy resolution of the instrument. This of course also means that a different response matrix and a new background model are needed for the different *gain epochs*. This is especially problematic for epoch 1 (launch – 1996 March 21) and even worse for epoch 2 (1996 March 21 – 1996 April 15), since these epochs are very short and only very limited calibration data are available resulting in larger uncertainties in the response matrix and the background model.

During AO4 in 2000 May 12, the propane chamber of PCU 1 started leaking and emptied within one day. This resulted in a significantly increased background in the three detection layers of this PCU thus rendering the data from this PCU difficult to analyze.

The *PCA* background consists of three components:

- the diffuse cosmic X-ray background, which is generally believed to consist of unresolved AGN and other X-ray sources (Comastri et al. 1995; Matteo et al. 1998; Comastri et al. 1999; Fiore et al. 1999; Moran et al. 2001; Hasinger 2002),
- a particle background consisting mainly of energetic protons and electrons, but also other particles. These particles interact with the detector in a similar way as X-ray photons,
- *internal* background produced by interaction between high energy particles (and photons) with the detector and the satellite itself, e.g., during SAA passages. Especially during the SAA passages, the activation of the satellite materials is very obvious: after SAA passage, an exponential decay of the background can be observed.

Background subtraction in the *PCA* is done by a model as the instrument is constantly pointed at the source[1]. For the analysis of Vela X-1 and GX 301−2 data, the *Sky_VLE*-model (see Stark 1997, for a description) was used, as is appropriate for these bright sources. The background of *PCA* is shown in Fig. 4.4.

For calibration purposes, the *PCA* uses a ^{241}Am source. ^{241}Americium is an α-emitter which emits characteristic photons with an energy of 59.6 keV at the same time. A small α-detector located along with the Americium source, detects the α particles emitted by the Americium source. Any photon detected within the *PCA* at the same instant must have an energy of 59.6 keV thus making an automatic gain correction possible.

Although the *PCA* has a nominal energy range from 2 to over 100 keV (after the gain change), the *useful* energy range is usually limited to energies between 2 keV

---

[1] At the beginning of the mission, when the background model was still not working properly, another possibility was to use Earth occultation data to obtain a decent background (e.g., Kreykenbohm et al. 1999). In later AOs, however, the PCUs were also usually switched off during Earth occultation.

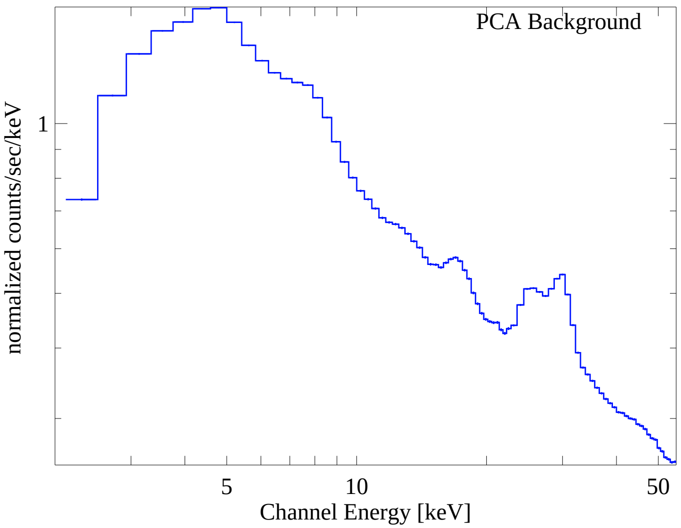

Figure 4.4: Background spectrum of the *PCA*. The very strong emission "line" between 4 keV and 5 keV is the Xenon L-edge; the Xenon-K edge is found at thirty keV. The other features are due to various lines from activated spacecraft materials.

and at most 30 keV. The reason for this severe limitation is the Xenon K edge located at 34.6 keV. Close to this edge, the effective area of the *PCA* is reduced from more than 6000 cm^2 between 6 keV and 10 keV to less than 1 cm^2 between 32 keV and ~34.6 keV. Above the Xenon K edge at 34.6 keV, the effective area reaches again about 1000 cm^2, but the response matrix is not well understood in this regime and the *HEXTE* is the better instrument than the *PCA* above ~25 keV.

4.2.2 HEXTE

The High Energy X-ray Timing Experiment built at the Center for Astrophysics and Space Sciences of the University of California at San Diego (UCSD) is a further developed version of the A4 detector of the High Energy Astrophysics Observatory (HEAO) (Matteson 1978). The *HEXTE* consists of two clusters of four NaI(Tl)/CsI(Na)-Phoswich scintillation detectors (for a description of scintillation detectors, see, e.g., Gerthsen & Vogel 1993) each, which are sensitive from 15 keV to 250 keV. For a very detailed description of the instrument, see Rothschild et al. (1998); I will only mention the most relevant points here.

All eight detectors are all alike, a schematic of one detector is shown in Fig. 4.5.

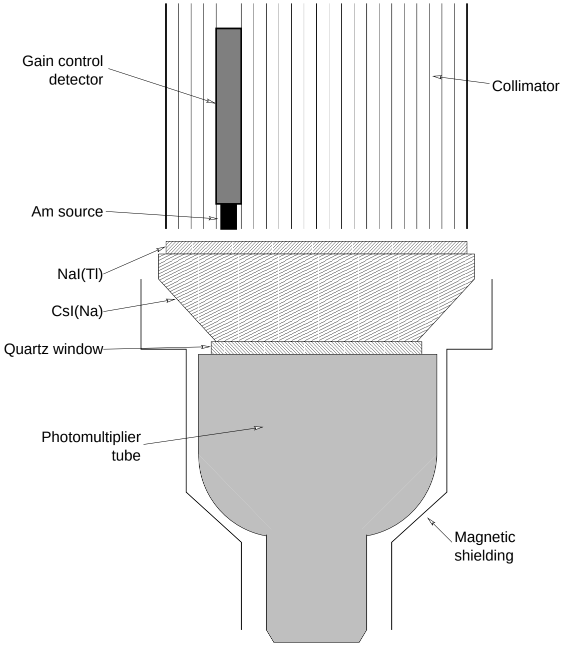

Figure 4.5: Schematic of one of the eight *HEXTE* detectors. The source photons enter from above passing the collimator and exciting scintillation light in the sodium iodine (doted with Tellurium) crystal. The second crystal below (Caesiumiodine doted with sodium) is much thicker; it detects background photons which are entering the detector from the sides or the bottom. The resulting scintillation light is then amplified by the photomultiplier tube. The different decay times of the light emitted by the two crystals – 0.25μs for NaI(Tl), $\sim 1\mu$s for CsI(Na) (Grupen 1993) – allow for a discrimination between scintillation events in the two crystals: an event is only accepted, if the light has a decay time of 0.25μs corresponding to an event in the NaI(Tl) crystal assuming that no other anti coincidence flag is raised. Figure from Wilms (1998).

In front of each detector, a collimator similar to the *PCA* is mounted which limits the field of view to one degree. Also similar to the *PCA*, an ^{241}Americium source is used for calibration purposes. It is mounted in the collimator inside the field of view (see Fig. 4.5).

The two clusters together have a total net detector area of $1600\,\mathrm{cm}^2$ at 50 keV. As the magnetic field changes due to the inclination of *RXTE*'s orbit and since the photomultipliers are sensitive to such changes, the whole detector is encased in a magnetic shielding. Furthermore, also an anti-coincidence shield against charged

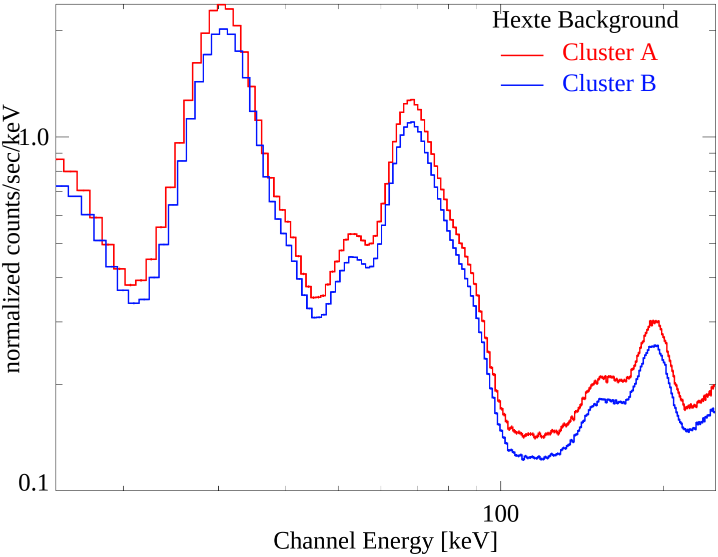

Figure 4.6: Spectrum of the *HEXTE* background for clusters A and B. The background is dominated by internal activation effects (Rothschild et al. 1998). I obtained more detailed information on the background directly from the *HEXTE*-Team at UCSD (Gruber 1997): the most prominent line at ~30 keV is a blend of X-rays from Tellurium and Iodine: cosmic rays and high energy particles trapped in the magnetic field of the Earth interact with ^{127}I of the detector, often destroying the Iodine nucleus (so called spallation), leaving several unstable nuclei, which upon decay emit X-rays around 30 keV. The line at 58 keV is due to inelastic scattering of neutrons on ^{127}I. The prominent line between 60 keV and 80 keV is also a blend of lines consisting of K-α X-rays from the lead of the collimator, as well as from ^{125}I. The next prominent line at 191 keV has been identified being due to ^{123}I. The overall continuum is due to ^{128}I produced by neutron capture on ^{127}I and $\beta-$ and $\beta+$ decays of many different unstable nuclei produced by spallation. The shift between both clusters is due to cluster B having only three fully functional detectors, while cluster A still has all four detectors.

particles is present to minimize the background. Nevertheless the background of these detectors is much higher than the background of the *PCA*; in fact it is usually also much higher than the source signal (for the comparably bright sources discussed in this work, Vela X-1 and GX 301−2, the background and the source are equally strong at ~30 keV. At ~70 keV, the background is stronger by a factor of 100). Furthermore the spectrum of the background is not flat, but is full of lines which make it vital to know the background exactly (see Fig. 4.6).

Background subtraction in *HEXTE* is done by source-background swapping of the two clusters every 32 s throughout the observations (Gruber et al. 1996). To avoid any accidental contamination of the background by a stronger X-ray source, the clusters have several background positions ("plus" and "minus"), such that a "plus" and a "minus" background can be extracted.

This high background is also in part responsible for the relatively high deadtime fraction, ranging usually between 30% and 40% thus reducing the effective on-source time significantly. A second reason for the high deadtime are very energetic cosmic rays that result in long lived excitation states in the crystals.

Early in the mission an electronics failure left one detector in the second cluster unusable for spectroscopy, thus reducing the effective area of second cluster by 25%. Apart from this unfortunate incident, there have been no other relevant events in the *HEXTE*. Due to the continuous automatic gain control (Pelling et al. 1991), the response matrix is also constant over the years.

4.2.3 ASM

The All Sky Monitor (*ASM*) was built at the Massachusetts Institute of Technology (MIT). Its purpose is to scan most of the X-ray sky at least once per day using three scanning shadow cameras (SSCs). One of these three cameras is shown in Fig. 4.7. Each of these cameras has a field of view of $90^\circ \times 6^\circ$ enabling it to observe a significant fraction of the sky. The cameras remain in the same position for ninety seconds and then move to a new position. Thus almost the complete sky (~80%) is scanned at least once per day. The only exception is of course the region too close to the sun.

Since $90^\circ \times 6^\circ$ is a very wide field of view, conventional techniques like a simple collimator (as used for the *PCA* and the *HEXTE*) are useless and a different technique is used: on top of each SSC is a coded mask which produces a complicated shadowgram. As detector a position sensitive proportional counter (PSPC) is used which is sensitive from ~2 keV to 12 keV covering a significant part of the energy band from softer to harder X-rays. A PSPC is very similar to a normal proportional counter except that it has several anodes. Depending on which anode registers the photon, some spatial information can be gained.

The coded mask on top of a *ASM* camera is opaque in certain parts while being transparent in other parts. The result is a distinct "shadow" which is registered by the PSPC. This shadowgram is then used to reconstruct the original sky image. Coded masks are a very complicated subject and the detailed mathematics are very complicated and will therefore not be discussed here. See Proctor et al. (1979) for good introduction into the subject and, e.g., Skinner et al. (1987) and

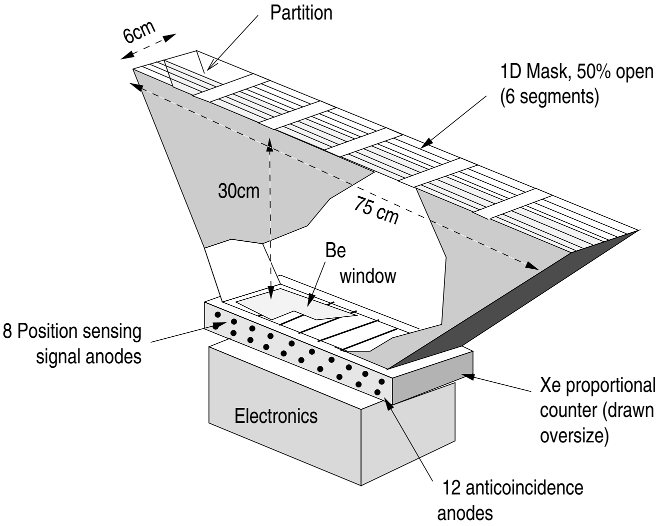
Partition
6cm
1D Mask, 50% open
(6 segments)
30cm
75 cm
Be
window
8 Position sensing
signal anodes
Electronics
Xe proportional
counter (drawn
oversize)
12 anticoincidence
anodes

Figure 4.7: Schematic of one camera of the All Sky Monitor (*ASM*). The *ASM* uses three of these cameras to monitor the complete visible sky (except for the region around the sun) at least once per day. Figure from Wilms (1998).

Willmore et al. (1992) for a description of the analysis methods and mathematics required for coded mask telescopes. The mask of the *ASM* consists of aluminum divided into 6×2 sections. Each of these sections again contains 15 open and 16 closed elements in a carefully chosen pattern. The coded mask technique used by the *ASM* allows a spatial resolution of $3' \times 15'$.

4.3 Software

For data screening and extraction the *FTOOLS* version 5.2 software package provided by NASAs High Energy Astrophysics Science Archive Research Center (HEASARC) was used[2]. For spectral analysis, *XSPEC* (Arnaud 1996) Version 11.2 (usually with a recent patch version; as of now patch level *bl*).

4.3.1 Phase resolved spectroscopy

As discussed in Section 3.3, the observer (i.e. the detectors on *RXTE*) observes the X-ray emitting region of an accreting pulsar under a constantly changing viewing angle due to the rotation of the neutron star. Due to this constantly changing viewing angle, the observed part of the accretion column and X-ray emitting region is also constantly changing. Different parts of the emission region presumably have a different spectrum; therefore it is quite problematic to simply integrate over a whole rotational period of the neutron star. Therefore a different approach is required: *phase resolved spectroscopy* integrates only data from a specific phase of the rotational period.

---

[2] see `http://rosat.gsfc.nasa.gov/docs/software/ftools/ftools_menu.html`.

The *FTOOLS* package include the tool *fasebin* which allows to generate phase resolved spectra from *PCA* and *HEXTE* data. This tool, however, has several major drawbacks:

1. the exposure time per bin for long period pulsars was sometimes completely wrong, sometimes even producing negative exposure times

2. although this tools is able to work on *HEXTE* data in principle, it ignores the *HEXTE* dead time correction. Since the deadtime in the *HEXTE* is usually about 40 %, this also leads to wrong exposure times and thus to wrong background subtraction rendering the resulting spectra unusable

3. the *HEXTE* background could not be phase resolved, which is no problem for pulsars with relatively short periods like Hercules X-1 with a period of ~1.24 s (Pravdo et al. 1978). For pulsars like Vela X-1 (Tsunemi 1989; Deeter et al. 1989, pulse period ~283 s) or GX 301−2 (Nagase et al. 1984, pulse period ~685 s) which are the main objective of this work, a phase resolved background is required since the background can change on timescales of a few seconds, whereas the phase bins in these long period pulsars are easily much longer (in the case of GX 301−2: ~120 s)

4. *fasebin* reads parameters like the pulse period only from the pulsar database, which is sufficient for very stable sources like radio pulsars, whereas accreting X-ray binaries exhibit rapid changes in the pulse period (Oosterbroek et al. 2001; Koh et al. 1997, see, e.g.,), thus requiring constant changes to the database.

Since this tool does not provide usable phase resolved spectra neither for the *PCA* nor the *HEXTE*, an alternative had to be found. Another way to generate phase resolved spectra is to use *good time intervals* (GTI files), which contain the appropriate good times for each phase. This approach, however, is very painful since it requires the generation of dozens of GTI files which again have to be merged with usual *HEXTE* GTI files and so forth. Furthermore this merging may result in very tiny good time intervals and it is not known how the standard extractor handles thousands of these tiny intervals. Therefore we decided to modify the code of *fasebin* appropriately.

I changed the source code in a way that *ikfasebin* is now able

1. to produce phase resolved background spectra for the *HEXTE*. Phase resolved background spectra for the *PCA* are not possible, since the *PCA* background data uses a 16 s time resolution and a data mode not supported by *(ik)fasebin*.

2. to produce correct exposure times for *PCA* data by removing a bug in the subroutine responsible for the calculation of the exposure time for binned *PCA* modes.

3. to create also dead time histograms for the *HEXTE* such that *HEXTE* spectra now also take the dead time into account

Wayne Coburn from CASS/UCSD (now at the Space Science Laboratory, UC Berkeley, Berkeley) enabled *ikfasebin* to read some pulsar parameters not only from the database, but also from command line. He and Rodina Liubov were very helpful with testing *ikfasebin* with many different sources and validating the results of *ikfasebin*.

Since the ability of *ikfasebin* to take the dead time of *HEXTE* into account is completely new and not very simple to implement, the procedure shall be described in the following.

A *HEXTE* light-curve generated by the standard *FTOOL seextract* contains the deadtime correction factor for every instrument data frame (IDF) which is 16 s long. A dead time histogram is accumulated along with the normal spectral histogram for each phase bin. These contributions to the histogram are computed from the dead time correction factors in a *HEXTE*-lightcurve with a resolution of 0.1 s (this parameter can also be changed by the user from command line, but a resolution of 0.1 s worked very well for all tested observations). After the accumulation is complete, an average dead time correction factor is derived for each phase bin.

ikfasebin was tested thoroughly using different sources and exposure times; the difference of the resulting total exposure time of the phase resolved and phase-averaged spectra is usually less than 0.1%. Apart from Vela X-1, the tool has successfully been used to create phase-resolved spectra of X-Per and for several other X-ray pulsars (Coburn et al. 2001; Coburn 2001; Heindl et al. 2000).

The code has not yet been made public by putting it on the World Wide Web pages, but it is available upon request.

CHAPTER 5

Confirmation of two cyclotron lines in Vela X-1

In this chapter, pulse phase-resolved X-ray spectra of the high mass X-ray binary Vela X-1 using the Rossi X-ray Timing Explorer are presented. This chapter is focused mainly on the discussion of the existence of two cyclotron resonant scattering features observed in the spectrum of Vela X-1. Special emphasis is put on the first line at ~24 keV as the existence of this line has been strongly debated in the past and is still a matter of discussion since it was not observed in *BeppoSAX* data (La Barbera et al. 2003). This chapter provides evidence that a spectral feature is indeed present at ~24 keV which is interpreted as the fundamental cyclotron line.

Since this chapter is based on the publication Kreykenbohm et al. (2002a), it adopts a similar structure and also adopts the "we-style" used in that paper.

The remainder of this chapter is structured as follows: Sect. 5.2 describes the relevant calibration issues, the software used for the analysis, and the data. Sect. 5.3 gives an overview of the spectral models used, introduces pulse phase resolved spectroscopy, and discusses the evolution of the spectral parameters over the pulse in 16 phase bins. Later we use fewer bins to increase the significance and discuss the behavior of the 25 keV and 50 keV CRSFs in different pulse phases. In Sect. 5.4 we discuss the existence of the 25 keV line and review our findings in the context of the other cyclotron sources.

5.1 Introduction

Vela X-1 (4U 0900−40) is an eclipsing high mass X-ray binary (HMXB) consisting of the B0.5Ib supergiant HD 77581 and a neutron star with an orbital period of 8.964 days (van Kerkwijk et al. 1995) at a distance of ~2.0 kpc (Nagase 1989). The optical companion has a mass of ~23 $M_\odot$ and a radius of ~30 $R_\odot$ (van Kerkwijk et al. 1995). Due to the small separation of the binary system (orbital radius: 1.7 R_*), the 1.4 $M_\odot$ neutron star (Stickland et al. 1997) is deeply embedded in the intense stellar wind ($4 \times 10^{-5}\,M_\odot\,\mathrm{yr}^{-1}$; Nagase et al. 1986) of HD 77581.

The neutron star has a spin period of ~283 s (Rappaport & McClintock 1975; McClintock et al. 1976). Both spin period and period derivative have changed erratically since the first measurement as is expected for a wind accreting system. The last measurements with the Burst and Transient Source Experiment[1] (*BATSE*) resulted in a period of ~283.5 s.

The X-ray luminosity of Vela X-1 is ~$4 \times 10^{36}\,\mathrm{erg\,s}^{-1}$, which is a typical value for an X-ray binary. Several observations have shown that the source is extremely variable with flux reductions to less than 10% of its normal value (Kreykenbohm et al. 1999; Inoue et al. 1984). In these instances it is not known whether a clump of material in the wind blocks the line of sight or if the accretion itself is choked.

The phase averaged X-ray spectrum of Vela X-1 has been modeled with a power law including an exponential cutoff (White et al. 1983; Tanaka 1986) or with the Negative Positive EXponential (NPEX-model; Mihara 1995, see also Eq. 5.1 below). The spectrum is further modified by strongly varying absorption which depends on the orbital phase of the neutron star (Kreykenbohm et al. 1999; Haberl & White 1990), an iron fluorescence line at 6.4 keV, and occasionally an iron edge at 7.27 keV (Nagase et al. 1986). A cyclotron resonant scattering feature (CRSF) at ~55 keV was first reported from observations with *HEXE* (Kendziorra et al. 1992). Makishima et al. (1992) and Choi et al. (1996) reported an absorption feature at ~25 keV to 32 keV from *Ginga* data. Kreykenbohm et al. (1999) using observations with the Rossi X-ray Timing Explorer (*RXTE*) and more detailed analysis of older *HEXE* and *Ginga* data (Kretschmar et al. 1996; Mihara 1995) supported the existence of both lines, while Orlandini et al. (1998a) reported only one line at ~55 keV based on *BeppoSAX* observations. Later observations with *RXTE* also cast some doubt on the existence of the 25 keV line (Kreykenbohm et al. 2000).

---

[1] See `http://www.batse.msfc.nasa.gov/batse/pulsar/data/sources/velax1.html`

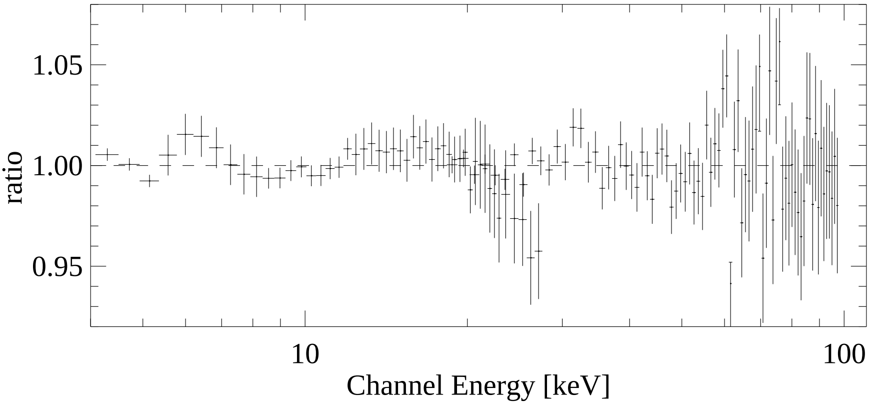

Figure 5.1: Ratio of PCA and HEXTE data to the best fit model for a Crab observation (obsid 40805-01-05-01, 1999 December 12). The two power laws, which represent the nebula and pulsar, had photon indices $\Gamma_1 = 2.25^{+0.03}_{-0.03}$ and $\Gamma_2 = 1.88^{+0.05}_{-0.03}$ respectively. A single power law model gave $\Gamma = 2.13 \pm 0.02$, which is in agreement with recent observations by *XMM-Newton* (Willingale et al. 2001). The *PCA* response matrix was created with *PCARSP 2.43*.

5.2 Data

We observed Vela X-1 with the *RXTE* in 1998 and again in 2000. The first observation in *RXTE*-AO3 was made 1998 January 21 (JD 2450835.32) to January 22 (JD 2450836.05) resulting in 30 ksec on-source time. During this observation we encountered an extended low (see Fig. 5.2); therefore we only used data taken after the extended low, starting about 8 hours after the beginning of the observation at JD 2450835.64 (see Fig. 5.2). The second observation was in *RXTE*-AO4 and took place 2000 February 03/04 (JD 2451577.71 – JD 2451579.22) resulting in 60 ksec on-source time. Figs. 5.2 and 5.3 show the *PCA* light-curves of the 1998 and 2000 observations.

For a detailed description of the *RXTE* and its instruments, see Chapter 4. Only the topic specific to this analysis will be discussed shortly in the following.

For the *PCA*, the response matrix was generated with *PCARSP*, version 2.43. To account for the uncertainties in the *PCA*-response matrix, we used systematic errors as given in Table 5.1. These numbers were derived by fitting a two power law model simultaneously to a *PCA* and *HEXTE* spectrum of the Crab nebula and pulsar (see Fig.5.1). See Wilms et al. (1999) for a discussion of this procedure.

After the analysis was completed and while this publication was in preparation, *FTOOLS Patch 5.0.4* was released, introducing *PCARSP* version 7.10. Tests

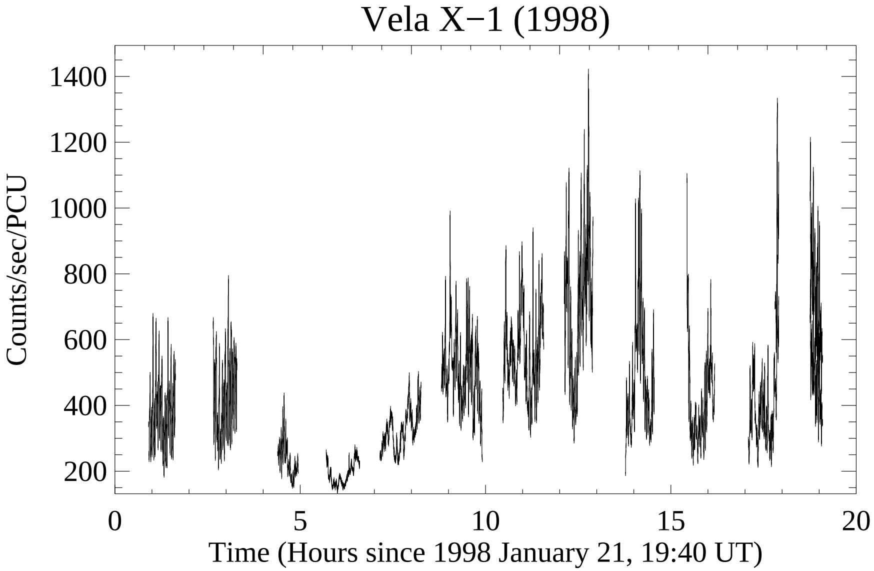

Figure 5.2: RXTE PCA light-curve of the 1998 observation. The variability is not only due to the flaring, but also due to the 283 s pulse. In this and all following light-curves, the count rate has been normalized to one PCU. The temporal resolution of the light-curves is 16 s and covers the entire energy range of the *PCA*. The gaps in the light-curve are due to Earth occultation and passages through the South Atlantic Anomaly. Note the extended low in the first half of the observation: it is probably due to a massive blob of cold material passing through the line of sight. As this paper is dedicated to phase-resolved spectroscopy and the existence of the CRSFs, this data was excluded from our analysis and we do not discuss this phenomenon here. For a detailed discussion, see Kretschmar et al. (1999). After the extended low, Vela X-1 was flaring and remained so until the end of the observation.

using the new response matrix, however, show that the best-fit parameters are only marginally different compared to the old matrices, with the only difference being a ~30% larger value of the hydrogen column and virtually no difference at higher energies.

Our light-curves and phase-resolved spectra were obtained from binned mode data with a temporal resolution of 250 ms and 128 spectral channels. Due to the gain correction present in these data in the PCA experiment data system, some pulse height analyzer (PHA) channels remain empty. This problem is known and handled properly by *PCARSP* (Tess Jaffe, priv. comm.). For clarity, these zero counts/sec channels are not shown in our figures. We therefore used the *PCA* in

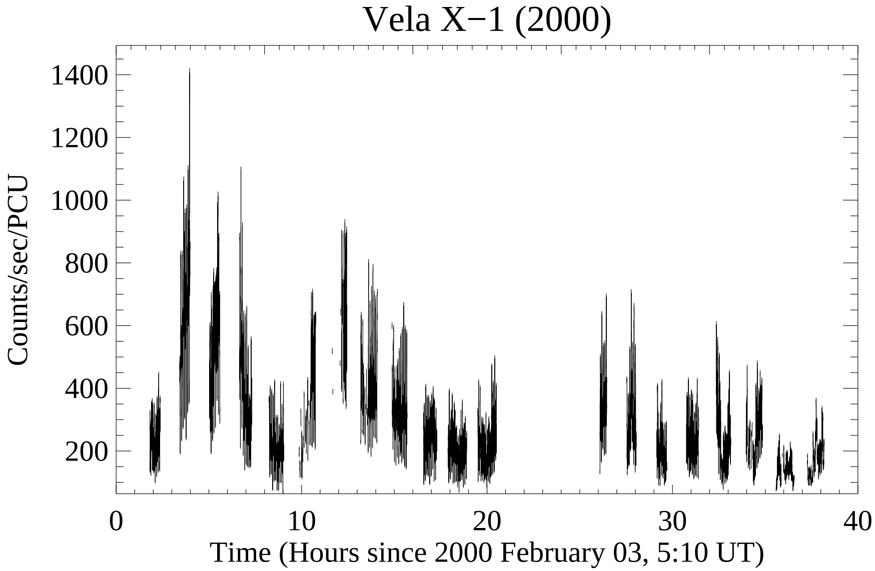

Figure 5.3: RXTE PCA light-curve of the 2000 observation as for the 1998 observation in Fig. 5.2. Gaps in the light-curve are due to SAA, Earth occultation, and *RXTE* observing other sources.

the energy range from 3.5–21 keV (corresponding to PHA channels 6–45) in our analysis and relied on the *HEXTE* data above this energy range.

For the *HEXTE*, the response matrices were generated with *HXTRSP*, version 3.1. We used *HXTDEAD* Version 2.0.0 to correct for the dead time. To improve the statistical significance of our data, we added the data of both *HEXTE* clusters and created an appropriate response matrix by using a 1:0.75 weighting to account for the loss of a detector in the second cluster. This can be safely done as the two cluster responses are very similar. To further improve the statistical significance of the *HEXTE* data at higher energies, we binned several channels together as given in Table 5.2. We chose the binning as a compromise between increased statistical significance while retaining a reasonable energy resolution. The binning resulted in statistically significant data from 17 keV up to almost 100 keV (we detect the source at ~75 keV with a $3\,\sigma$ significance in the pulse phase resolved spectra and $5\,\sigma$ in the phase averaged spectra) in the 2000 observation.

All analysis was done using the *FTOOLS* version 5.0.1 dated 2000 May 12. We used *XSPEC* 11.0.1aj, (Arnaud 1996) with several custom models (see below,

Table 5.1: Systematic errors applied to the *PCA*-data to account for the uncertainties in the 2.43 and 7.10 version of the *PCA* response matrices. We used the response matrix generated by *PCARSP 2.43* to derive the results presented here (see text).

Channels	keV	Syst. (2.43)	Syst. (7.10)
0 – 9	1 – 5	1.0%	0.3%
10 – 15	5 – 8	1.0%	1.3%
16 – 26	8 – 12	0.5%	1.3%
27 – 39	12 – 18	0.5%	0.3%
40 – 58	19 – 30	2.0%	2.0%

Sect. 5.3.1) for the spectral analysis of the data. To create phase-resolved spectra we modified the *FTOOL fasebin*, to take the *HEXTE* dead-time into account. For a more detailed description of this tool and the changes, see Section 4.3.1.

5.3 Spectral Analysis

5.3.1 Spectral Models

Since probably all accretion powered X-ray pulsars have locally super-Eddington flux at the polar cap (Nagase 1989), a realistic, self-consistent calculation of the emitted spectrum is extremely difficult. Both radiative transfer and radiation hydrodynamics have to be taken into account at the same time (Isenberg et al. 1998b). Although this problem has been investigated for many years, there still exists no convincing theoretical model for the continuum of accreting X-ray pulsars (Harding 1994, and references therein). Most probably, the formation of the overall spectral shape is dominated by *resonant* Compton scattering (Nagel 1981b; Mészáros & Nagel 1985; Brainerd & Mészáros 1991; Sturner & Dermer

Table 5.2: Binning of the *HEXTE* data. We chose the binning to get good statistical significance for each bin while also maintaining good energy resolution. Therefore we did not bin the channels below 40 keV. Factor is the number of channels binned together. Raw channels are approximately 1 keV in width.

Channels	Factor
1 – 39	1
40 – 69	3
70 – 109	8
110 – 255	32

1994; Alexander et al. 1996). This should produce a roughly power-law continuum with an exponential cutoff at an energy characteristic of the scattering electrons. Deviations should appear at the cyclotron resonant energy, i.e. the cyclotron lines. Because the process is resonant scattering, as opposed to absorption, it is natural to call “cyclotron lines” “cyclotron resonant scattering features”. Because of the computational complexities associated with modeling the continuum and CRSF formation, this type of Comptonization has been far less studied than *thermal* Comptonization (Sunyaev & Titarchuk 1980; Hua & Titarchuk 1995), and empirical models of the continuum continue to be the only option for data analysis.

Due to the general shape of the continuum spectrum, the empirical models all approach a power-law at low energies, and have some kind of cutoff at higher energies (White et al. 1983; Tanaka 1986). The CRSFs are either modeled as subtractive line features or through multiplying the continuum with a weighting function at the cyclotron resonant energy. As we have shown previously (Kretschmar et al. 1997), a smooth transition between the power law and the exponential cutoff is necessary to avoid artificial, line-like features in the spectral fit. This transition region is notoriously difficult to model. See Kreykenbohm et al. (1999) for a discussion of spectral models with smooth “high energy cutoffs”, such as the Fermi-Dirac cutoff (Tanaka 1986) used in our analysis of the AO1 data (Kreykenbohm et al. 1999), and the Negative Positive Exponential model (NPEX; Mihara 1995; Mihara et al. 1998).

In this paper, we describe the continuum of Vela X-1, I_{cont}, using the NPEX model,

$$I_{\mathrm{cont}}(E) \propto \left(E^{-\Gamma_1} + \alpha E^{+\Gamma_2}\right) \times \mathrm{e}^{-E/E_{\mathrm{F}}} \tag{5.1}$$

where $\Gamma_1 > 0$ and $\Gamma_2 = 2$ (Mihara 1995) and where E_{F} is the folding energy of the high energy exponential cutoff. In our experience, this model is the most flexible of the different continuum models. For Vela X-1, the continuum between 7 and 15 keV is better described with the NPEX model than the Fermi-Dirac cutoff. The CRSFs are taken into account by a multiplicative factor

$$I(E) \propto I_{\mathrm{cont}} \exp(-\tau_{\mathrm{GABS}}(E)) \tag{5.2}$$

where the optical depth, τ_{GABS}, has a Gaussian profile (see Coburn et al. 2002, Eqs. 6,7),

$$\tau_{\mathrm{GABS}}(E) = \tau_{\mathrm{C}} \times \exp\left(-\frac{1}{2}\left(\frac{E - E_{\mathrm{C}}}{\sigma_{\mathrm{C}}}\right)^2\right) \tag{5.3}$$

Here E_{C} is the energy, σ_{C} the width, and τ_{C} the optical depth of the CRSF.

We note that the relationship between the parameters of the empirical continuum models and real physical parameters is not known. Because thermal Comptonization spectra get harder with an increasing Compton-y-parameter, it seems reasonable to relate the characteristic frequency of the exponential cutoff, E_F, with some kind of combination between the (Thomson) optical depth and the temperature (see, e.g., Mihara et al. 1998). Because of the complexity of the continuum and line formation, however, we caution against a literal interpretation of any of the free parameters that enter these continuum models, and will not attempt to present any interpretation here (note, however, that the cyclotron line parameters do have a physical interpretation).

5.3.2 Pulse Phase-resolved spectra

During the accretion process, material couples to the strong magnetic field of the neutron star at the magnetospheric radius. This material is channeled onto the magnetic poles of the neutron star, where spots on the surface of the neutron star are created (Burnard et al. 1991, and references therein). If the magnetic axis is offset from the spin axis, the rotation of the neutron star gives rise to pulsations (Davidson & Ostriker 1973), as a distant observer sees the emitting region from a constantly changing viewing angle. Because the emission is highly aniostropic, the spectra observed during different pulse phases vary dramatically. This is especially true for CRSFs whose characteristics depend strongly on the viewing angle with respect to the magnetic field (for an in-depth discussion see Araya-Góchez & Harding 2000; Araya & Harding 1999; Isenberg et al. 1998b, and references therein). This dependence can in principle be used to infer the geometric properties of the emission region and the electron temperature.

To obtain phase-resolved spectra, the photon or bin times were bary-centered and corrected for the orbital motion of Vela X-1 using the ephemeris of Nagase (1989). Then the pulse phase was calculated for each time bin (for the *PCA*) or for each photon (for the *HEXTE*) and then attributed to the appropriate phase bin. Using epoch folding (Leahy et al. 1983), we determined the pulse period for each observation individually. We derived pulse periods of $P_\mathrm{pulse} = 283.5 \pm 0.1\,\mathrm{s}$ for the 1998 data and $P_\mathrm{pulse} = 283.2 \pm 0.1\,\mathrm{s}$ for the 2000 data (using JD2444279.546637 as the zero phase for both observations).

Since the first detection of pulsations from Vela X-1 by McClintock et al. (1976), the pulse profile is known to be very complex. Above 20 keV, the pulse profile consists of two peaks which are about equally strong. Since Vela X-1 has a relatively hard spectrum, Staubert et al. (1980) were able to detect the two pulses up to 80 keV. We designate these two pulses as the *main pulse* and the *secondary pulse* (see Fig. 5.4 for the definition).

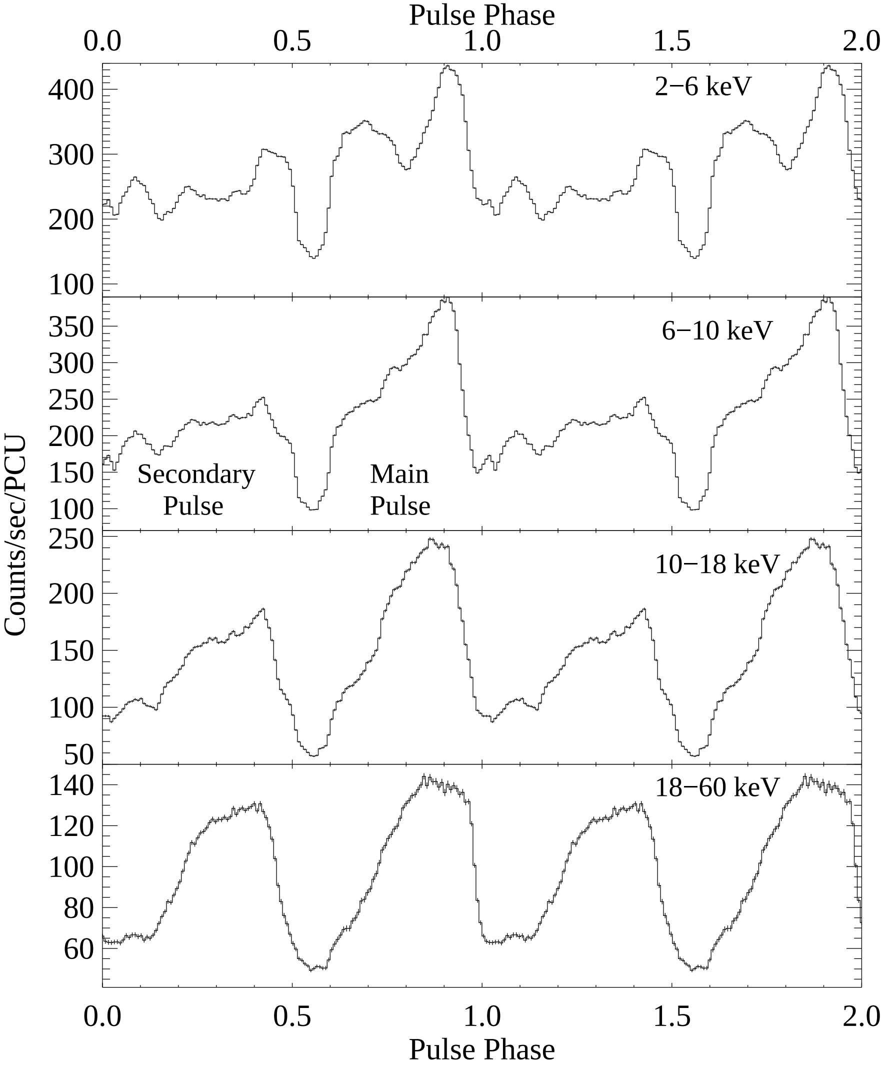

Figure 5.4: Energy resolved pulse profiles in four bands derived from the 2000 data. At lower energies (below 6 keV), the pulse profile is very complex and shows a five peaked structure: two peaks in the main pulse and three in the secondary pulse. Between 6 keV and 10 keV, the first peak of the main pulse is reduced to a mere shoulder, while the second peak is very strong. Above 10 keV the pulse profile evolves continuously into a simple double pulse.

Below 5 kev, these two pulses evolve into five peaks: the main pulse develops into two peaks while the secondary pulse develops into three peaks. Although the two pulses are almost equally strong at high energies, the second peak of the main pulse is almost a factor of two brighter at lower energies than the first two peaks of the secondary pulse, while the third peak of the secondary pulse is almost as strong as the first peak of the main pulse. For a detailed description of the pulse profile and the relative intensities of the different peaks, see Raubenheimer (1990) and Sect. 5.4.1.

In the following we first study the evolution of the continuum parameters (i.e., the NPEX-model and the photo-electric absorption) and then concentrate on the behavior of the CRSFs in the 2000 and 1998 observations using fewer phase bins.

5.3.2.1 Spectral Evolution over the Pulse

We used 16 phase bins for the 1998 as well as the 2000 data. The better statistics of the 2000 observation would allow finer resolution (e.g., 32 phase bins) but would make the comparison of the observations more difficult.

The phase resolved spectra were again modeled using the NPEX continuum with $\Gamma_2 = 2$, modified by photoelectric absorption, an iron line at 6.4 keV, and the CRSF at 50 keV. The evolution of the relevant spectral parameters is shown as a function of pulse phase in Figs. 5.5 and 5.6 for the 1998 and 2000 data, respectively. Note that in this section, the emphasis is on the evolution of the continuum parameters. The CRSFs will be discussed in detail in the next two sections.

The spectral evolution over the pulse of the two observations is somewhat different (see Figs. 5.5 and 5.6): in the 1998 data, N_H varies between $15\times10^{22}\,\mathrm{cm}^{-2}$ and $26\times10^{22}\,\mathrm{cm}^{-2}$ and shows a clear correlation with flux (linear correlation coefficient $r = 0.75$; Bevington & Robinson 1992, Eq. 11.17). In the 2000 data, N_H is lower by a factor of 10 and consistent with a constant value ($r = 0.21$).

While not shown, the iron line is extremely stable within each observation: its energy, width, and normalization show no variation with pulse phase or flux. As the iron line is believed to be due to fluorescence in the gas surrounding the Vela X-1/HD 77581 system (Ohashi et al. 1984), this is not surprising. While the equivalent width of the iron line in the 1998 data is 1.3 keV it is only 250 eV in the 2000 data. This is consistent with the overall absorption in the 1998 data being much higher than in the 2000 data thus suppressing the continuum. Since the Fe line originates from a much larger region and is less affected by the local absorption in the area surrounding the neutron star, one would expect the line flux to follow the average source flux.

In the 1998 data, the folding energy of the NPEX-model is variable with pulse

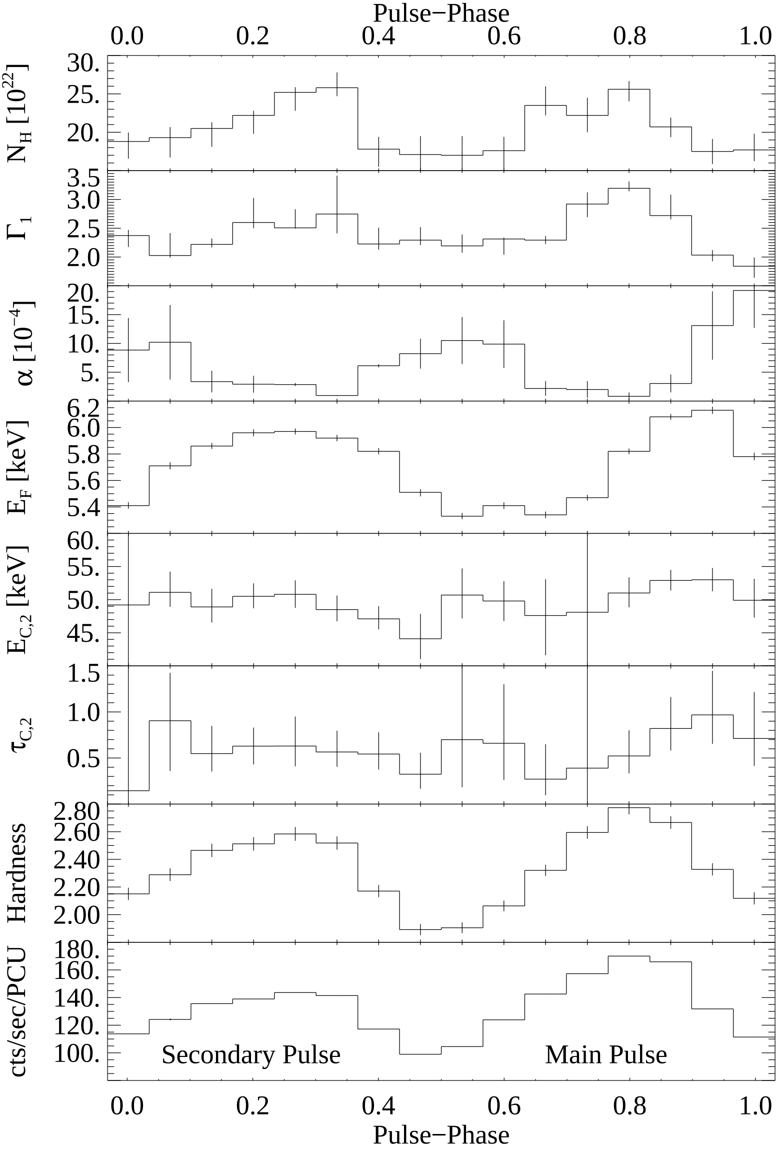

Figure 5.5: Evolution of the fit parameters over the pulse for the 16 phase-bins for the 1998 data. The energy ranges, the spectral hardness, and the other parameters are defined in the text. The vertical bars indicate the uncertainties at 90% confidence level.

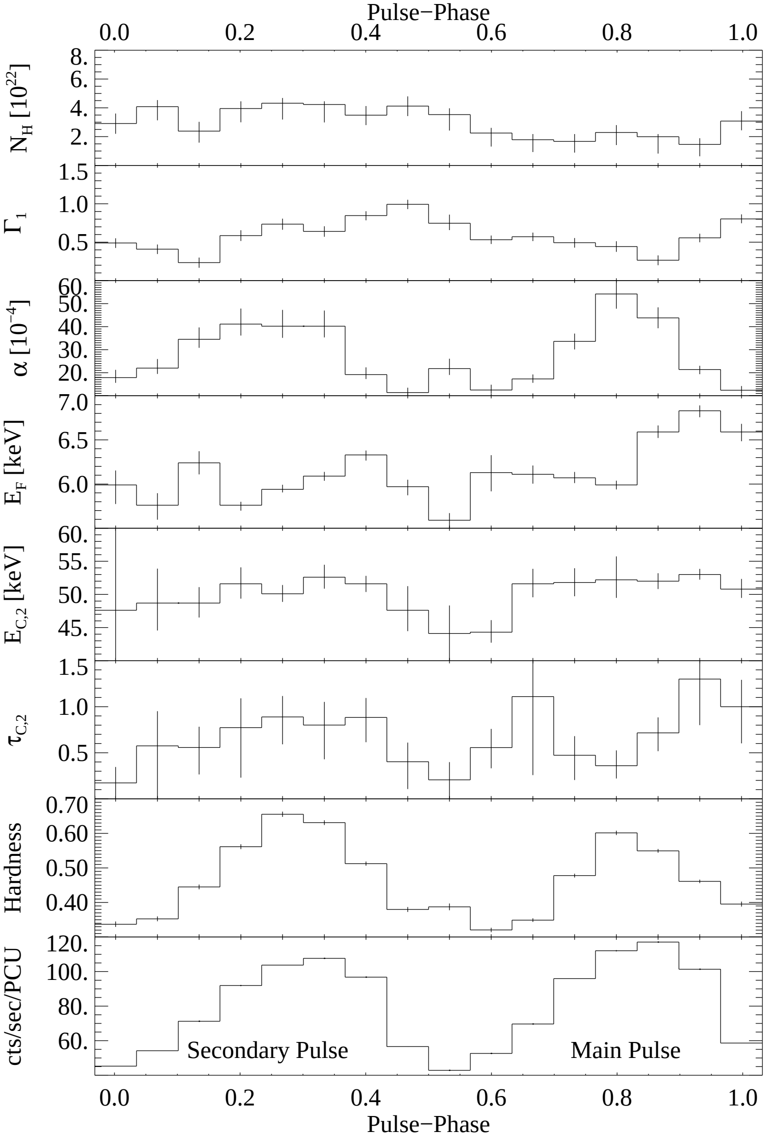

Figure 5.6: Evolution of the fit parameters over the pulse for the 16 phase-bins for the 2000 data. The spectral hardness, the other parameters, and energy ranges are defined as in Fig. 5.5. The vertical bars indicate the uncertainties at 90% confidence level.

phase: it correlates strongly with the flux in the secondary pulse (correlation coefficient $r = 0.89$), while there is no such correlation in the main pulse ($r = 0.16$). In the 2000 data, this correlation is much less pronounced: $r = 0.45$ for the secondary pulse and $r = 0.14$ for the main pulse. The photon index Γ_1 of the NPEX model varies over the pulse, but is only correlated with flux in the 1998 data ($r = 0.76$). No such correlation is present in the 2000 data ($r = 0.21$): its value in most phase bins is consistent with 0.6, which is about a factor of 4 smaller than in the 1998 data. Although the χ^2 contours of N_H versus Γ_1 are somewhat elongated, we note that it is impossible to fit the 2000 data with values of Γ_1 and N_H similar to the 1998 data. Such an attempt results in $\chi^2 > 3500$ (66 dof). The relative normalization of the negative power law component of the NPEX model (see Eq. 5.1), α, varies significantly over the pulse: while there is no clear correlation with flux present in the 1998 data, the 2000 data is clearly correlated with flux ($r = 0.75$). The hardness ratio again shows a very strong correlation with flux in the 1998 data ($r = 0.95$) and in the 2000 data ($r = 0.88$). The spectral hardness is defined as $R = H/S$ where S is the total rate in the 2.5–10 keV band and H is total rate in the 15–20 keV band. The *PCA* countrate is in the energy range from 15–20 keV and shows clearly the Vela X-1 double pulse.

Summarizing this section, we found that the two observations are somewhat different. In the 1998 data, the absorption column N_H, the photon index Γ_1, the folding energy of the NPEX model, and the hardness ratio are correlated with flux, while all the iron line parameters and the relative normalization α of the NPEX model are not correlated with flux. In the 2000 data, however, the relative normalization of the NPEX model, and the hardness ratio are correlated with flux, while the other parameters are not.

5.3.2.2 The CRSFs in the 2000 data

Although the 16 phase bins provide good temporal resolution, the relatively low exposure time per bin results in only mediocre statistics. Therefore we reduced the number of phase bins to obtain better statistical quality per bin. For the 2000 data, spectra were obtained for the rise, center, and fall of the main pulse, for the rise, center, and fall of the secondary pulse, and for the two pulse minima (see Fig. 5.7 for the definition of the individual bins). Henceforth, we identify these phase bins with *capital* letters.

We used our standard continuum model to analyze the data; since these sections are commited to the CRSFs, we only quote the interesting spectral parameters here (a table of all spectral fits is available in Appendix A).

The well known CRSF at $52.8^{+1.9}_{-1.4}$ keV is strongest in the fall of the main pulse with a depth of $\tau_{\mathrm{C},2} = 1.1^{+0.3}_{-0.2}$ (F-Test: 2.9×10^{-14}). In the center of the main pulse

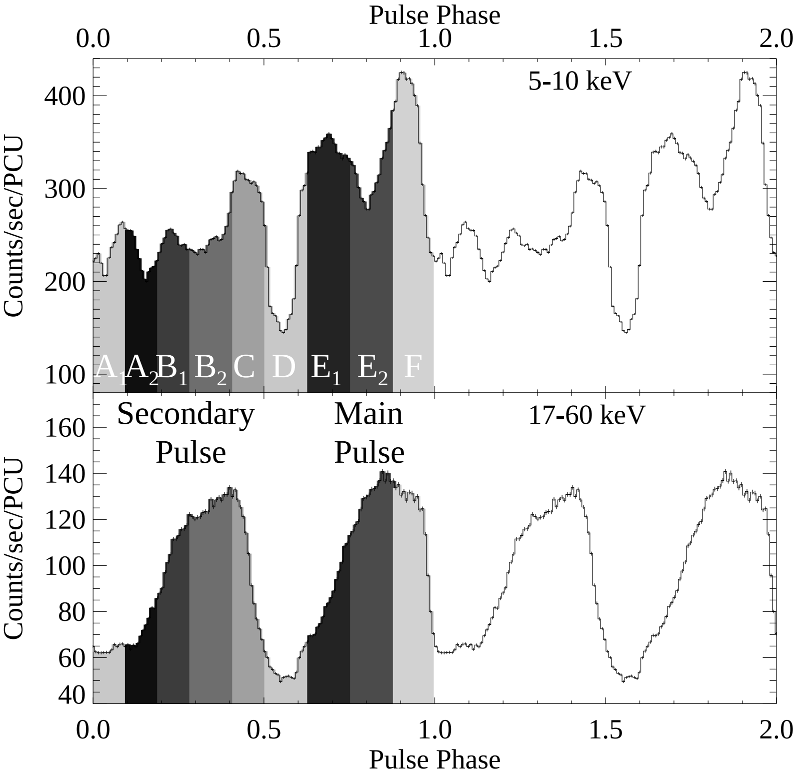

Figure 5.7: Folded light curves (FLCs) of the 2000 data and definition of the nine phase bins obtained from the 2000 data. As in Fig. 5.13, we show the complex low energy pulse profile in the upper panel and the simpler high energy pulse profile in the lower panel. Due to the evolution of the pulse period, the FLCs of the 2000 data are somewhat offset compared to the 1998 data FLCs. Note that due to the higher statistics we used nine phase bins in the 2000 data instead of six for the 1998 data. For clarity, the folded light-curve is shown twice. Note that error-bars *are* shown, but in most cases they are too small to be seen in print.

(bin E_2), it is somewhat less deep than in the fall ($\tau_{C,2} = 0.5^{+0.3}_{-0.1}$; see Fig. 5.9). In the rise of the main pulse (bin E_1) it is again of similar depth as in the fall ($\tau_{C,2} = 1.0^{+0.4}_{-0.3}$, see Fig. 5.9).

In the secondary pulse, the CRSF is on average less deep than in the main pulse and the depth is – within uncertainties – consistent with a constant value of 0.6

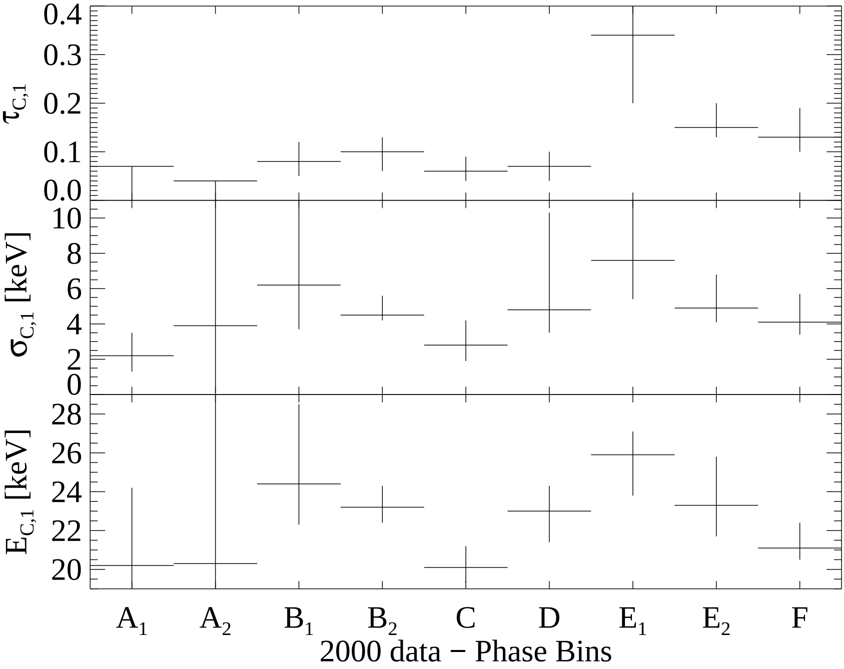

Figure 5.8: Evolution of the depth, the width, and the energy of the CRSF at 23 keV for the nine phase bins of the 2000 observation. The vertical bars indicate the uncertainties at the 90% (2.7σ) confidence level. For discussion, see text.

throughout the secondary pulse (bins A_1 to C). In the fall (bin C) it has a depth of $\tau_{C,2} = 0.5^{+0.2}_{-0.2}$, but it is still very significant (F-Test: 1.8×10^{-6}). In the center it is of similar depth ($\tau_{C,2} = 0.6^{+0.2}_{-0.2}$) and also very significant (F-Test: 3.7×10^{-11}). In the rise (bin B_1) the depth $\tau_{C,2} = 0.8^{+0.3}_{-0.2}$ is somewhat greater, but still consistent with a a value of 0.6.

In the pulse minima the significance of the CRSF is low (bin D, F-Test: 2.8×10^{-2}) or insignificant (bin A_1; F-Test: 0.59). In both cases the depth of the line is $\tau_{C,2} \leq 0.4$ with a lower limit < 0.15 and an upper limit of 0.5. Fig. 5.9 shows the fundamental and harmonic CRSF optical depths in our nine phase bins of the 2000 observation. Given these optical depth measurements and upper limits, we find that in the main pulse, the line is strongest on the rising and falling edges, while it is of similar strength throughout the secondary pulse. Finally, the line is weakest, if indeed present at all, in the pulse minima.

However, after fitting the CRSF at 50 keV, the fit is still not acceptable in most

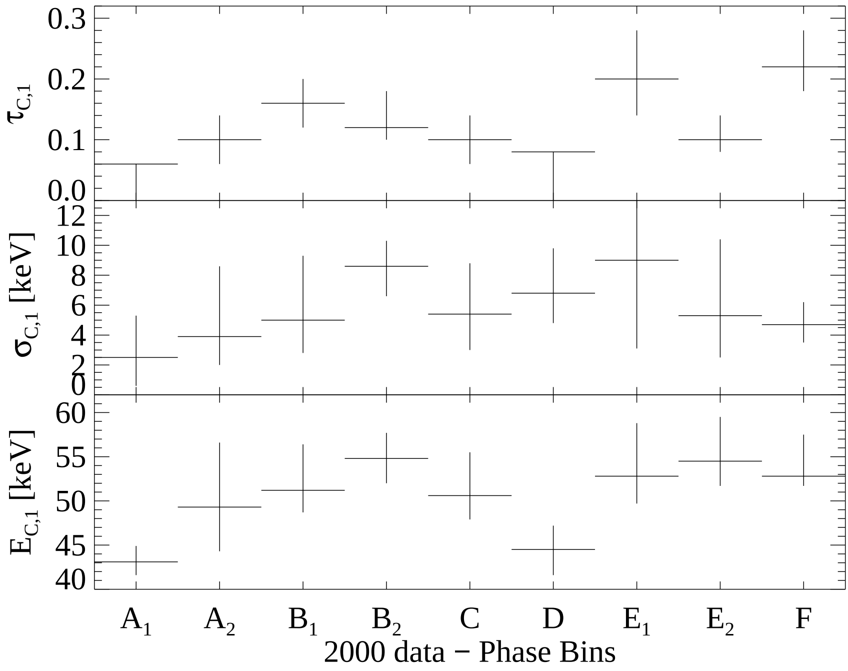

Figure 5.9: Evolution of the depth, the width and the energy of the CRSF at 50 keV for the nine phase bins of the 2000 observation. The vertical bars indicate the uncertainties at the 90% (2.7σ) confidence level. For discussion, see text.

phase bins: there is another absorption line like structure present at about 25 keV. The most straight-forward explanation for this feature is that it is a CRSF. After adding a second CRSF component to our models, the resulting fits are very good. However, as the resulting CRSFs are usually relatively shallow, we also investigated other possibilities to fit this feature, most notably we tried other continuum models like the Fermi-Dirac cutoff. But these models were either completely unable to describe the data (e.g. thermal bremsstrahlung or the cutoffpl, a power-law multiplied by an exponential factor), known to produce artificial absorption lines like the high energy cutoff (White et al. 1983) or – as in the case of the Fermi-Dirac cutoff – also produced an absorption line like feature at 25 keV. The wiggle between ~8 keV and 13 keV, which is present in the 2000 and the 1998 data, is also present in many other *RXTE* observations of accreting neutron stars (Coburn et al. 2002). It usually has the form of a small dip around 10 keV followed by a small hump at 12 keV (see for instance, Fig. 5.11); it, however, is very variable. It

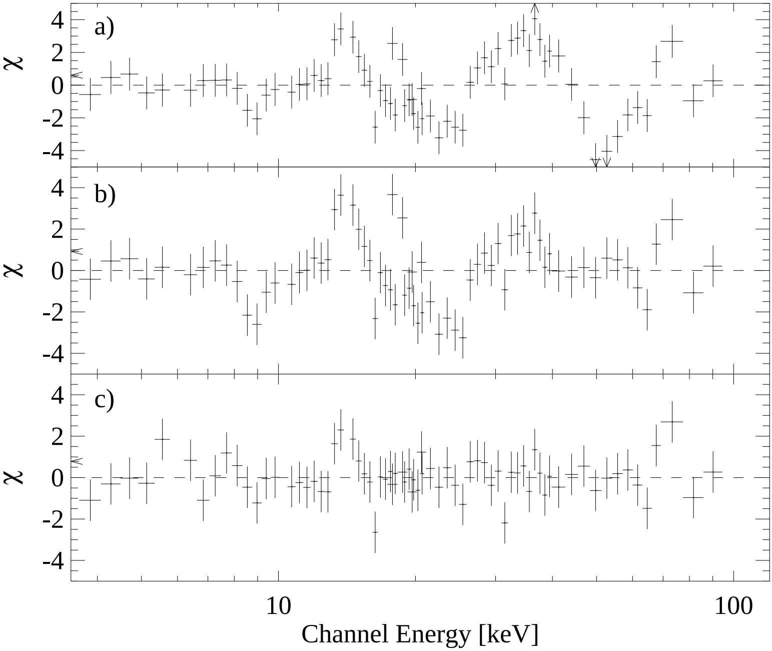

Figure 5.10: Residuals of fits to the spectrum of the *center of the main pulse* (bin E_2) of the 2000 data. **a** for a model without cyclotron absorption lines, **b** with one line at $53.8^{+2.5}_{-1.9}$ keV, and **c** with two lines at $23.3^{+1.3}_{-0.6}$ keV and $54.5^{+5.2}_{-2.9}$ keV. Note the feature at 23 keV in **b**, which we interpret as the fundamental cyclotron absorption line. This line is deepest in the rise and most significant in the center of the main pulse and shallower in the other phase bins (see Fig. 5.12 and text for discussion).

is present in most phase bins (and in phase averaged spectra), but shows no clear phase dependence. This phenomenon is yet unexplained, but it is unrelated to the feature at 25 keV, since this wiggle appears in many sources at more or less at the same energy where no CRSF is found at 25 keV. We therefore conclude that the feature at 25 keV is real and interpret it as a CRSF.

The behavior of the feature at 25 keV is quite similar to the 50 keV CRSF. We found that the 25 keV line is most significant in the center of the main pulse (bin E_2): the inclusion of a CRSF at $23.3^{+1.3}_{-0.6}$ keV improves the fit significantly (F-Test: 2.9×10^{-13}). The depth of this line is 0.15, with a lower limit of 0.13. In the *rise* of the main pulse (bin E_1), the CRSF at $25.9^{+2.4}_{-1.7}$ keV is clearly present and significant (F-Test: 2.8×10^{-7}). With a depth of $\tau_{C,1} = 0.33^{+0.06}_{-0.13}$ it is also deeper than in the center. However, in the fall (bin F), where the 50 keV line is

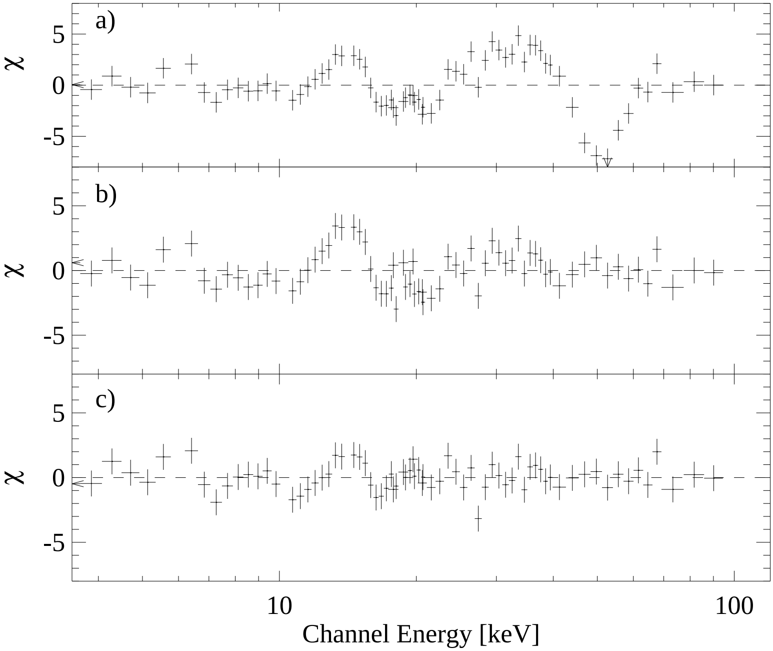

Figure 5.11: Residuals of fits to the spectrum of the fall of the main pulse (bin F) of the 2000 data. **a** for a model without cyclotron absorption lines, **b** with one line at $52.8^{+1.6}_{-1.2}$ keV, and **c** with two lines at $21.1^{+0.6}_{-0.7}$ keV and $52.7^{+2.0}_{-1.4}$ keV. The absorption feature at 23 keV in **a** and **b** is much weaker than in the center of the main pulse (see Fig. 5.10), while the 50 keV line is more prominent in this phase bin than in any other phase bin.

most prominent, the fundamental line is detected with high significance (F-Test: 4.2×10^{-9}), but it is not as deep as in the rise: $\tau_{\mathrm{C},1} = 0.13^{+0.05}_{-0.02}$ (see Figs. 5.8 and 5.11).

We found that there is also a significant (F-Test: $<5\times10^{-5}$) CRSF present at 23 keV throughout the secondary pulse ($\mathrm{B}_{1,2}$ and C). As shown in Fig. 5.8, the line is of similar depth throughout the secondary pulse: from $\tau_{\mathrm{C},1} = 0.06^{+0.03}_{-0.02}$ in the fall to $\tau_{\mathrm{C},1} = 0.10^{+0.03}_{-0.03}$ in the center, where it is also most significant (F-Test: 5.6×10^{-10}). In any case, the line is somewhat shallower than in the main pulse.

In the pulse minimum *after* the main pulse (bin A_1), an absorption feature at 25 keV is not visible in the residuals and the inclusion of a line at $22.6^{+2.9}_{-3.0}$ keV does not result in an improvement (F-Test: 0.29). The upper limit for the depth of this line is 0.10. However, in the pulse minimum *before* the main pulse (bin D), the residuals show a shallow absorption feature and the inclusion of a CRSF at

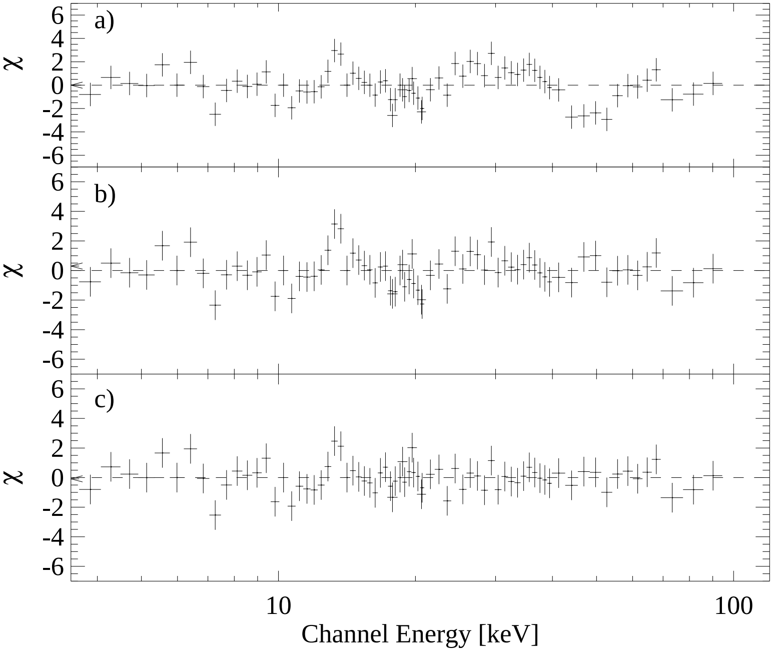

Figure 5.12: Residuals of fits to the fall of the *secondary* pulse (bin C) of the 2000 data. **a** for a model without cyclotron absorption lines, **b** with one absorption line at $50.4^{+3.9}_{-2.5}$ keV, and **c** with two lines at $20.1^{+1.4}_{-1.7}$ keV and $50.5^{+6.2}_{-3.0}$ keV. The improvement due to the second line at 20 keV is very small; in fact, after the inclusion of the 50 keV line no absorption line feature is visible in **b**.

$20.2^{+1.3}_{-1.7}$ keV with a depth of $\tau_{\mathrm{C},1} = 0.07 \pm 0.03$ improves the fit somewhat (F-Test: 3.1×10^{-3}).

5.3.2.3 The CRSFs in the 1998 data

Since the total on-source time of the 1998 data is much less than for the 2000 data, we used only six, broader bins in the 1998 data. We obtained spectra for the rise and fall of the main pulse, the rise and fall of the secondary pulse, and for the two pulse minima (see Fig. 5.13 for the definition of the individual bins). Henceforth, we identify these phase bins with *small* letters.

The CRSF at $52.6^{+1.4}_{-1.9}$ keV is also most significant in the fall (bin f) of the main pulse (F-Test: 8.2×10^{-11}): its depth is $0.8^{+0.3}_{-0.2}$. The line is still significant in the rise of the main pulse (F-Test: 1.6×10^{-4}; $\tau_{\mathrm{C},2} = 0.4^{+0.4}_{-0.1}$). Throughout the

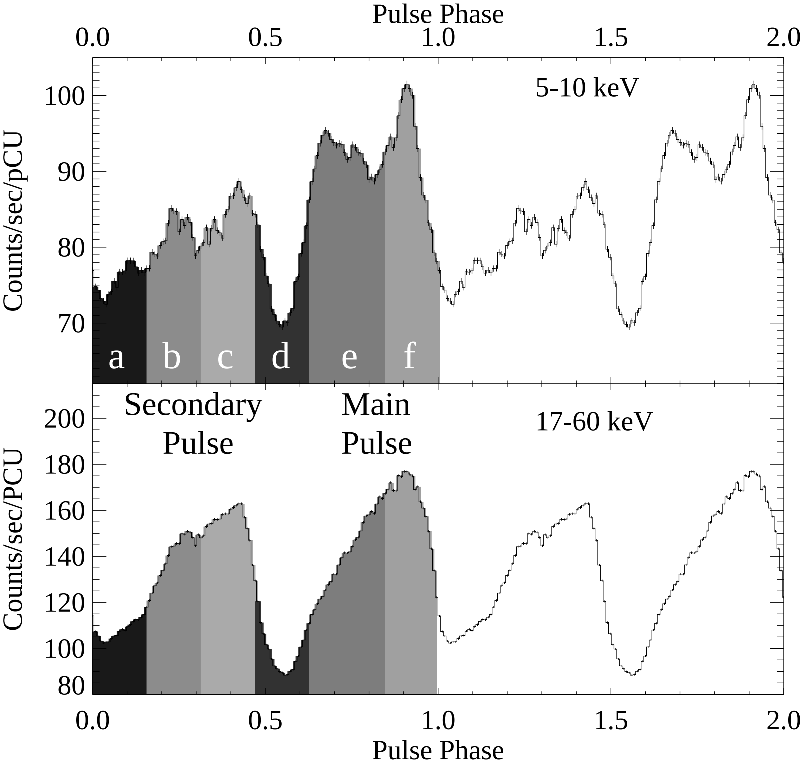

Figure 5.13: FLCs of the 1998 data. The FLCs were generated by converting the photon arrival times to pulse phases using the spin period of the neutron star and then accumulating a pulse profile binned on phase instead of time. Also shown are the definitions of the pulse phase ranges *main pulse fall*, *main pulse rise*, *secondary pulse fall*, *secondary pulse rise*, *pulse minimum 1*, and *pulse minimum 2* for the 1998 data for two different energy bands of the *PCA* (for comparison with the definitions of the 2000 data, see Fig. 5.7). The upper panel shows the folded low energy pulse profile from 5 to 10 keV, while the lower panel shows the high energy pulse profile above 17 keV. For clarity, the folded light-curve is shown *twice*. Note that error-bars *are* shown, but in most cases they are too small to be seen in print.

secondary pulse (bins b, c), the line has a depth of $0.5^{+0.1}_{-0.1}$ similar to the rise of the main pulse and is very significant (F-Test: $< 1.1\times10^{-8}$). In the two pulse minima (bins a, d) the CRSF is also present ($\tau_{C,2} = 0.4^{+0.1}_{-0.1}$), but less significant than in the rise of the main pulse (bin e; F-Test: $< 2 \times 10^{-3}$). Although the line depth seems to vary over the pulse, it is within errors almost consistent with a constant value of $\tau_{\mathrm{C},2} = 0.6$.

After fitting a CRSF at $49.5^{+4.0}_{-3.1}$ keV, there is still a feature present at about 25 keV in the spectrum of the main pulse *rise* (bin e; see Fig. 5.14) – similar to the 2000 data (see Fig. 5.10). Fitting another CRSF at $24.1^{+1.3}_{-0.7}$ keV with a depth of $\tau_{\mathrm{C},1} = 0.08^{+0.03}_{-0.02}$ improves the fit significantly (F-test probability for the CRSF being a chance improvement: 6.3×10^{-5}).

In the fall of the main pulse there is also an indication of the presence of an absorption feature at 25 keV after fitting the $52.7^{+1.6}_{-1.1}$ keV CRSF. Fitting another cyclotron absorption line at $23.6^{+1.0}_{-2.2}$ keV with a depth of $\tau_{\mathrm{C},1} = 0.06^{+0.01}_{-0.02}$ improves the fit with an F-test probability of 2.7×10^{-3}.

However, between the two pulses we found no significant line at 24 keV: in the pulse minimum 1 (bin a) and pulse minimum 2 (bin d), the inclusion of a CRSF at $23.9^{+2.1}_{-1.9}$ keV resulted in no significant improvement; upper limits for the depth of the line are 0.06 (pulse minimum 1) and 0.05 (pulse minimum 2). The same applies for the spectra of the rise and fall of the secondary pulse (bins b and c): the inclusion of a CRSF at 24 keV does *not* improve the fit significantly (F-Test: $> 9.8 \times 10^{-2}$). Note that this does not exclude the presence of a CRSF at 24 keV, it is just not detected: the upper limit for the depth of the CRSF at 24 keV is 0.04 for these phase bins.

5.4 Summary and Discussion

5.4.1 The Pulse Profile

Despite the strong pulse to pulse variations and the overall strong variability of Vela X-1 including flaring activity (see Fig. 5.2, 5.3) and "off-states" (Kreykenbohm et al. 1999; Inoue et al. 1984), the pulse profile at higher *and* lower energies is remarkably stable (compare the pulse profile in Fig. 5.4 and e.g. McClintock et al. 1976). Therefore, the low energy profile is not due to any random short term fluctuations.

Such an evolution of the pulse profile and therefore the spectral shape over the X-ray pulse is typical for accreting X-ray pulsars, however, its interpretation is difficult. While the double pulse at energies above 20 keV can be attributed to the two magnetic poles (Raubenheimer 1990), there is no such straightforward explanation for the low energy pulse profile.

Early explanations of the pulse profile invoked varying photoelectric absorption over the pulse (Nagase et al. 1983). In this picture, for example, the "dip"

Table 5.3: Fit results for some selected phase bins from the 2000 data. All uncertainties quoted in this paper are at the 90% (2.7 σ) confidence level. Note that there is an improvement when using a line at 25 keV also in the secondary pulse but this improvement is very small compared to the improvement in the center of the main pulse (see below). The complete tables for the 1998 and 2000 data are available in Appendix A.

	Main Pulse Fall (F)			Secondary Pulse Fall (C)			Main Pulse Center (E_2)		
	w/o cycl.	1 cycl.	2 cycl.	w/o cycl.	1 cycl.	2 cycl.	w/o cycl.	1 cycl.	2 cycl.
N_H [10^{22}]	$2.4^{+0.5}_{-0.8}$	$2.5^{+0.4}_{-1.8}$	$2.4^{+0.9}_{-0.6}$	$4.2^{+0.5}_{-0.9}$	$4.2^{+0.2}_{-1.3}$	$4.2^{+0.6}_{-0.8}$	$1.9^{+0.5}_{-0.9}$	$1.8^{+0.3}_{-1.3}$	$2.9^{+0.4}_{-1.2}$
Fe [keV]	$6.32^{+0.03}_{-0.07}$	$6.26^{+0.07}_{-0.05}$	$6.34^{+0.04}_{-0.07}$	$6.33^{+0.04}_{-0.06}$	$6.31^{+0.04}_{-0.05}$	$6.33^{+0.04}_{-0.05}$	$6.25^{+0.08}_{-0.05}$	$6.22^{+0.11}_{-0.05}$	$6.31^{+0.05}_{-0.07}$
Fe-σ [keV]	$0.30^{+0.06}_{-0.08}$	$0.33^{+0.06}_{-0.06}$	$0.35^{+0.06}_{-0.06}$	$0.33^{+0.06}_{-0.06}$	$0.33^{+0.06}_{-0.05}$	$0.35^{+0.06}_{-0.06}$	$0.28^{+0.08}_{-0.09}$	$0.31^{+0.08}_{-0.08}$	$0.31^{+0.09}_{-0.08}$
Γ_1	$0.72^{+0.04}_{-0.07}$	$0.61^{+0.06}_{-0.06}$	$0.81^{+0.12}_{-0.08}$	$1.04^{+0.04}_{-0.08}$	$0.98^{+0.06}_{-0.07}$	$1.07^{+0.06}_{-0.08}$	$0.36^{+0.06}_{-0.07}$	$0.29^{+0.07}_{-0.07}$	$0.58^{+0.10}_{-0.11}$
Γ_2	2	2	2	2	2	2	2	2	2
E_F	$6.36^{+0.03}_{-0.03}$	$6.38^{+0.09}_{-0.06}$	$6.37^{+0.08}_{-0.07}$	$5.95^{+0.04}_{-0.03}$	$6.14^{+0.09}_{-0.06}$	$6.04^{+0.08}_{-0.07}$	$6.14^{+0.03}_{-0.03}$	$6.28^{+0.04}_{-0.04}$	$6.02^{+0.17}_{-0.05}$
$E_{\mathrm{C},1}$ [keV]	–	–	$21.1^{+0.7}_{-0.7}$	–	–	$20.1^{+1.3}_{-1.6}$	–	–	$23.3^{+1.3}_{-0.6}$
$\sigma_{\mathrm{C},1}$ [keV]	–	–	$4.1^{+1.6}_{-0.7}$	–	–	$2.8^{+1.4}_{-0.9}$	–	–	$4.9^{+1.9}_{-0.8}$
$\tau_{\mathrm{C},1}$	–	–	$0.13^{+0.05}_{-0.02}$	–	–	$0.06^{+0.03}_{-0.02}$	–	–	$0.15^{+0.07}_{-0.02}$
$E_{\mathrm{C},2}$ [keV]	–	$53.0^{+1.6}_{-1.2}$	$52.8^{+1.9}_{-1.4}$	–	$50.5^{+3.9}_{-2.4}$	$50.6^{+4.9}_{-2.7}$	–	$53.8^{+2.3}_{-1.9}$	$54.5^{+5.0}_{-2.8}$
$\sigma_{\mathrm{C},2}$ [keV]	–	$4.9^{+1.2}_{-0.9}$	$4.7^{+1.5}_{-1.2}$	–	$4.9^{+2.6}_{-2.5}$	$5.4^{+3.4}_{-2.4}$	–	$3.7^{+1.6}_{-1.6}$	$5.3^{+5.1}_{-2.8}$
$\tau_{\mathrm{C},2}$	–	$1.3^{+0.3}_{-0.2}$	$1.1^{+0.3}_{-0.2}$	–	$0.6^{+0.4}_{-0.2}$	$0.5^{+0.2}_{-0.2}$	–	$0.8^{+0.5}_{-0.2}$	$0.5^{+0.3}_{-0.1}$
χ^2(dof)	424 (64)	144 (61)	62 (58)	121 (64)	75 (61)	50 (58)	258 (64)	174 (61)	61 (58)

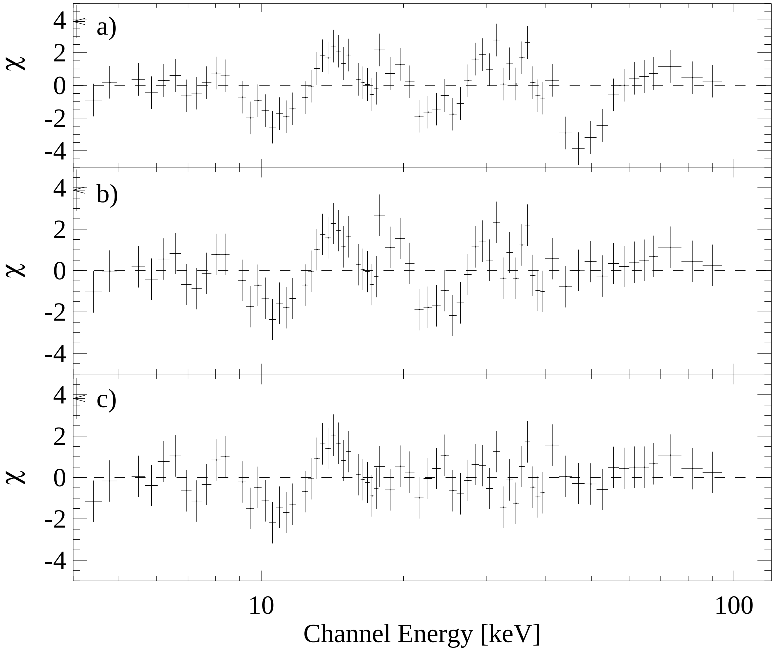

Figure 5.14: Residuals of fits to the spectrum of the *rise* of the main pulse of the 1998 data (bin e). **a** for a model without cyclotron absorption lines, **b** with one line at $53.0^{+1.8}_{-1.4}$ keV, and **c** with two lines at $25.1^{+1.9}_{-1.3}$ keV and $53.0^{+3.8}_{-1.9}$ keV. Note the absorption feature at 25 keV in **b** which is not present or much weaker in the other pulse phases.

at pulse phase ~0.8 is attributed to the accretion column passing through the line of sight. However, there is no such straightforward explanation for the complex profile of the secondary pulse and furthermore, our phase resolved spectra do *not* show an increased absorption in the center of the main pulse (Fig. 5.6). It therefore seems more plausible to attribute the variation of the spectral parameters with pulse phase to the mechanism generating the observed radiation, such as anisotropic propagation of X-rays in the magnetized plasma of the accretion column (Nagel 1981a) or the influence of the magnetic field configuration (Mytrophanov & Tsygan 1978). Due to the uncertainties associated with modeling the accretion column (see Sect. 5.3.1), only the general shape of the pulse profile can be described with these models, and the substructures cannot be explained. A good description of the processes responsible for the complex shape of the pulse profile is thus still missing.

We note, however, that in the strong magnetic field of the accretion column the motion of electrons perpendicular to the magnetic field is constrained, while they move freely parallel to the field lines. As a result, one expects the thermal motion of the electrons to produce a harder spectrum when viewed parallel to the *B*-field than when viewed perpendicular to the field. In a pencil beam geometry, one would then expect the pulse maxima to have a harder spectrum than the minima, similar to what has been seen in Vela X-1.

5.4.2 The existence of the 25 keV line

It is very unlikely that the 25 keV feature results from a calibration problem. Fits to Crab spectra taken close to the 2000 observation have shown that there are no deviations in the relevant area between 20 keV and 30 keV in the *HEXTE* (see Fig. 5.1). Furthermore, we have limited the energy range of the *PCA* to ≤21 keV, so the detection of the line is almost only due to the *HEXTE*. Finally, we note that the line is only visible in one pulse phase of the 1998 data, which should be subject to similar calibration uncertainties as the 2000 data. Since the *HEXTE* has a continuous automatic gain control, the *HEXTE* response is very stable throughout the mission, and thus the calibration is the same for AO1 through AO4.

Our observations indicate that the feature is quite variable with pulse phase. As discussed in the previous sections, the depth of the line varies strongly with pulse phase. In certain phase bins, the lower limit of the depth is 0.20, while in another phase bin its upper limit is 0.09. This variability also makes it highly unlikely that the 25 keV feature is due to a calibration problem as it would then be present in all phase bins. Apart from that, the feature appears at about half the energy of the 50 keV cyclotron line: the lower line is at $22.9^{+2.9}_{-0.9}$ keV, while the second line is at $50.9^{+0.6}_{-0.7}$ keV (2000 data, phase-averaged spectrum). This results in an average coupling factor of 2.15 ± 0.19, in agreement with a factor of 2.0 expected for a first harmonic. We also note that in the main pulse rise (2000 data) where the 25 keV CRSF is deepest, we find a coupling factor of almost *exactly* 2.0. However, we caution that although theoretical models predict a value of 2.0 (Harding & Daugherty 1991, and references therein), recent observations have shown that the fundamental line can be heavily distorted (as in 4U 0115+63; Heindl et al. 1999b; Santangelo et al. 1999) and therefore a coupling factor of exactly 2.0 is not necessarily to be expected.

Furthermore, the 25 keV line varies with time: It was barely visible in the 1998 data and was not seen at all by *BeppoSAX* (Orlandini et al. 1998a). Adding to that, the strong phase variability of the line makes it difficult to detect. Therefore it is not surprising that Orlandini et al. (1998a) and Kreykenbohm et al. (2000) did not detect this line in their phase-averaged spectra. Using phase resolved *Ginga* data, Mihara (1995) also reported a feature at 24 keV in the main pulse while it

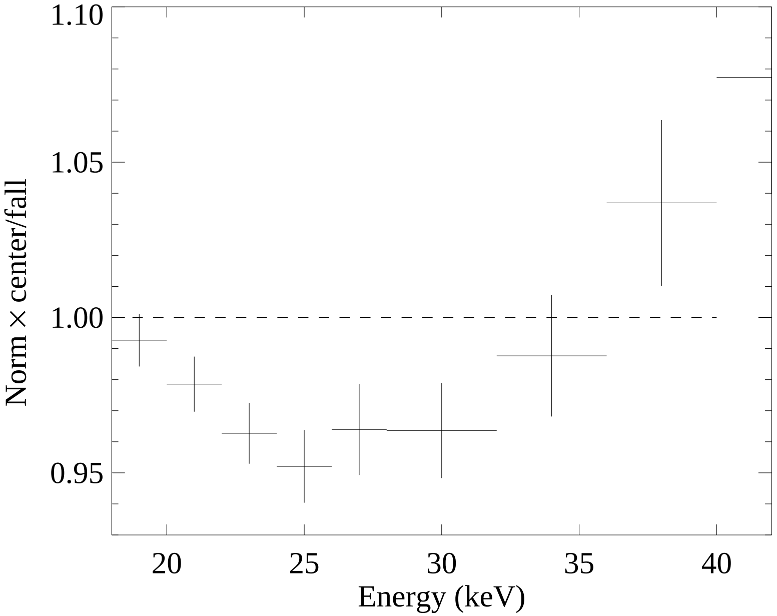

Figure 5.15: Raw *HEXTE* count rate spectrum of the center of the main pulse divided by the raw *HEXTE* count rate spectrum of the fall of the secondary pulse using the 2000 data. Note the clear lack of counts between 20 keV and 30 keV in the spectrum of the center of the main pulse.

was insignificant outside the main pulse.

Finally, to be completely independent of any applied model or response matrices, we divided the raw count rate spectrum of the center of the main pulse by the count rate spectrum of the fall of the secondary pulse. The result is shown in Fig. 5.15: there is a clear dearth of counts between 20 keV and 30 keV, just where we find the 25 keV line with about the same width. This means that there is an absorption line like feature in the raw count rate spectrum of the center of the main pulse – independent of the applied model or the response matrix.

In summary, we have shown that there is an absorption line like feature at 25 keV in some phase bins, while it is shallower or far less significant in other phase bins. The most straightforward interpretation of this feature is that it is the fundamental CRSF, while the 50 keV line is the first harmonic.

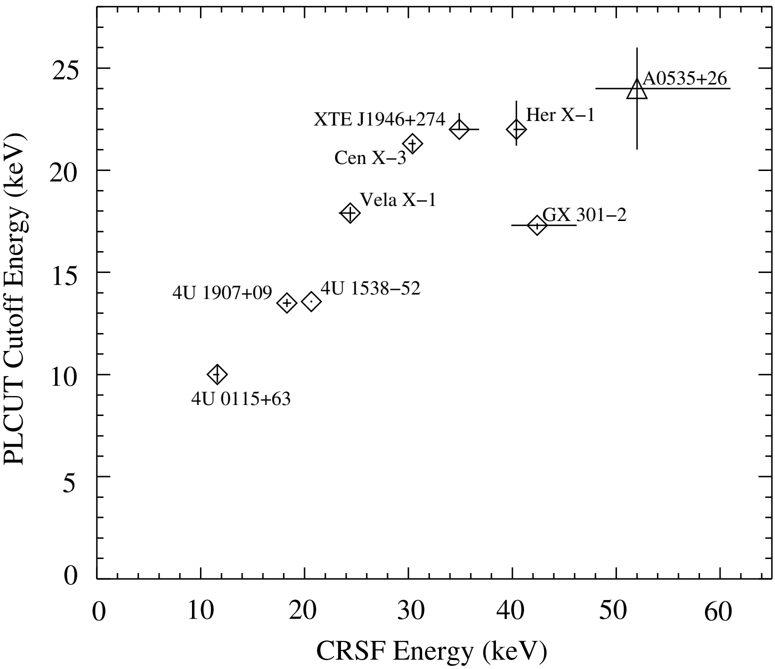

Figure 5.16: Correlation between the centroid energy of the fundamental CRSF and the cutoff energy (when using a power law/high energy cutoff model instead the NPEX model), based on *RXTE* data (with the exception of A 0535+26). See Coburn (2001) for a complete discussion. With a line energy of 25 keV, Vela X-1 fits nicely into the sequence, whereas it would not fit in if the energy of the fundamental line were 50 keV.

5.4.3 CRSFs in accreting pulsars

There are now about a dozen X-ray pulsars for which cyclotron lines have been detected. Most of these sources have been observed with *RXTE*, such that a systematic study of the properties of these sources and their CRSFs starts to become feasible. Although such a study is outside the scope of this paper, we want to point out that our detection of a CRSF at ~25 keV in Vela X-1 is consistent with the general properties of CRSF sources. In their study of CRSFs from *Ginga* and other instruments, Makishima et al. (1999) found a correlation between the energy of the fundamental CRSF and the cutoff energy in the canonical White et al. (1983) X-ray pulsar continuum. Recently, this correlation has been reinvestigated by Coburn (2001) using *RXTE* data from all sources with known CRSFs. Since

RXTE has a broader energy range than previous missions, such a study is able to cover a wider range of CRSF energies. Coburn (2001) finds that most *RXTE* observed pulsars follow the Makishima et al. (1999) correlation up to 35 keV where a roll-over is observed (see Fig. 5.16 and Coburn 2001, for a discussion).

The only exceptions so far are GX 301−2 which shows very high amplitude N_H variations which make the determination of the continuum uncertain, 4U 1626−67 follows the correlation only in certain pulse phases, while X Per has a very different continuum (Coburn et al. 2001) and therefore a comparison with the other sources is difficult if possible at all.

We note that Vela X-1 fits nicely the correlation of Fig. 5.16, provided the fundamental line is at ~25 keV and not at 50 keV.

As we have pointed out in section 5.4.2, the fundamental line in Vela X-1 is weak and only detectable in some specific pulse phases. This is similar to the other three sources where more than one fundamental CRSF has been claimed so far: 4U 0115+63 (Heindl et al. 1999b; Santangelo et al. 1999), A 0535+26 (Kendziorra et al. 1994; Maisack et al. 1997), and 4U 1907+07 (Cusumano et al. 1998). In 4U 0115+63, the fundamental CRSF is quite complex and decidedly non-Gaussian in shape – Heindl et al. (1999b) require two overlapping lines in order to model this line, while the higher 4 harmonics are much more Gaussian in shape. Here, all lines show strong variation with pulse phase, but are almost always present. For A 0535+26, a very prominent line at ~100 keV has been reported by Maisack et al. (1997) using *OSSE*, while a 50 keV feature presented by Kendziorra et al. (1994) from *HEXE* data was quite weak and difficult to model. Finally, Cusumano et al. (1998) find in 4U 1907+09, that the line at 39 keV is again very prominent while its ~19 keV fundamental is weak[2].

Such a complex line shape of the fundamental line is consistent with Monte Carlo simulations of the generation of cyclotron lines in accreting X-ray pulsars (Isenberg et al. 1998b; Araya & Harding 1999; Araya-Góchez & Harding 2000). These simulations show that the shape of the CRSF depends strongly on the assumed geometry, electron temperature, and optical depth of the plasma. It has been pointed out by Araya & Harding (1999), that under certain viewing angles, the fundamental line is not a simple absorption line, but has a very complex shape that includes, for example, “P Cygni” like emission wings. These emission wings are caused by the angular dependence of the scattering cross section, multiple resonant scattering, and by higher order effects such as “photon spawning” (Araya-Góchez & Harding 2000).

---

[2] Recently, a CRSF feature at ~70 keV has also been claimed for Her X-1 (Segreto et al., 2002, in prep.). If this proves to be true, Her X-1 would be the only object with more than one cyclotron line in which the fundamental line is stronger than the upper harmonics.

The feature seen around 20 keV (Figs. 5.10, 5.11, and 5.12) might be such an emission wing. Fitting this feature (where present) with a Gaussian produces a fit comparable to fitting an absorption line. The resulting Gaussians are relatively narrow: $0.7^{+0.6}_{-0.7}$ keV in the fall of the secondary pulse and $1.5^{+0.2}_{-0.4}$ keV in the fall of the main pulse. The Gaussian is broadest in the rise of the main pulse with a width of $3.0^{+1.0}_{-0.7}$ keV. Due to this narrowness we believe that this feature is a wing of a CRSF and not due to improper modeling of the continuum, e.g. due to a Wien bump between 10 keV and 20 keV which would have to be much broader.

Higher order CRSFs tend to be much less affected by these phenomena. When such complicated line profiles are convolved with the moderate energy resolution of todays X-ray detectors, it is possible that such emission wings result in line profiles where the line is almost undetectable or where the line shows the shallow non-Gaussian shape seen in 4U 0115+63. Since the strength of the wings depends on the inclination angle, one could envisage a scenario where the geometry of the accretion column is such that the fundamental is completely filled in except for certain pulse phases, explaining the difficulty of detecting the fundamental CRSF in these systems. Admittedly, these simulations have only begun and the computation of larger grids of simulated and more realistic CRSFs for observational work has only recently become computationally feasible. However, if this speculation were true, it would provide a natural explanation for the scarcity of X-ray pulsars where more than one CRSF is observable.

CHAPTER 6

The variable cyclotron line in GX 301−2

In this chapter, data from the hyper giant X-ray binary Wray 977/ GX 301−2 is analyzed. The data discussed here was obtained with *RXTE* under proposal ID 50066 with me as PI (principal investigator) and Jörn Wilms and Rüdiger Staubert from Tübingen, Richard Rothschild and William Heindl from UCSD, Kim Slavis and Paul Hink from Washington, Peter Hauschildt from the University of Georgia (now in Hamburg) and Peter Kretschmar from the ISDC as CoIs. The source was observed continuously for 200 ksec during the periastron passage and 12 monitoring observations each about 10 ksec long distributed uniformly over the orbit.

This source was known to exhibt one cyclotron line at ~40 keV (Mihara 1995). The detailed pulse phase resolved analysis presented here, showed, however, a previously unknown strong phase dependence of the spectral parameters (energy, depth, and shape) of this line.

Since this chapter is based on the publication Kreykenbohm et al. (2004), it also uses the same structure and also adopts the “we-style” used in that paper.

The remainder of this chapter is structured as follows. In Sect. 6.2 the pulse period and pulse profiles are discussed. Sect. 6.3 discusses the different possible spectral models and detailed fits to phase resolved spectra with special emphasis on the behavior of the cyclotron line. Finally the results are summarized and the discussed in Sect. 6.4.

6.1 Introduction

GX 301−2 (4U 1223−62) is a High Mass X-ray Binary system consisting of a neutron star accreting from the strong stellar wind of the early type B-emission line star Wray 977. Due to difficulties in classifying Wray 977, the system parameters are rather uncertain. In a recent detailed analysis, Kaper et al. (1995) have classified Wray 977 as a B1 Iae+ hypergiant at a distance of 5.3 kpc; we will adopt these values throughout this paper. If this classification is correct, Wray 977 is one of the most luminous and massive stars in our galaxy, with a luminosity of $1.3 \times 10^6\,\mathrm{L}_\odot$ and a mass in excess of $48\,\mathrm{M}_\odot$ (best fit $\sim$75 $\mathrm{M}_\odot$). With one of the highest known wind mass loss rates in the Galaxy ($\dot{M} \sim 10^{-5}\,\mathrm{M}_\odot\,\mathrm{yr}^{-1}$), the very slow wind ($v_\infty = 400\,\mathrm{km\,s}^{-1}$) can easily feed the neutron star with enough material to explain the observed X-ray luminosity of $10^{37}\,\mathrm{erg\,s}^{-1}$. We note that Koh et al. (1997) doubt these extreme parameters for Wray 977 as they are only barely compatible with their analysis, and argue that the earlier distance of 1.8 kpc (Parkes et al. 1980) and a spectral type of B2 Iae is correct, with a correspondingly reduced luminosity of the Be star. Even with these more moderate parameters, the system is unique. Note that the following analysis does not depend on the detailed choice of system parameters.

The neutron star is in an eccentric ($e = 0.462$) orbit with a period of 41.498 ± 0.002 days (Koh et al. 1997; Sato et al. 1986). Due to the violent wind accretion the source is extremely variable – X-ray luminosity changes of a factor of five within one hour being common (Rothschild & Soong 1987). The underlying orbital variability, however, always follows the same pattern (Fig. 6.1): Shortly before periastron passage, the neutron star intercepts the gas stream from Wray 977 (Leahy 1991, 2002), resulting in an extended X-ray flare during which the luminosity increases by a factor of $\sim$25 (see Fig. 6.1 and Pravdo et al. 1995). During periastron passage, the neutron star passes through the dense inner wind of Wray 977, $\sim 0.1\,R_\star$ above the stellar surface (see Pravdo & Ghosh 2001, and Fig. 6.2), and the X-ray activity decreases until it reaches a minimum after the periastron passage. This behavior is probably due to the neutron star being *almost* eclipsed by Wray 977 (Leahy 2002) and an intrinsically lower luminosity compared to the flare. Following this minimum, the X-ray luminosity increases slowly again over the orbit with a possible second maximum near apastron, where the neutron star intercepts the spiral shaped gas stream from Wray 977 a second time (Leahy 2002).

Using the Rossi X-ray Timing Explorer (*RXTE*) we observed GX 301−2 starting in 2000 October (JD 2451829.8 to JD 2451868.3) covering the greater part of the pre-periastron flare and the complete periastron passage in one contiguous $\sim$200 ksec long observation (Fig. 6.3). We used the same procedures as in our

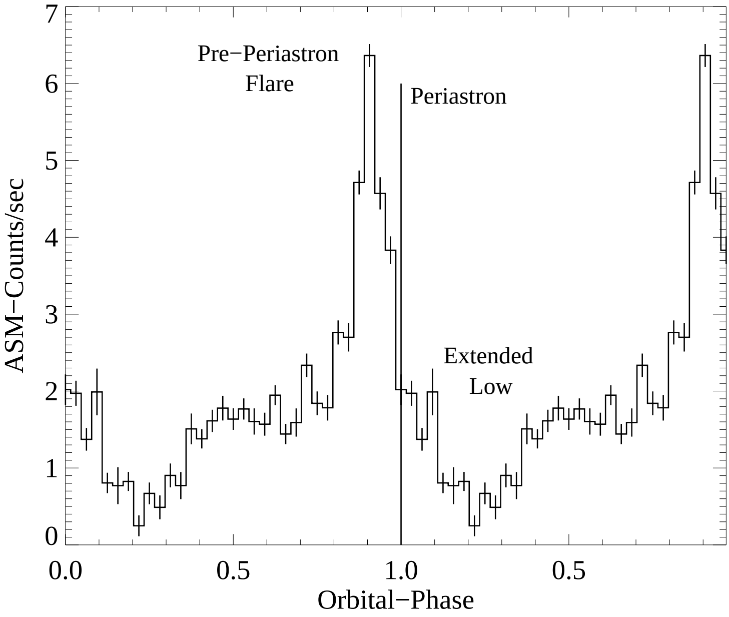

Figure 6.1: Folded light curve (FLC) using all available data (starting in 1996 until mid 2003) on GX 301−2 of the All Sky Monitor on board *RXTE*. The light curve has been folded with the orbital period of 41.498 d (Koh et al. 1997). The periastron passage has been extrapolated based on the ephemeris of Koh et al. (1997). The flare shortly before the periastron passage is very evident. Note the extended low following the periastron passage: it is probably due to the optical companion almost eclipsing the neutron star. For clarity the folded light curve is shown twice.

earlier analysis of *RXTE* data from Vela X-1 (Kreykenbohm et al. 2002a). Due to the improved calibration of the Proportional Counter Array (*PCA*), the systematic uncertainties associated with the *PCA* differ with respect to our earlier work (compare Table 6.1 and Kreykenbohm et al. 2002a, Table 1). All analysis was done using *FTOOLS 5.2* and *XSPEC 11.2.0au* (Arnaud 1996). Phase resolved spectra were produced with a modified version of the *FTOOL fasebin*, which properly accounts for the *HEXTE* dead time (Kreykenbohm et al. 2002a).

The remainder of this paper is structured as follows. In Sect. 6.2 we discuss the pulse period and pulse profiles. Sect. 6.3 discusses the different possible spectral models and detailed fits to phase resolved spectra with special emphasis on the behavior of the cyclotron line. We summarize our results in Sect. 6.4.

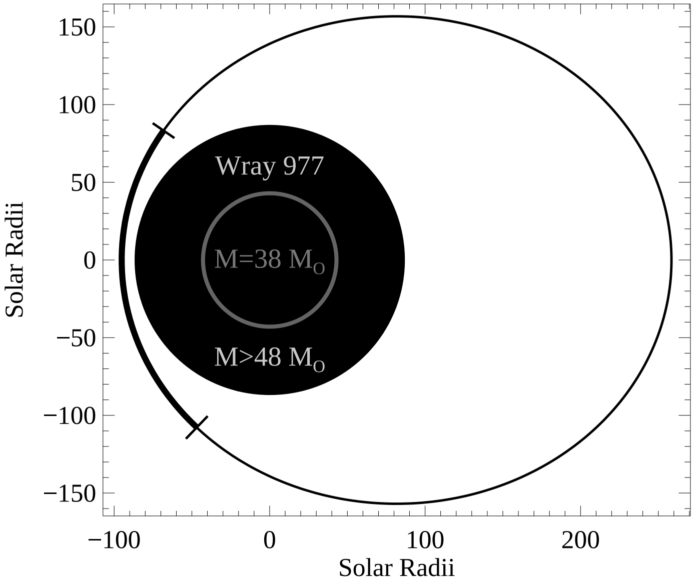

Figure 6.2: Sketch of the system GX 301−2/Wray 977 based on the parameters of Kaper et al. (1995). The neutron star passes Wray 977 at a distance of $\lesssim 0.1R_\star$ during the periastron passage. The time of the observation is marked by dashes and stronger line thickness, covering a significant part of the orbit due to the high velocity of the neutron star during periastron passage. The grey inner circle represents the size of Wray 977 when using the old values of Parkes et al. (1980) which are also used by Koh et al. (1997).

6.2 Pulse profiles

With a pulse period of ~700 sec (Swank et al. 1976), GX 301−2 is one of the slowest pulsars known. Since the first measurement of the period with *Ariel-5*

Table 6.1: Systematic errors applied to the *PCA*-data to account for uncertainties in the *PCA* response matrix. We derived these values by fitting a two power law model simultaneously to a spectrum of a public *RXTE* observation of the Crab. See Wilms et al. (1999) and Kreykenbohm et al. (2002a) for a more detailed discussion of this procedure.

Channels	Energy	Systematics
0– 15	2– 8 keV	1.0%
16– 39	8–18 keV	0.5%
40– 57	18–29 keV	2.0%
58–128	29–120 keV	5.0%

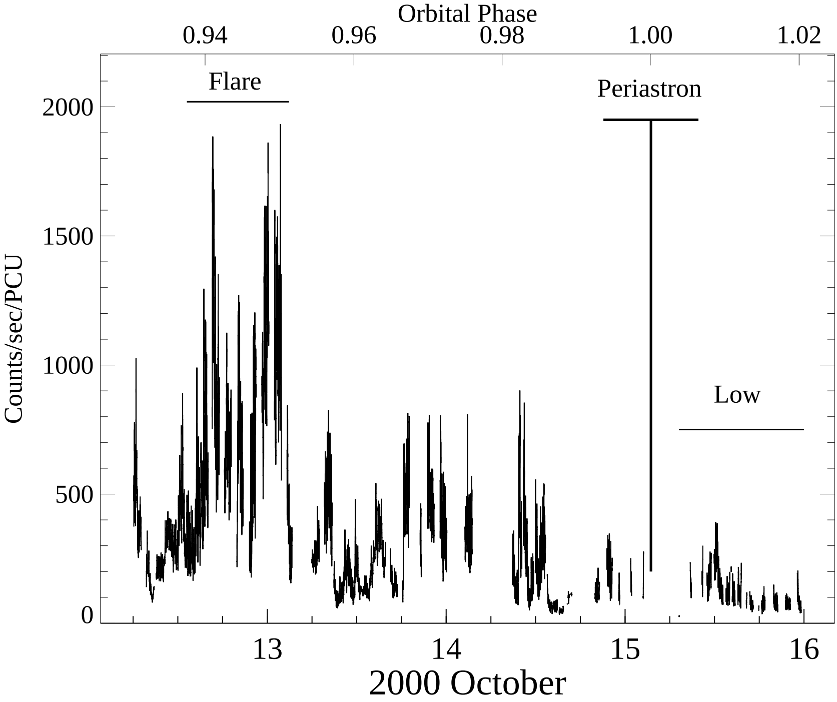

Figure 6.3: X-ray light curve of the periastron passage of GX 301−2 as observed with *RXTE*. The count rate is given in counts/sec per Proportional Counter Unit (PCU). Note the pre-periastron flare, the low following the periastron passage, and the overall variability of the source. The time of the periastron passage has been extrapolated using the ephemeris of Koh et al. (1997); the horizontal bar represents the uncertainty due to the uncertainties of the ephemeris. Our observation covered a significant part of the pre-periastron flare and the periastron passage itself. During the flare, count rates are up to 20 times higher than in the low following the periastron passage.

(White et al. 1976a), it has undergone dramatic variations: the period was stable at ~700 sec until 1984, then the pulsar was spun up between 1985 and 1990 (Koh et al. 1997; Bildsten et al. 1997) to a period of ~675 sec. In 1993, the spin behavior reversed (Pravdo & Ghosh 2001) and the pulsar has since been spinning down almost continously: we determined the pulse period of our observation (JD 2451830.8) to be 684.2 sec (see below). These long lasting spin-up and spin-down trends are in favor of GX 301−2 being a disk accreting system. Similar to other

HMXB systems like Vela X-1, however, the pulse to pulse variations are very strong and the overall short term evolution of the pulse period is best described by a random walk model as is typical for a wind accretor (de Kool & Anzer 1993).

To obtain pulse profiles, the bin (*PCA*) or photon arrival (*HEXTE*) times were first barycentered and then corrected for the orbital motion of GX 301−2 using the ephemeris of Koh et al. (1997). We used epoch folding (Leahy et al. 1983) to determine the pulse period during the periastron passage to be 684.2 ± 0.2 sec, thus confirming that GX 301−2 is continuing its spin down.

We used this period to create energy resolved pulse profiles. This long period, the pulse to pulse variations, and the strong variability of the source, exacerbate the determination of a pulse profile. In our case, GX 301−2 is brighter by a factor of more than ten during the pre-periastron flare compared to the low during the actual periastron passage (Fig. 6.3). We therefore created several sets of energy resolved pulse profiles using *PCA*-data: For the first set we used data taken during the flare only (see Fig. 6.4), while we used data from the low and directly after the pre-periastron flare for the second and third set (Fig. 6.5). In general, the average pulse profile of GX 301−2 is very well defined and similar to that of Vela X-1: it consists of two strong pulses at higher energies evolving into a more complex shape with substructures below 12 keV. As one of the peaks is stronger in all energy bands than the other, we designate this peak as the *main pulse* and the weaker peak as the *secondary pulse*. The secondary peak is strongly energy-dependent: it is very weak (compared to the main pulse) at energies below 10 keV. At higher energies above ~20 keV it is significantly stronger, in fact, almost as strong as the main pulse. At these higher energies, the profile is approximately sinusoidal; however, the main pulse remains stronger throughout the energy band covered here. Also similar to Vela X-1, the long term pulse profile is very stable. There are, however, significant short term variations.

The interpretation of this energy dependence of the pulse profile is not straightforward. Above ~20 keV, the sinusoidal pulse shape can be attributed to contributions from the two magnetic poles of the neutron star. It has been argued that anisotropic propagation of the X-rays in the magnetized plasma of the accretion column (Nagel 1981a) or a complicated configuration of the magnetic field (Mytrophanov & Tsygan 1978) could produce the complex pulse profile at lower energies as well. Alternatively, in analogy to Vela X-1, which also shows a strong energy dependence of the pulse profile (Kreykenbohm et al. 1999, 2002a), increased photoelectric absorption or the accretion column passing through the line of sight can also be invoked to explain the observed profiles (Nagase et al. 1983). Due to the large and Compton thick absorbing column during the flare ($N_\mathrm{H} \sim 10^{23}\,\mathrm{cm}^{-2}$, see below) it seems more likely that this latter explanation holds for GX 301−2 as well. To investigate the causes of the pulse profile variations, a

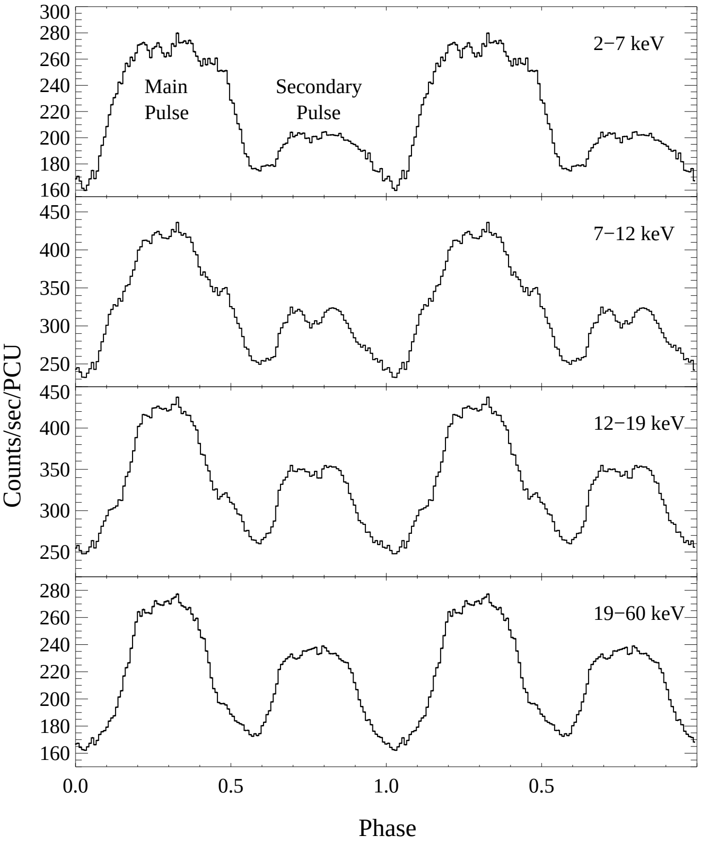

Figure 6.4: Pulse profiles in four energy bands from data taken during the pre-periastron flare (see Fig. 6.3). For clarity the pulse profiles are shown *twice*. Note that the error bars *are* shown, but are too small to be seen in print.

detailed spectroscopic analysis of the pulse phase resolved X-ray spectrum is required.

6.3 Phase resolved spectra

6.3.1 Introduction

As mentioned above, in the standard picture of accreting X-ray pulsars, the strong magnetic field of the neutron star couples to the infalling material and channels it onto the two magnetic poles where two hot spots emerge (Burnard et al. 1991). If the magnetic axis is offset from the rotational axis, the rotation of the neutron star gives rise to pulsations (Davidson & Ostriker 1973). The X-ray spectrum observed from the accretion column and the hot spot has been modeled as exponentially cutoff power law, which is modified by strongly varying photoelectric absorption from the accretion stream or the stellar wind at low energies (White et al. 1980, 1983). Furthermore, an Fe Kα fluorescence line is observed at ~6.4 keV. Swank et al. (1976) also observed an iron edge near 7 keV.

The strong magnetic field ($B \sim 10^{12}\,\mathrm{G}$) at the neutron stars' magnetic poles leads to the formation of cyclotron resonant scattering features (CRSFs, "cyclotron lines"). These lines result from resonant scattering of electrons in Landau levels in the $\sim 10^{12}\,\mathrm{G}$ magnetic field of neutron star (see Coburn et al. 2002; Araya & Harding 1999; Mészáros & Nagel 1985, and references therein). The energy of the feature is nominally given by

$$E_\mathrm{C} = 11.6\,\mathrm{keV} \times \frac{1}{1+z} \times \frac{B}{10^{12}\,\mathrm{G}} \tag{6.1}$$

where E_C is the centroid energy of the CRSF, z is the gravitational redshift at the scattering site (if the scattering occurs at the surface of the neutron star, $z \sim 0.3$, depending on the equation of state), and B the magnetic field strength. The energy of the fundamental CRSF thus gives a direct measure of the magnetic field strength in the line forming region.

Since the physical conditions are expected to vary over the emission region, the X-ray spectrum is expected to change with the viewing angle, and therefore with pulse phase. This change is especially important when analyzing CRSFs since their shape depends strongly on the viewing angle (Araya-Góchez & Harding 2000; Araya & Harding 1999; Isenberg et al. 1998a), thus making a spectrum averaged over the whole pulse period difficult to interpret. We therefore analyzed the data from GX 301−2 using six phase intervals as defined in Fig. 6.5: the rise and fall of the main pulse, the rise and fall of the secondary pulse, and the two pulse minima. These intervals were chosen to give a good coverage of the pulse with a similar signal to noise ratio.

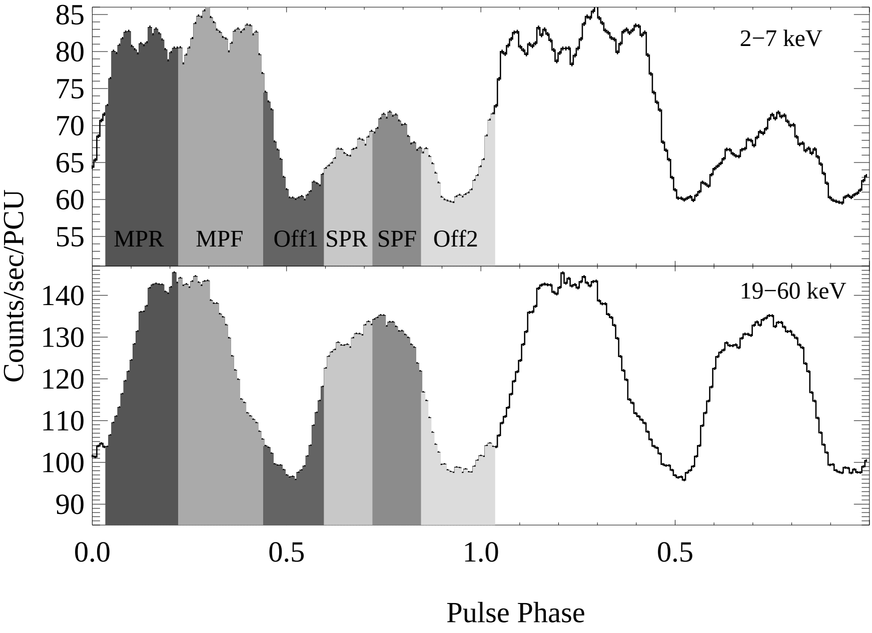

Figure 6.5: Definition of the six phase bins used for phase resolved spectroscopy using pulse profiles of data taken *after* the pre-periastron flare (see Fig. 6.3). Different shadings show the six phase bins in use: rise and fall of the main pulse (MPR and MPF), rise and fall of the secondary pulse (SPR and SPF), and the two pulse minima (OFF1 and OFF2).

6.3.2 The spectral model

The lack of theoretical models of high enough quality for comparison with observational data forces the use of empirical spectral models for the characterization of the observed continuum (Kreykenbohm et al. 1999). Here, we describe the continuum produced in the accretion column of the neutron star, $I_{\mathrm{NS}(E)}$, by a power law with photon index Γ which is cutoff by the Fermi-Dirac cutoff (Tanaka 1986),

$$I_{\mathrm{NS(E)}}(E) = A_{\mathrm{PL}} \frac{E^{-\Gamma}}{\exp\left((E - E_{\mathrm{Cut}})/E_{\mathrm{F}}\right) + 1} \tag{6.2}$$

where A_{PL} is a normalization constant, and where E_{Cut} and E_{F} are called the cutoff and folding energy of the Fermi-Dirac cutoff. This continuum shape is then modified by a CRSF modeled as an absorption line with a Gaussian depth profile

(Coburn et al. 2002, Eqs. 6 and 7),

$$d_{\mathrm{GABS}}(E) = d_{\mathrm{C}} \times \exp\left(-\frac{1}{2}\left(\frac{E - E_{\mathrm{C}}}{\sigma_{\mathrm{C}}}\right)^2\right) \tag{6.3}$$

where E_{C} is the energy, σ_{C} the width, and d_{C} the depth of the CRSF. The shape of this absorption line is simpler than the pseudo-Lorentzian line shape (as used by the *XSPEC* model CYCLABS and in earlier works; see, e.g., Makishima & Ohashi 1990) and gives equally good fits. The overall X-ray spectrum emitted by the neutron star is then given by

$$I_{\mathrm{NS}}(E) = I_{\mathrm{cont}}(E)\exp(-\tau_{\mathrm{GABS}}(E)) \tag{6.4}$$

Due to the strong stellar wind of Wray 977, however, the observed X-ray spectrum of GX 301−2 is strongly modified by photoelectric absorption, especially during times when the neutron star is close to Wray 977, such as in our observation. As the material enshrouding the neutron star is most likely clumpy, we expect (part of) the neutron star's X-rays to be strongly absorbed close to the neutron star ($N_{\mathrm{H},2}$ in Eq. 6.5). Furthermore, all X-rays emerging from this zone will also be subject to photoelectric absorption in the overall stellar wind of Wray 977 ($N_{\mathrm{H},1}$ in Eq. 6.5). A model describing such a physical situation is the *absorbed partial covering model*, which has the form

$$I_{\mathrm{obs}}(E) = \mathrm{e}^{-\sigma_{\mathrm{bf}} N_{\mathrm{H},1}}\left(1 + c\mathrm{e}^{-\sigma_{\mathrm{bf}} N_{\mathrm{H},2}}\right) I_{\mathrm{NS}}(E) + I_{\mathrm{Fe}}(E) \tag{6.5}$$

where σ_{bf} is the bound free absorption cross section per Hydrogen atom (Wilms et al. 2000), $N_{\mathrm{H},1}$ and $N_{\mathrm{H},2}$ are the column densities of the two components, and c is the covering fraction of the absorber responsible for $N_{\mathrm{H},2}$. The possibility of a fluorescent Fe Kα line is accounted for by a Gaussian emission line, I_{Fe}.

A second possible scenario takes into account that during periastron passage the neutron star is extremely close to the surface of Wray 977. A large fraction of the neutron star's X-rays are thus intercepted by Wray 977 where they are backscattered by Thomson scattering or absorbed. This situation is analogous to the Compton reflection hump observed in active galactic nuclei (Lightman & White 1988). In principle, the X-rays backscattered from within the atmosphere of Wray 977 could be responsible for a significant part of the total observed X-ray flux. A model describing this physical situation has the form

$$I_{\mathrm{obs}}(E) = \mathrm{e}^{-\sigma_{\mathrm{bf}} N_{\mathrm{H}}}\left(I_{\mathrm{NS}}(E) + \mathrm{R}_{I_{\mathrm{NS}}}(E;\Omega/2\pi) + I_{\mathrm{Fe}}(E)\right) \tag{6.6}$$

where all symbols are as described above and where $\mathrm{R}_I(E;\Omega/2\pi)$ describes the spectrum resulting from Compton reflecting X-rays with spectral shape $I(E)$ off gas with covering factor $\Omega/2\pi$ (Magdziarz & Zdziarski 1995). Again, this spectrum is photoabsorbed in the strong stellar wind of Wray 977.

We note that these two pictures are not exclusive: the accretion stream might well be patchy close to the neutron star, and the X-ray spectrum emerging from the accretion stream would then be reprocessed in the atmosphere of Wray 977. Detailed spectral fitting shows, however, that applying either of the above models already results in $\chi^2_{\text{red}} \sim 1$. Combining the partial covering model and the reflection model is therefore not necessary. With the available spectral data alone, it is not possible to test which of the two continuum models is the more realistic one – the absorption column of the partial covering model is so high that it mimics the features of the soft end of the reflection spectrum (note that the shape of the reflection spectrum below 10 keV is essentially identical to the shape of the incident continuum, absorbed by a column equivalent to one Thomson optical depth). Since the major aim of this work is the study of the cyclotron line, which is not affected by the details of the modeling of the continuum below 10 keV, we will concentrate our discussion in the remainder of this paper on the behavior of the source as reflected in the fits of the absorbed partial covering model (Table 6.3). The corresponding fit parameters from the reflection model are listed in Table 6.4.

To allow the comparison of the spectral shape used here with other parameterizations of the continuum, we also modeled the data with several other standard pulsar continua (with and without a CRSF), especially using the high energy cutoff (White et al. 1983, see Table 6.2). Residuals for these continua for the rise of the secondary pulse are shown in Fig. 6.6. In this pulse region (phase region SPR, see Fig.6.5) the CRSF is very prominent such that the data are especially suited to illustrate the difficulties of the standard spectral models.

a: Negative Positive Exponential (NPEX, Mihara 1995; Mihara et al. 1998), with strong residuals especially below 10 keV. Despite the inclusion of a CRSF at 32 keV, significant residuals remain above 40 keV ($\chi^2_{\text{red}} = 17.2$ before, $\chi^2_{\text{red}} = 10.7$ after including the line). **b**: power law with a Fermi-Dirac cutoff (FDC, Tanaka 1986, $\chi^2_{\text{red}} = 9.6$ without a CRSF (not shown), 5.5 with CRSF at ~35 keV) **c**: power law with high energy cutoff after White et al. (1983, HEC; $\chi^2_{\text{red}} = 25.4$), exhibiting a very prominent and spurious feature. Because of this spectral artifact, this model should not be used for cyclotron line searches (Kretschmar et al. 1997; Kreykenbohm et al. 1999); for comparison with earlier observations the best fit values are shown in Table 6.2. **d**: the Smoothed High Energy Cutoff (SHEC), the HEC model smoothed by including a Gaussian absorption line (GABS) at the cutoff energy (Coburn et al. 2002), describes the data very well after applying a CRSF at 35 keV: $\chi^2_{\text{red}} = 2.6$ before including a CRSF (not shown), and 1.7 after the inclusion; see also Table 6.2, **e**: a standard partial covering model (PC, essentially this is Eq. 6.5, setting $N_{\text{H},1} = 0$) still shows significant deviations below 8 keV:

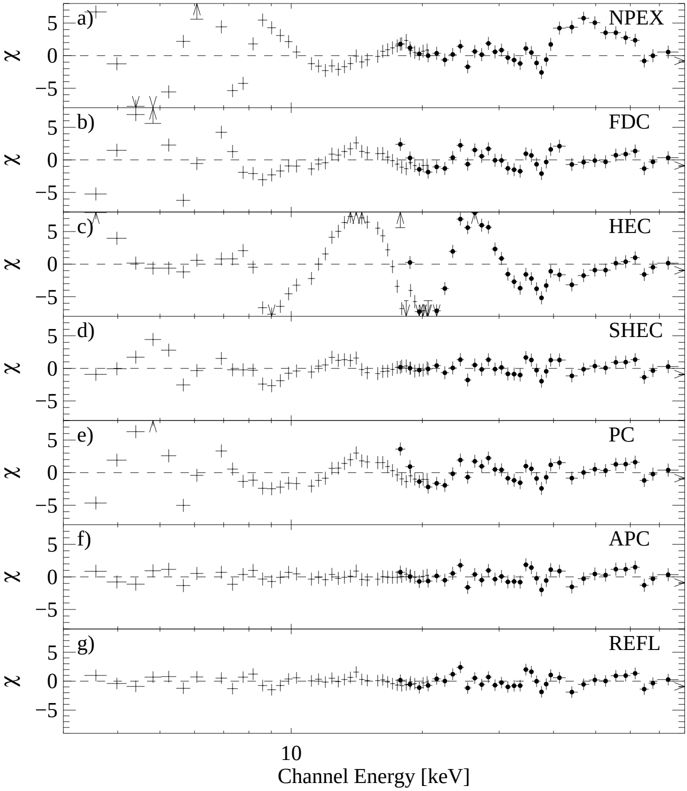

Figure 6.6: Residuals of fits of conventional neutron star continuum models to phase bin SPR (see Fig. 6.5). Unless otherwise noted, the residuals shown include photoelectric absorption, an additive Fe Kα line, and the CRSF. For discussion, see text.

$\chi^2_{\rm red} = 11.0$ without a CRSF (not shown), $\chi^2_{\rm red} = 5.4$ after including a 33 keV CRSF, which are remedied by using the **f**: Absorbed Partial Covering (APC) model of Eq. 6.5: $\chi^2_{\rm red} = 4.1$ without a CRSF (not shown), and $\chi^2_{\rm red} = 0.8$ after the inclusion of a CRSF at 34 keV. **g**: Reflection Model of Eq. 6.6. Residuals are comparable to those of the APC; therefore, we use the APC model along with this reflection model to analyze the data.

Table 6.2: Parameters for spectral modeling of data from phase bin SPR (for definition, see Fig. 6.5) with a power law and a high energy cutoff (White et al. 1983, HEC) or a smoothed version of this cutoff (Coburn et al. 2002, SHEC) with and without the inclusion of a CRSF. At lower energies all three models are modified by photoelectric absorption.

Parameter	HEC	SHEC	SHEC + CRSF
$N_\mathrm{H}[10^{22}]$	$26.4^{+0.3}_{-0.2}$	$17.2^{+0.8}_{-0.8}$	$16.9^{+0.9}_{-0.9}$
Γ	$0.14^{+0.01}_{-0.01}$	$-0.32^{+0.04}_{-0.04}$	$-0.34^{+0.04}_{-0.05}$
E_Cut [keV]	$19.86^{+0.02}_{-0.03}$	$18.43^{+0.14}_{-0.14}$	$18.22^{+0.34}_{-0.18}$
E_F [keV]	$6.08^{+0.04}_{-0.02}$	$5.29^{+0.05}_{-0.05}$	$5.44^{+0.09}_{-0.08}$
Fe [keV]	$6.50^{+0.03}_{-0.02}$	$6.47^{+0.01}_{-0.01}$	$6.46^{+0.01}_{-0.01}$
Fe-σ [keV]	$0.25^{+0.02}_{-0.03}$	$0.38^{+0.02}_{-0.02}$	$0.38^{+0.02}_{-0.02}$
τ_C	–	–	$0.14^{+0.05}_{-0.03}$
E_C [keV]	–	–	$34.9^{+1.7}_{-1.3}$
σ_C	–	–	$3.4^{+2.8}_{-1.5}$
χ^2 (dof)	1620.4 (64)	157.1 (61)	99.9 (58)

6.3.3 Spectral fits

Since the source is extremely variable, we accumulated phase resolved spectra not only for the whole data set, but separately also for the pre-periastron flare and the low following the flare. With a total usable exposure time of 176 ks for *PCA* and 89 ks live time for *HEXTE* the phase resolved spectra from the whole data set provide excellent statistical quality (note that the exposure time in *HEXTE* is typically lower by ~40% due to the dead time of the instrument; during our observation, the orbit of *RXTE* was very close to the South Atlantic Anomaly thus giving rise to an increased particle background resulting in a deadtime of about ~50% in the *HEXTE*). In the following paragraphs, we will use this complete dataset for our analysis. See Tables 6.3 and 6.4 for a list of the spectral parameters.

The total usable exposure time during the flare is ~25 ksec for *PCA* and ~12 ksec for *HEXTE*. Even though this is much shorter than that of the whole observation, the flare spectra dominate over the rest of the observation due to the much higher flux during the flare. Since the low luminosity post periastron data have a much lower statistical quality, the uncertainties of all parameters from this time are fairly large and the CRSF could not be detected in any phase region with high significance.

Since the data from the flare are very similar to the data from the complete

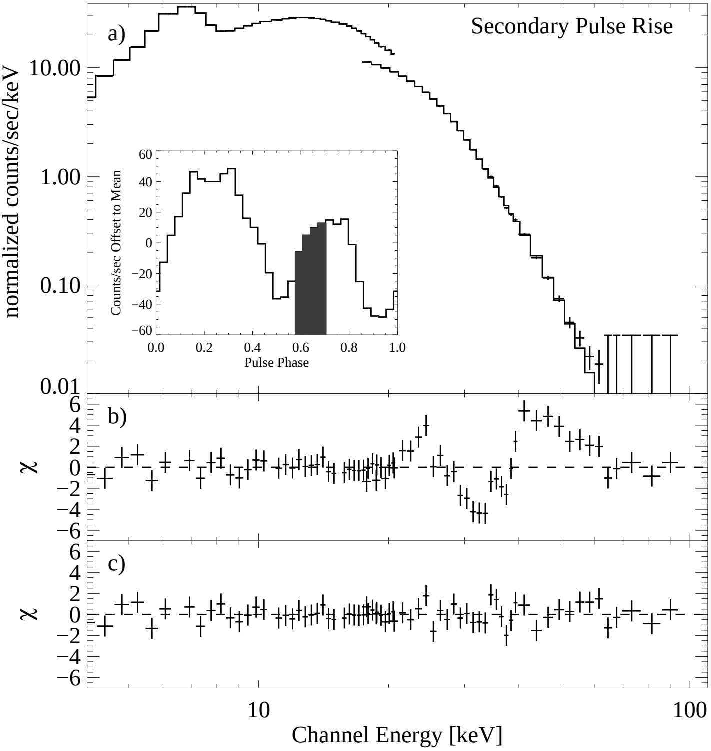

Figure 6.7: **a**: Data and folded model of the rise of the secondary pulse. The model is an absorbed partial covering model (for discussion, see text). **b**: Residuals for the model without a CRSF and **c**: with a CRSF at $34.2^{+1.1}_{-0.9}$ keV. The inset shows the pulse profile of GX 301−2 in the energy range from 5 keV to 20 keV. The marked region is the phase bin under discussion – the rise of the secondary pulse (see also Fig. 6.5).

set and the data from the low have a low statistical quality, we only discuss the spectral parameters for the complete data set (unless mentioned otherwise).

6.3.3.1 The X-ray spectrum below 10 keV

As is expected from the physical picture outlined in Sect. 6.3.2, the spectral parameters identified with the stellar wind – $N_{\mathrm{H},1}$, $N_{\mathrm{H},2}$, and the parameters of the Fe Kα line – do not depend significantly on the pulse phase as they originate very far away from the neutron star compared to the accretion column where the X-rays and the pulse forms.

The high column density of the stellar wind as measured during the whole observation, $N_{\mathrm{H},1} \sim 2 \times 10^{23}\,\mathrm{cm}^{-2}$ indicates how deep the neutron star is embedded in the wind. With a column density of as high as $2.3 \times 10^{24}\,\mathrm{cm}^{-2}$, the second component of the partial covering model is close to being Compton thick. As explained above, this large value is responsible for our inability to differentiate between the partial covering model and the Compton reflection model.

In the low following the pre-periastron flare, the absorbing columns are measured to be even higher. The column density for the "weakly" absorbed component, $N_{\mathrm{H},1}$, varies between 3.5×10^{23} and $4.5 \times 10^{23}\,\mathrm{cm}^{-2}$ and is thus twice as large as during the flare, and also the column density $N_{\mathrm{H},2}$ is increased: it varies between $4 \times 10^{24}\,\mathrm{cm}^{-2}$ to over $10^{25}\,\mathrm{cm}^{-2}$. However, the observed count rate is not only due to the strong photoelectric absorption but also due to an intrinsically lower source luminosity: while the *unabsorbed* flux during the flare is about $1 \times 10^{-8}\,\mathrm{erg\,s}^{-1}$, the *absorbed* flux, however, is $\sim 4.9 \times 10^{-9}\,\mathrm{erg\,s}^{-1}$. During the low the unabsorbed flux is lower by a factor of three ($\sim 3.5 \times 10^{-9}\,\mathrm{erg\,s}^{-1}$) and the absorbed flux by a factor of more then six ($\sim 7 \times 10^{-10}\,\mathrm{ergs\ s}^{-1}$).

The high column density of the wind is also responsible for the strong Fe Kα fluorescence line. The line energy of $6.48^{+0.03}_{-0.02}\,keV$, corresponding to an ionization level from Fe V to Fe IX, implies that the iron, and thus probably all circumstellar material, is mildly ionized. Also the width of the line, $\sigma_{\mathrm{Fe}} = 0.33^{+0.02}_{-0.02}\,keV$, is close to the energy resolution of the *PCA*, the very small uncertainties indicate that the line width is indeed measured.

6.3.3.2 The pulsar continuum and the cyclotron line

Pulse phase spectroscopy allows us to study the variation of the pulsar emission over the X-ray pulse. Our data analysis shows that the photon index Γ is almost constant over the pulse and only varies between -0.2 ± 0.1 and 0.1 ± 0.1. Note that the spectrum is slightly but systematically softer in all phase bins during the pre-periastron flare. The parameters of the cutoff also do not vary over the pulse: The folding energy E_{F} is only variable between 5.0 keV and 5.9 keV, while the cutoff energy E_{Cut} is consistent with a constant value of 15.5 keV except for the rise of the main pulse where it is marginally lower ($E_{\mathrm{Cut}} = 12.9^{+1.8}_{-1.6}\,keV$).

This continuum model alone, however, does not result in an acceptable fit in any of the phase bins (see e.g., Fig. 6.7b). In all phase bins a large absorption line like structure is present between 30 keV and 40 keV (see Fig. 6.9). After the inclusion of a CRSF, the fits are acceptable in all phase bins with $\chi^2_{\mathrm{red}} \sim 1.0$ (see Tables 6.3 and 6.4). The improvement is extremely significant: according to the F-Test (Bevington & Robinson 1992)[1] the probability of a chance improvement is 2.5×10^{-11} in the fall of the secondary pulse (the bin with the smallest improvement). We remark that the CRSF is found at almost the same energy and the same width (within uncertainties), but with a higher $\chi^2_{\text{red}}$when using the SHEC model applied in earlier publications (compare Tables 6.2 and 6.3).

---

[1] Note that in principle the F-Test is known to be problematic when used for the significance of a

Contrary to the continuum, the depth and the position of the CRSF are strongly variable with pulse phase (see Tables 6.3, 6.4, and Fig 6.10). This behavior is fairly typical of most CRSF sources (e.g. Vela X-1 or Her X-1). We find that the line is deepest in the minimum between the main pulse and the secondary pulse (phase bin OFF1) with $\tau_\text{C} = 0.32^{+0.19}_{-0.13}$, and it is also of comparable depth in the adjacent phase bins, the fall of the main pulse (MPF, $\tau_\text{C} = 0.29^{+0.08}_{-0.06}$) and the rise of the secondary pulse (SPR, $\tau_\text{C} = 0.23^{+0.04}_{-0.03}$). While the depth of the CRSF in these three phase bins has a lower limit of 0.20, the CRSF is significantly less deep in the other three phase bins. At the same time, the position of the CRSF changes from $E_\text{C} = 30.1^{+0.8}_{-0.7}\,keV$ in the fall of the secondary pulse and $E_\text{C} = 31.0^{+0.6}_{-0.5}$ keV at the rise of the main pulse to significantly higher energies in the fall of the main pulse and the pulse minimum, where it becomes as high as $\sim 37.9\,keV$ (Fig. 6.10). Assuming a canonical mass of $1.4\,\text{M}_\odot$ and a radius of 10 km for the neutron star, the typical gravitational redshift amounts to ~29% at the surface of the neutron star, such that the measured values imply a magnetic field between $B = 3.4 \times 10^{12}$ G and $B = 4.2 \times 10^{12}$ G for GX 301−2.

This change of the CRSF energy is correlated with its depth: the line is deepest in the phase bins where the CRSF is at the highest energies (correlation coefficient > 0.97). Note that this behavior is not due to the intrinsically lower signal during the interpulse: during the fall and the rise of the main pulse, where the data are of comparable statistical quality (and the source has a similar flux), we find a significant difference of the spectral parameters. We finally note that the line width of the CRSF σ_C is always in the range from 3 keV to 7 keV, typical for CRSFs at these energies.

As we illustrate in Fig. 6.9, in addition to the changes of the depth and position of the CRSF, there are indications for a change in the shape of the feature itself. After fitting the CRSF in the rise of the main pulse some residuals remain (see Fig. 6.8), indicating that the CRSF has a non-Gaussian line shape. Furthermore, the remaining residuals at ~50 keV could indicate the presence of an emission wing. The existence of such emission wings and overall variations of the line profile over the pulse have been predicted by the numerical simulations of Araya & Harding (1999).

---

line (non-) detection (Protassov et al. 2002), even if systematic uncertainties are not an issue, however, the extremely low false alarm probabilities make the detection of the line stable against even crude mistakes in the computation of the significance.

Table 6.3: Fitted parameters from pulse phase spectroscopy for using the whole 200 ksec long observation of the periastron passage and the pre-periastron flare (see Fig. 6.3). The model is the absorbed partial covering model described in Sect. 6.3.2 by Eq. 6.5 with and without the inclusion of CRSF. Note that the inclusion of the CRSF between 30 keV and 40 keV in this data set improves the fits in all phase bins including in the pulse minima, where CRSFs are often either not present or insignificant (see e.g., Kreykenbohm et al. 2002a). All uncertainties quoted in this table and elsewhere in this paper are 90% confidence. dof are the degrees of freedom. The flux is absorbed flux given in erg s^{-1} in the 2–10 keV band.

Phase	$N_{\mathrm{H},1}[10^{22}]$	$N_{\mathrm{H},2}[10^{22}]$	Γ	E_{Cut} [keV]	E_{F} [keV]	E_{Fe} [keV]	σ_{Fe} [keV]
MPR	$22.7^{+2.3}_{-2.3}$	$268.5^{+8.9}_{-10.0}$	$-0.12^{+0.09}_{-0.11}$	$9.9^{+0.7}_{-1.3}$	$5.78^{+0.58}_{-0.58}$	$6.48^{+0.02}_{-0.02}$	$0.31^{+0.03}_{-0.03}$
MPR+C	$22.2^{+1.3}_{-1.2}$	$249.0^{+14.8}_{-20.7}$	$-0.05^{+0.13}_{-0.12}$	$12.8^{+1.7}_{-2.0}$	$5.88^{+0.08}_{-0.08}$	$6.48^{+0.02}_{-0.02}$	$0.33^{+0.03}_{-0.03}$
MPF	$21.8^{+1.6}_{-0.5}$	$265.1^{+16.1}_{-16.7}$	$0.07^{+0.11}_{-0.04}$	$15.8^{+0.7}_{-0.2}$	$5.44^{+0.08}_{-0.04}$	$6.48^{+0.02}_{-0.02}$	$0.33^{+0.03}_{-0.03}$
MPF+C	$22.5^{+1.3}_{-1.1}$	$242.8^{+17.7}_{-20.1}$	$0.06^{+0.10}_{-0.09}$	$15.0^{+1.2}_{-1.1}$	$5.93^{+0.15}_{-0.11}$	$6.48^{+0.02}_{-0.02}$	$0.34^{+0.03}_{-0.03}$
OFF1	$22.6^{+0.6}_{-0.5}$	$249.6^{+15.5}_{-14.9}$	$0.03^{+0.10}_{-0.06}$	$16.1^{+0.5}_{-0.5}$	$5.09^{+0.06}_{-0.05}$	$6.49^{+0.02}_{-0.02}$	$0.34^{+0.03}_{-0.03}$
OFF1+C	$22.6^{+1.3}_{-1.3}$	$230.7^{+14.7}_{-13.3}$	$-0.18^{+0.26}_{-0.16}$	$16.3^{+1.9}_{-1.6}$	$5.52^{+0.24}_{-0.16}$	$6.50^{+0.02}_{-0.02}$	$0.34^{+0.03}_{-0.03}$
SPR	$20.5^{+1.0}_{-1.0}$	$218.8^{+14.3}_{-14.6}$	$-0.19^{+0.09}_{-0.08}$	$16.2^{+0.4}_{-0.4}$	$4.97^{+0.06}_{-0.05}$	$6.49^{+0.02}_{-0.02}$	$0.33^{+0.03}_{-0.03}$
SPR+C	$20.8^{+1.2}_{-1.4}$	$211.0^{+17.5}_{-18.9}$	$-0.21^{+0.10}_{-0.11}$	$15.2^{+1.1}_{-1.1}$	$5.35^{+0.11}_{-0.10}$	$6.49^{+0.02}_{-0.02}$	$0.33^{+0.03}_{-0.03}$
SPF	$20.0^{+0.8}_{-0.6}$	$234.0^{+12.7}_{-13.3}$	$-0.34^{+0.02}_{-0.00}$	$12.8^{+0.8}_{-0.7}$	$5.29^{+0.08}_{-0.06}$	$6.48^{+0.02}_{-0.02}$	$0.32^{+0.03}_{-0.03}$
SPF+C	$20.2^{+1.4}_{-1.2}$	$204.0^{+18.7}_{-21.6}$	$-0.25^{+0.11}_{-0.11}$	$15.0^{+1.2}_{-1.1}$	$5.39^{+0.07}_{-0.07}$	$6.49^{+0.01}_{-0.01}$	$0.33^{+0.03}_{-0.03}$
OFF2	$21.7^{+0.8}_{-0.3}$	$267.0^{+11.8}_{-12.3}$	$-0.11^{+0.13}_{-0.06}$	$13.3^{+1.1}_{-0.4}$	$5.12^{+0.09}_{-0.05}$	$6.50^{+0.02}_{-0.01}$	$0.33^{+0.03}_{-0.02}$
OFF2+C	$22.7^{+1.4}_{-1.3}$	$244.6^{+16.5}_{-19.8}$	$-0.03^{+0.11}_{-0.10}$	$14.1^{+1.9}_{-0.8}$	$5.30^{+0.08}_{-0.07}$	$6.50^{+0.02}_{-0.01}$	$0.34^{+0.03}_{-0.03}$

Phase	τ_{C}	E_{C} [keV]	σ_{C}	χ	(dof)	χ^2_{red}	Flux
MPR	–	–	–	255.0	(62)	4.11	1.87×10^{-9}
MPR+C	$0.10^{+0.02}_{-0.01}$	$31.0^{+0.6}_{-0.6}$	$3.5^{+1.3}_{-1.0}$	73.9	(59)	1.25	
MPF	–	–	–	364.2	(62)	5.87	1.93×10^{-9}
MPF+C	$0.29^{+0.08}_{-0.05}$	$38.0^{+1.3}_{-1.1}$	$6.1^{+1.7}_{-1.1}$	50.4	(59)	0.85	
OFF1	–	–	–	140.6	(62)	2.27	1.37×10^{-9}
OFF1+C	$0.33^{+0.25}_{-0.10}$	$37.3^{+2.5}_{-2.3}$	$7.6^{+2.0}_{-2.4}$	42.4	(59)	0.72	
SPR	–	–	–	251.7	(62)	4.06	1.47×10^{-9}
SPR+C	$0.25^{+0.07}_{-0.04}$	$35.2^{+1.3}_{-1.1}$	$5.1^{+1.6}_{-1.1}$	56.0	(59)	0.95	
SPF	–	–	–	176.8	(62)	2.85	1.52×10^{-9}
SPF+C	$0.10^{+0.02}_{-0.02}$	$30.0^{+0.8}_{-0.6}$	$3.0^{+1.2}_{-1.1}$	77.8	(59)	1.32	
OFF2	–	–	–	170.2	(62)	2.74	1.31×10^{-9}
OFF2+C	$0.14^{+0.01}_{-0.02}$	$31.9^{+1.2}_{-1.0}$	$4.0^{+1.7}_{-1.2}$	51.0	(59)	0.86	

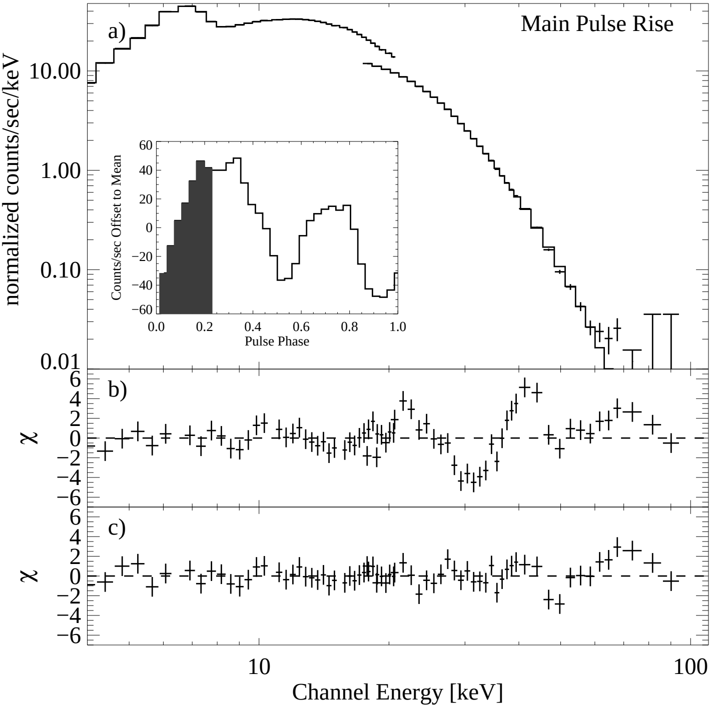

Figure 6.8: **a** Data and folded model of the rise of the main pulse for the absorbed partial covering model (see text for discussion). **b** Residuals for a fit without a CRSF, and **c** with a CRSF at $31.0^{+0.6}_{-0.5}\,keV$. The inset shows the pulse profile of GX 301−2 in the energy range from 5 keV to 20 keV. The marked region is the rise of the main pulse. Note that fitting a Gaussian shaped CRSF does not completely remove the residuals of the CRSF; the resulting fit is acceptable, but not very good ($\chi^2_{\mathrm{red}} = 1.2$). See text for a discussion.

We also searched for any yet undetected second CRSF. As the addition of a second CRSF at any energy does not improve the fit, we tried to force an additional CRSF on the best fit at twice or half the energy of the ~35 keV CRSF, especially in the phase bins where the χ^2_{red} is > 1.0 like the rise of the main pulse. A line between 15 keV and 20 keV can be excluded with very high confidence: the upper limit for the depth of a line in this energy range is less than 10^{-10}. A CRSF at twice the energy (between 60 keV and 70 keV) can not be excluded with such a high confidence, but it is still very unlikely that there is a secondary line present; the upper limit for the depth of such a line is still as low as 0.3. Therefore, we conclude that no other CRSF is present in the data; we caution, however, that the

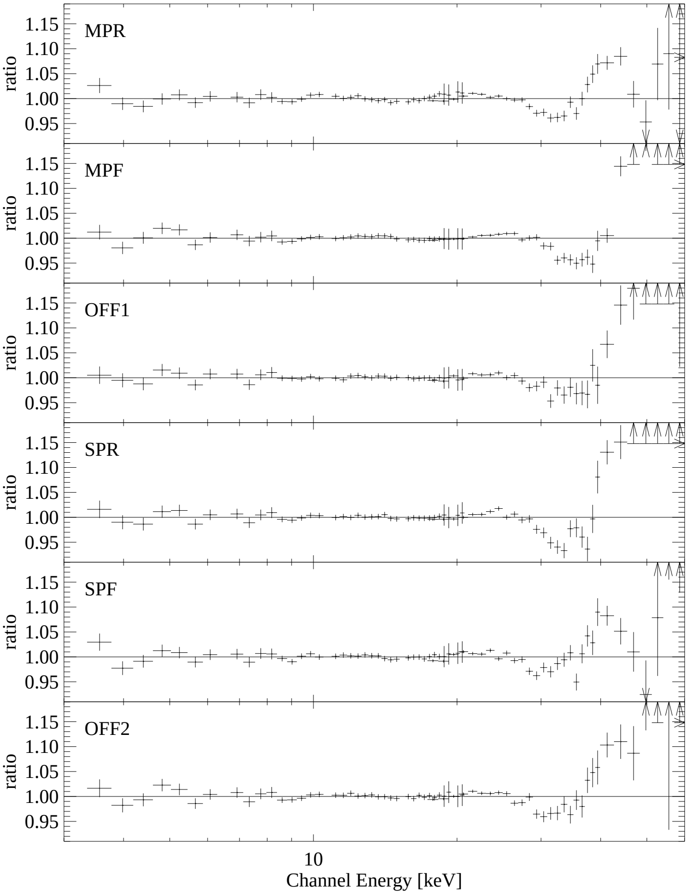

Figure 6.9: Variation of the CRSF for the six phase bins defined in Fig. 6.5). Note that not only the depth and the energy of the CRSF changes with phase but also the actual shape of the line itself seems also to be variable. See text for a discussion of these issues.

source is only weakly detected above ~60 keV and therefore we cannot exclude the presence of a feature in this energy range.

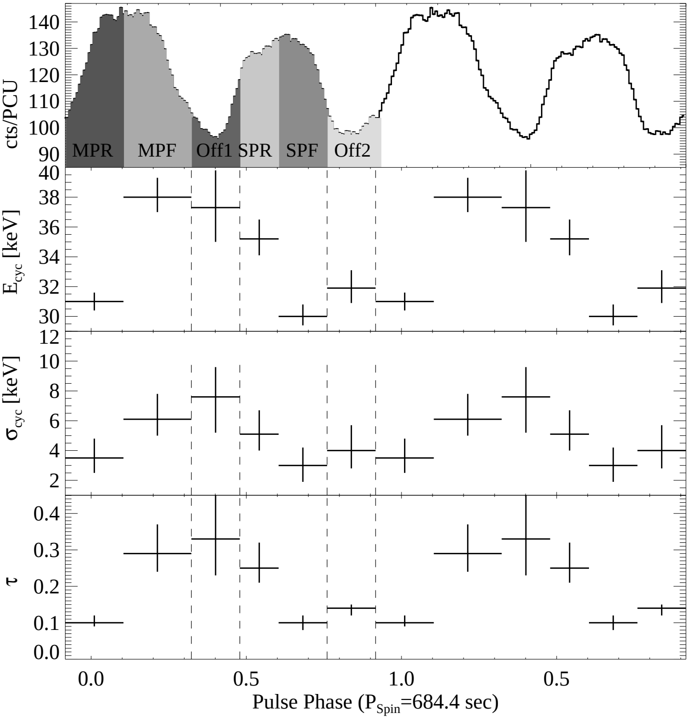

Figure 6.10: Variation of the energy and the depth of the CRSF over the pulse for the APC model. Although the values are slightly different for the REFL model, the variation of the parameters is very similar. For clarity the pulse is shown twice. **a** shows the *PCA*-countrate. Note that error bars are shown, but they are too small to be seen in print. **b** shows the variation of the energy of the CRSF over the pulse. Note that the energy variation over the pulse is definitely non-sinusoidal and therefore not due to simple angle dependence. **c** shows the variation of the depth of the CRSF over the pulse. See text for discussion.

6.4 Summary and discussion

6.4.1 CRSF Variability

The major result of this paper is the observation of a variation of the energy of the cyclotron line by almost 8 keV (corresponding to about 25%) from $30.1^{+0.8}_{-0.7}\,keV$ in the fall of the secondary pulse to $37.9^{+1.3}_{-1.0}\,keV$ in fall of the main pulse. This large variation is similar to that found in several other sources, such as 4U 1626−67 (Heindl & Chakrabarty 1999) with a variation of 25%, 4U 0115+63 with a vari-

Table 6.4: As Table 6.3, but for the reflection model (see Eq. 6.6).

Phase	N_H [10^{22}]	Γ	E_Cut [keV]	E_F [keV]	Refl	E_Fe [keV]	σ_Fe [keV]
MPR	$21.0^{+0.4}_{-1.0}$	$0.07^{+0.09}_{-0.09}$	$10.4^{+0.7}_{-1.0}$	$6.74^{+0.13}_{-0.08}$	$-3.5^{+0.3}_{-0.4}$	$6.48^{+0.02}_{-0.02}$	$0.35^{+0.04}_{-0.03}$
MPR+CRSF	$21.2^{+0.3}_{-1.2}$	$0.09^{+0.09}_{-0.17}$	$12.8^{+1.5}_{-1.6}$	$6.67^{+0.04}_{-0.10}$	$-2.6^{+0.4}_{-0.4}$	$6.47^{+0.02}_{-0.02}$	$0.35^{+0.04}_{-0.03}$
MPF	$22.0^{+1.1}_{-0.5}$	$0.20^{+0.11}_{-0.06}$	$17.2^{+0.3}_{-0.3}$	$5.98^{+0.17}_{-0.07}$	$-1.7^{+0.1}_{-0.1}$	$6.47^{+0.02}_{-0.02}$	$0.36^{+0.03}_{-0.04}$
MPF+CRSF	$21.6^{+0.8}_{-0.3}$	$0.13^{+0.12}_{-0.06}$	$15.1^{+0.7}_{-0.4}$	$6.49^{+0.16}_{-0.12}$	$-1.9^{+0.2}_{-0.2}$	$6.47^{+0.02}_{-0.02}$	$0.36^{+0.04}_{-0.03}$
OFF1	$21.7^{+0.9}_{-0.8}$	$0.14^{+0.11}_{-0.07}$	$16.9^{+0.4}_{-0.4}$	$5.65^{+0.13}_{-0.08}$	$-2.2^{+0.2}_{-0.2}$	$6.49^{+0.01}_{-0.02}$	$0.36^{+0.02}_{-0.03}$
OFF1+CRSF	$21.8^{+0.8}_{-1.4}$	$0.12^{+0.10}_{-0.11}$	$15.6^{+1.0}_{-1.4}$	$6.16^{+0.25}_{-0.25}$	$-2.5^{+0.4}_{-0.4}$	$6.49^{+0.01}_{-0.02}$	$0.35^{+0.03}_{-0.03}$
SPR	$19.9^{+0.9}_{-1.1}$	$-0.11^{+0.11}_{-0.08}$	$16.1^{+0.4}_{-0.5}$	$5.57^{+0.12}_{-0.08}$	$-2.5^{+0.3}_{-0.2}$	$6.48^{+0.02}_{-0.02}$	$0.33^{+0.03}_{-0.03}$
SPR+CRSF	$19.8^{+0.5}_{-1.4}$	$-0.13^{+0.09}_{-0.10}$	$14.8^{+0.8}_{-0.9}$	$5.91^{+0.03}_{-0.14}$	$-2.8^{+0.3}_{-0.3}$	$6.48^{+0.02}_{-0.02}$	$0.33^{+0.02}_{-0.03}$
SPF	$18.9^{+0.4}_{-1.3}$	$-0.24^{+0.10}_{-0.11}$	$11.8^{+0.9}_{-0.7}$	$6.08^{+0.08}_{-0.15}$	$-3.3^{+0.5}_{-0.3}$	$6.48^{+0.02}_{-0.02}$	$0.33^{+0.03}_{-0.03}$
SPF+CRSF	$19.1^{+0.7}_{-1.3}$	$-0.23^{+0.09}_{-0.11}$	$13.3^{+0.8}_{-1.0}$	$6.03^{+0.13}_{-0.14}$	$-2.6^{+0.4}_{-0.2}$	$6.47^{+0.02}_{-0.01}$	$0.33^{+0.02}_{-0.03}$
OFF2	$21.1^{+0.6}_{-1.2}$	$0.08^{+0.09}_{-0.09}$	$15.0^{+0.5}_{-0.5}$	$5.86^{+0.05}_{-0.11}$	$-3.2^{+0.3}_{-0.2}$	$6.49^{+0.02}_{-0.02}$	$0.36^{+0.03}_{-0.03}$
OFF2+CRSF	$21.5^{+0.2}_{-0.2}$	$0.10^{+0.01}_{-0.01}$	$15.4^{+0.1}_{-0.4}$	$5.96^{+0.02}_{-0.01}$	$-2.9^{+0.1}_{-0.0}$	$6.49^{+0.01}_{-0.02}$	$0.35^{+0.02}_{-0.02}$

Phase	τ_C	E_C [keV]	σ_C	χ	(dof)	χ^2_red	Flux
MPR	–	–	–	234.8	(60)	3.91	1.87×10^{-9}
MPR+CRSF	$0.14^{+1.01}_{-0.03}$	$31.8^{+0.4}_{-0.6}$	$2.2^{+1.2}_{-2.0}$	79.1	(63)	1.26	
MPF	–	–	–	356.9	(60)	5.95	1.93×10^{-9}
MPF+CRSF	$0.28^{+0.06}_{-0.03}$	$38.7^{+1.5}_{-0.8}$	$4.7^{+1.5}_{-1.0}$	51.0	(63)	0.81	
OFF1	–	–	–	125.6	(60)	2.09	1.37×10^{-9}
OFF1+CRSF	$0.28^{+0.20}_{-0.08}$	$38.8^{+3.4}_{-2.8}$	$6.3^{+2.9}_{-2.3}$	49.7	(63)	0.79	
SPR	–	–	–	222.5	(60)	3.71	1.47×10^{-9}
SPR+CRSF	$0.29^{+0.11}_{-0.05}$	$35.6^{+1.7}_{-1.0}$	$2.9^{+1.1}_{-1.1}$	55.5	(63)	0.88	
SPF	–	–	–	144.6	(60)	2.41	1.52×10^{-9}
SPF+CRSF	$0.09^{+0.02}_{-0.02}$	$32.0^{+0.8}_{-0.8}$	$0.9^{+1.6}_{-0.8}$	82.9	(63)	1.32	
OFF2	–	–	–	158.5	(60)	2.64	1.31×10^{-9}
OFF2+CRSF	$0.14^{+0.04}_{-0.02}$	$32.5^{+0.5}_{-0.4}$	$3.1^{+0.9}_{-0.6}$	55.7	(63)	0.88	

ation of 20% in the 1st harmonic (Heindl et al. 1999b; Santangelo et al. 1999), Cen X-3 with a variation of 30% (Burderi et al. 2000), or Her X-1 with ~25% (Gruber et al. 2001, 1980). On the other hand, the energies of the CRSFs in Vela

X-1 varies only by ~10% with pulse phase (Kreykenbohm et al. 2002a). Consistent with earlier interpretations, the strong energy variation of the cyclotron line in GX 301−2 argues that during different phases of the X-ray pulse, regions with different magnetic fields are observed. There are several plausible scenarios for such a suggestion.

First consider a simple scenario that we observe an accretion column in a pure dipole field. In such a case the observed 25% change of the cyclotron line energy would translate into a change in the height of the scattering region of ~5 km (or ~50% of the neutron star radius). Such a change is rather unlikely, given that accretion columns are generally predicted to have heights of less than 1 km (Burnard et al. 1991; Becker 1998; Brown & Bildsten 1998). Apart from these theoretical considerations, a very tall accretion column would also imply a rather uncommon magnetic field configuration for GX 301−2: For a ~5 km high accretion column, the emission pattern is very likely a pure fan beam. To entirely block the lower parts of the accretion column such that the X-ray spectrum is dominated by the "top" of the column requires that the angle between the magnetic field axis and the spin axis, β, is at least 40°, and larger if relativistic light bending is included. Detailed models for the emission pattern of XRBs, which include relativistic light propagation (Kraus et al. 1996; Blum & Kraus 2000), as well as the statistical analysis of accreting neutron star pulse profiles (Bulik et al. 2003), however, imply $\beta \lesssim 20°$. We conclude, therefore, that the accretion column of GX 301−2 is much lower than what would be expected if the variation of E_C were due to a pure dipole field geometry.

A second possibility for the cyclotron line variability, which has been discussed, e.g., for Cen X-3, would be the presence of a very wide polar cap. For a dipole configuration, Burderi et al. (2000) show that an opening angle of the order of 55° is required to produce a 30% variation of the line energy. Such a large polar cap, however, is unlikely to produce the observed X-ray pulse shape – the pulse profile is expected to be much broader in this case. Furthermore, as already noted by Burderi et al. (2000), such large polar caps would imply that the line energy varies symmetrically about the pulse maximum, which is not the case for any of the pulsars with a strong variation of the line energy. Finally, we also note that the strong magnetic field confines the accreting plasma, resulting in a much smaller opening angle of the neutron star's hot spot (Litwin et al. 2001; Becker 1998; Basko & Sunyaev 1976). As a result we conclude that the extended polar cap scenario is an unlikely explanation for the large variation of the energy of the CRSF.

A third and final scenario for the pulse variation is that the observed X-rays come from an accretion mound, as suggested, e.g., by Burnard et al. (1991). In this case the observed variation of the line energy is mainly due to the higher multipole components of the magnetic field in the mound and the X-ray emissivity profile is a combination of a fan and a pencil beam.

Parenthetically, we note that slight variations of the line energy are also predicted for the case of homogeneous magnetic fields, as the location, depth, and shape of the CRSF are predicted to change with viewing angle, i.e., pulse phase (Mészáros & Nagel 1985; Isenberg et al. 1998b; Araya & Harding 1999; Araya-Góchez & Harding 2000). The strongest of these effects are the emission wings of the fundamental CRSF caused by "photon spawning" (Araya & Harding 1999; Araya-Góchez & Harding 2000), where electrons excited into a higher Landau level by resonant scattering of a photon, decay into the ground state by emitting photons at an energy which is roughly that of the fundamental CRSF. As a result the fundamental line is predicted to be shallower and have a more complex shape than the higher harmonics. When folded through the *HEXTE* response matrix, these variable complex line profiles can result in slight changes of the measured line energy. These changes, however, are much smaller than the 25% energy variation seen here, and can thus be excluded as the cause for the observed variation. Nevertheless, the inspection of the residuals of the pulse phase resolved fits indicates a possible change of the shape of the CRSF over the pulse (Fig. 6.9). Similar to, e.g., 4U 0115+63 (Heindl et al. 1999b; Santangelo et al. 1999), the presence of an unresolved complex structure of the fundamental could be postulated to explain the not fully satisfactory χ^2 values in some phase bins (e.g., $\chi^2_{\text{red}}\sim 1.2$ for bin MPR (see Fig. 6.8), as compared to $\chi^2_{\text{red}} < 1.0$ in the other phase bins). With the increasing energy resolution of modern gamma-ray detectors, it is foreseeable that such profiles will be resolvable with newer instruments such as, e.g., the SPI instrument on INTEGRAL.

6.4.2 Implications of the Line variability

In recent years, several groups have searched for correlations between the parameters of the CRSF and the X-ray continuum in the hope of deducing information about the line and continuum formation process (Makishima et al. 1999; Coburn 2001, and references therein). A major disadvantage of these searches, however, has been that they typically used pulse *averaged* data instead of pulse resolved spectroscopy, complicating the interpretation of the correlations found.

One of the most interesting new correlations found in the large sample of X-ray pulsars observed with *RXTE* and analyzed in a uniform manner by Coburn (2001) and Coburn et al. (2002) has been between the relative width of the CRSF, σ/E, and its depth, τ. As noted by Coburn et al. (2002), part of the σ/E_{cyc}–τ-plane is inaccessible to *RXTE* due to observational constraints; however, our data all fall into the range that is well observable. As shown in Fig. 6.11, our phase resolved results for GX 301−2 confirm the overall correlation: deeper CRSFs are generally broader. We note that this agreement between the phase averaged and the phase resolved data suggests that the correlations found by Coburn et al. (2002) from the phase averaged data are indeed real and not due to effects of the averaging.

Having many data points for one object helps in understanding the σ/E_{cyc}-τ correlation in terms of a physical model. As we have outlined in the previous section, it is likely that the X-rays observed from GX 301−2 are produced in an accretion mound of moderate height at the magnetic poles of the neutron star. Consider first the case that only one pole is visible. Over the X-ray pulse we view this pole under different viewing angles, θ, where θ is the angle between the line of sight and the magnetic field in the accretion column. For the high temperatures of the accretion column, the line width is expected to be dominated by thermal broadening. As shown, e.g., by Mészáros & Nagel (1985), the anisotropic velocity field of the electrons in the accretion column leads to fractional line widths of

$$\frac{\sigma}{E_{\mathrm{C}}} \propto \sqrt{\frac{kT_{\mathrm{e}}}{m_{\mathrm{e}}c^2}\cos^2\theta} \tag{6.7}$$

where kT_{e} is the temperature of the electrons along the magnetic field lines. Basic Comptonization theory suggests that kT_{e} can be estimated from the folding energy of the pulsar continuum, E_{F} (e.g., Burderi et al. 2000, and references therein). If we furthermore assume that the seed photons for the Compton upscattering in the accretion column are created throughout the volume of the accretion column, then detailed Monte Carlo simulations, e.g., of Isenberg et al. (1998b) show that the depth τ of the CRSF is expected to be largest when the line of sight is almost perpendicular to the direction of the magnetic field. For a uniform temperature accretion column, where kT_{e} is constant, these models thus predict an anti correlation between τ and σ/E_{C}, in contradiction to the observation.

We note, however, that even phase resolved data are difficult to interpret. In the above discussion, we assumed that the observed data are dominated by emission from one homogeneous emission region. In reality, this is not the case and the observed data are generally a mixture of contributions from both magnetic poles, which could influence the observed correlation. While it is difficult to disentangle the contributions from the two poles (Kraus et al. 1996; Blum & Kraus 2000), it seems likely that the physical conditions at both poles are slightly different. We would then expect the parameters of the X-ray continuum emitted by each pole to be different, which would be reflected by changes in the observed continuum parameters. In GX 301−2, however, the continuum parameters as exemplified by E_{F} are remarkably stable, suggesting either that only one magnetic pole contributes to the observed data, or that the poles have similar temperature. For this reason,

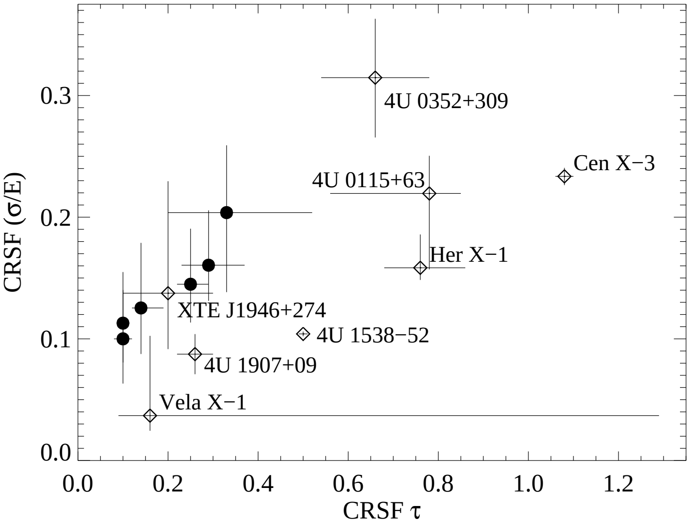

Figure 6.11: Fractional CRSF width σ/E_C versus the depth of the CRSF for several accreting neutron stars from *RXTE* data. Diamonds: values derived by Coburn et al. (2002) from phase averaged spectra. Filled circles: values derived from phase resolved spectra for GX 301−2 (this work).

it seems unlikely that a mixture of flux from the two poles causes the observed $\sigma_\mathrm{C}/\tau_\mathrm{C}$ correlation. Given the contradiction with simple theory, it appears that additional physical processes must occurring.

Finally, we note a second correlation found in our phase resolved data, that is also present in the phase average data (Coburn et al. 2002): a correlation between the line width σ_C and the energy of the line E_C shown in Fig. 6.12. In terms of the simple cyclotron line broadening theory of Eq. 6.7 this correlation is rather unexpected since such a strong correlation (0.93 for GX 301−2) is only possible if $\cos\theta$ does not vary appreciably. A variation of θ is required, however, since strong X-ray pulses are observed. Since the variation of $\cos\theta$ is fastest for $\theta \sim 90^\circ$, the good degree of correlation implies that θ is close to 0. As an example, for $\theta = 60^\circ$, the correlation constrains the viewing angle to vary by $\pm 6^\circ$ around its mean value, even tight in the case of a pure fan beam.

6.4.3 Summary

To summarize, our analysis of the *RXTE* data of GX 301−2 shows

1. The continuum of GX 301−2 is well described by an absorbed and partially

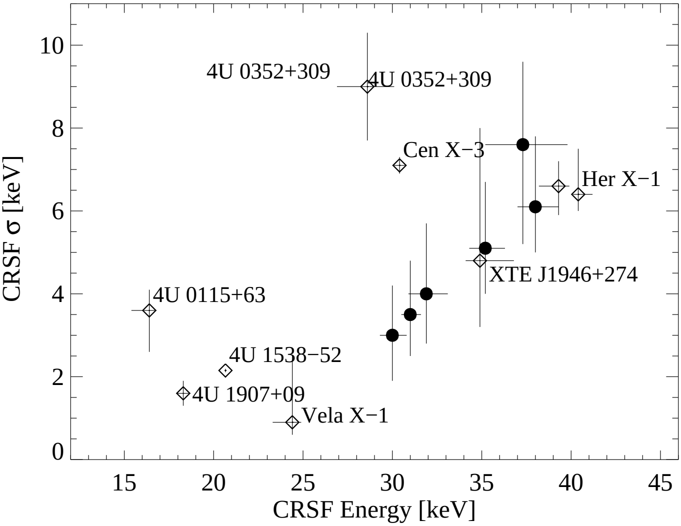

Figure 6.12: CRSF width σ_C versus CRSF Energy E_C for the same sample of accreting neutron stars as in Fig. 6.11. Note the very strong correlation between E_C and σ_C for GX 301−2 (correlation coefficient 0.93; filled circles).

covered pulsar continuum model. An alternative explanation for the X-ray spectrum is a reflected and absorbed pulsar continuum. Current data do not allow us to distinguish between these alternatives.

2. GX 301−2 shows a strong cyclotron line at an energy of ∼35 keV. The line energy, depth, and width are variable with the pulse phase and do not depend on the chosen continuum model.

3. The variability of the CRSF energy as well as the pulse profile suggest that the X-rays from GX 301−2 originate in an accretion mound, and that the change in energy is not due to a change in height in a dipole field.

4. The correlation between the relative width of the line and its depth is suggestive of changes in the angle between the line of sight and the magnetic field at the neutron star pole, in agreement with the standard paradigm for pulsating X-ray sources, but contradiction with the numerical simulations for the depth of the line.

CHAPTER 7

The Future

In the previous chapters I discussed the presence of a second cyclotron line in the spectrum of Vela X-1 and the variability of the line in GX 301−2. Although both systems are relatively similar (neutron stars accreting from the stellar wind of an evolved early type star), the properties of observed lines are quite different.

The 50 keV line of Vela X-1 is strong and well detected in all phases. While its depth varies significantly over the pulse, the width and energy of this line also vary, but not significantly. The 25 keV line in Vela X-1 is very difficult to detect and seems even not always be present, as La Barbera et al. (2003) fail to detect the line. Like the 50 keV line, this line also shows some variability over the pulse: the depth is significantly larger during the main pulse, while it is almost constant outside the main pulse; a behavior that is quite different from what is observed for the 50 keV line. Although the variability of the energy of the line is more pronounced than for the 50 keV line, the energy is still consistent with a constant value in most phase bins; the same applies to the width of the line.

In the case of GX 301−2, no secondary line could be observed, despite the good quality of the data. The line of GX 301−2 also behaves differently compared to the Vela X-1 lines. The energy of the line varies strongly over the pulse – changing by more than 25% from the fall of the secondary pulse to the pulse maximum (30 keV vs. 38 keV). Unlike Vela X-1, the line is deepest from the fall of the main pulse to the rise of the secondary pulse (including the pulse minimum) and remains quite shallow during the other phase bins. The depth of the line is strongly correlated with the width of the line: when the line is deep, it is also broad and vice versa.

The strong correlations between energy, width and depth of a cyclotron line found by Coburn et al. (2002) are also true for data from different pulse phases as shown in Figs 6.11 and 6.12. Apparently, the correlations found for GX 301−2 are also true when comparing values from different sources derived using phase *averaged* spectra.

While we observe some common behavior between different sources (they all follow the discussed correlations), individual sources can behave very differently (e.g., much weaker variation of the cyclotron parameters over the pulse for Vela X-1).

As discussed in the previous two chapters, the reason for this behavior and the difference between these similar sources still remains unknown.

Another also very interesting subject are the energy resolved pulse profiles: again, the pulse profiles of Vela X-1 and GX 301−2 are similar in the sense that both show a double pulse. But the evolution of the energy resolved pulse profiles from low to high energies is very different. While Vela X-1 shows a very complex structure below ~10 keV with five pulses (one of these is even in the inter pulse region), GX 301−2 shows a less complex double pulse at higher and lower energies. Many propositions have been made to explain the complicated pulse profile structure of Vela X-1 at lower energies, but none of these are satisfying, in the sense that they either cannot explain the energy dependent pulse profiles and/or fail to describe the long term stability of the pulse profiles (e.g., varying absorption over the pulse cannot explain the stability of the pulse profile over decades).

7.1 *RXTE*

Despite the comparably low energy resolution of *RXTE*, the instrument has proven to be very effective in detecting new cyclotron lines (see Table 3.1 for the many new detections). Its timing capabilities together with the large effective area of the *PCA* (see Chapter 4) make *RXTE* an ideal instrument to study the temporal behavior of these sources, namely pulse phase resolved spectroscopy and energy resolved pulse profiles.

Even after eight years of operation, *RXTE* is still working very well and collecting each day more data. The *RXTE* archive harbors tons of data of all X-ray pulsars in the meantime. As this thesis shows, phase resolved spectroscopy is required to analyze the data of accreting X-ray pulsars. Phase resolved spectroscopy, however, is a time consuming process, and has therefore been done only for a few sources and only a small fraction of the publicly available data has been used (two detailed studies are presented in this thesis).

In the future, as much *RXTE* data as possible should be analyzed using phase resolved spectroscopy, continuing the work of this thesis. One of the most interesting sources is Hercules X-1 – the first cyclotron source. The line in this source is known to vary similarly to GX 301−2 (Soong et al. 1990), however, the previous phase resolved analysis of Soong et al. (1990) used a different spectral model (with a fixed width for the CRSF); furthermore the high quality *RXTE* data of Her X-1 have not been analyzed yet using thorough phase resolved spectroscopy, but this analysis is under way. But for most sources, phase resolved spectroscopy has never been done (especially not with high signal to noise as *RXTE* can provide), therefore it is most urgent to analyze these data as well.

If phase resolved analyses exist for a substantial amount of the cyclotron sources, the phase averaged data points in Fig. 6.11 and Fig. 6.12 can be replaced by the phase resolved ones. This will put much more leverage on their interpretation, as phase averaged results do not contain the full information available.

The conclusions drawn in Section 6.4 can then be put on a much broader basis. This again can then be used as input for the theoretical discussion of the formation process of cyclotron lines.

Parallel to using the conventional models used in this thesis to fit the data, the Monte Carlo code by Araya-Góchez & Harding (2000) presented in Section 3.4.2, should be checked and enhanced. This modified code can then be used to calculate a fine grid for all possible parameter combinations. This grid can be converted into a table model for *XSPEC* and fit to the data. The new model will not necessarily describe the data "better" (in terms of χ^2_{red}) than a simple absorption line model, but at any rate it is very well possible that some of the deviations seen in GX 301−2 when fitting the cyclotron line with a simple Gaussian, can be described by the simulated spectra. The resulting parameters of such a model, however, provide a direct description of the conditions in the cyclotron formation region (e.g., electron temperature).

Once this model produces reliable results, the resulting parameters of the different objects can be compared directly instead of comparing simple fitting parameters like the width of the line. This will then hopefully also allow to get a much more detailed insight into the conditions and processes in the accretion column and will also help to explain, why similar objects behave so differently.

7.2 INTEGRAL

On 2002 October 17, ESAs International Gamma-Ray Astrophysics Laboratory (*INTEGRAL*) was launched (for a description of the instrument, see Winkler et al. 2003). *INTEGRAL* has four science instruments: the spectrometer SPI (Vedrenne et al. 2003), the imager IBIS (Ubertini et al. 2003), the X-ray monitor JEM-X (Lund et al. 2003), and the optical monitor OMC (Mas-Hesse et al. 2003). These instruments provide coverage from ~2 keV up to 10 MeV, an increase compared to *RXTE* by a factor of 100. The spectral energy resolution of SPI and IBIS is also much better than that of *RXTE*: 8 keV at 100 keV for IBIS and 3 keV for SPI at 1.7 MeV.

Due to the high spectral resolution of SPI and IBIS, it will be possible to resolve

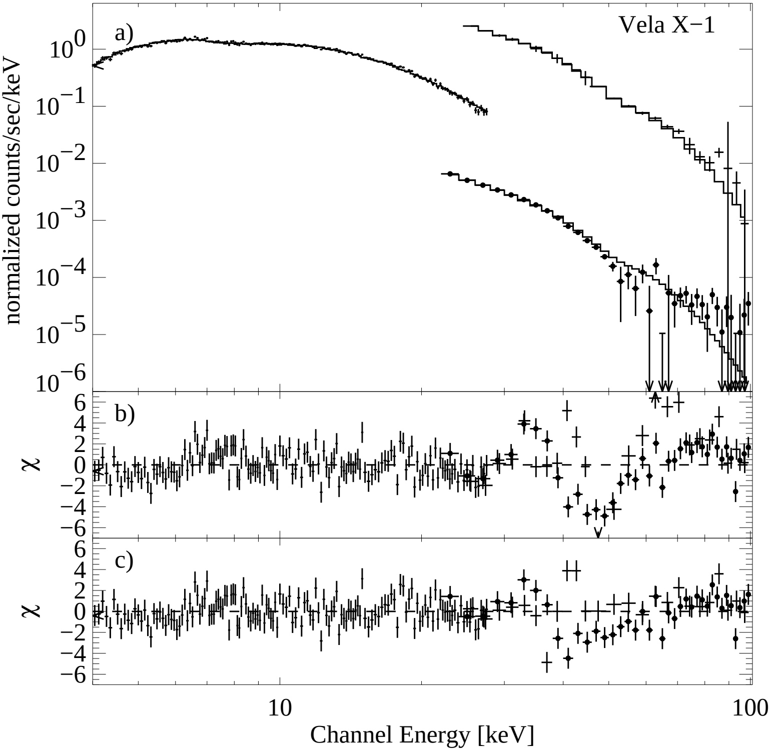

Figure 7.1: A phase averaged spectrum of Vela X-1 as observed by *INTEGRAL*. **a** shows the count rate spectrum and the model. The three instruments in use are JEM-X (low energies), IBIS and SPI (filled circles) for higher energies. The spectrum uses all data when Vela X-1 was in the field of view of the instruments during the Vela region core program in summer 2003 and the source was not in eclipse. **b** shows the residuals without the inclusion of a CRSF. Note that the cyclotron line at ~50 keV is clearly detected. **c** with the inclusion of a CRSF at $51.5^{+0.5}_{-0.7}$ keV. Note also that IBIS and SPI do not agree on the actual shape of the line which might be due to calibration problems in IBIS.

the cyclotron lines and their wings. This will then allow us to really fit the lines using the Monte Carlo models (see Section 3.4.2) to accurately determine the physical parameters of the line formation region.

Together with a very high sensitivity and a highly eccentric orbit with a period of ~72 h, *INTEGRAL* is the almost ideal instrument to observe accreting X-ray pulsars. Due to the exponentially falling continua of accreting X-ray pulsars and lower effective area (compared to the *PCA*), however, long exposure times are required to obtain high signal to noise spectra also at higher energies.

During the core program, *INTEGRAL* scans repeatedly the galactic plane (Galactic Plane Scan, GPS). Since many stellar X-ray sources are located close to the Galactic plane, the GPS allows to monitor many X-ray sources like GX 301−2 and Cen X-3 over a long time, although the monitoring can be quite coarse for some sources (e.g., in the 2003, Cen X-3 has been observed only three or four times). This monitoring already lead to the discovery of a new class of objects (Walter et al. 2003): heavily absorbed sources which are invisible at lower energies (therefore they could not be detected by other monitoring instruments like the *ASM*).

At the writing of this thesis, only first and very preliminary results are available, however, the analysis is ongoing. A first spectrum of Vela X-1 using data from the Vela region core program is shown in Fig. 7.1. The spectrum shown is analyzed just on a quick-look basis and is meant as a starting point for a detailed and ongoing analysis. The spectrum shown is a phase averaged spectrum, as the software for phase resolved spctroscopy is currently under development and therefore not yet available.

As the preliminary spectrum in Fig. 7.1 already clearly shows, *INTEGRAL* is really a big step forward for the analysis of accreting X-ray pulsars. With more data (not only for Vela X-1) to come, it will be possible in the future to model the spectra with much more detail which will then hopefully allow to put real constraints on the physical parameters of the line formation region and the whole accretion column itself.

Bibliography

Adams, J. D., Stauffer, J. R., Monet, D. G., Skrutskie, M. F., & Beichman, C. A. 2001, AJ, 121, 2053

Alexander, S. G., Davila, J., & Dimattio, D. J. 1996, ApJ, 459, 666

Alves, J. & Homeier, N. 2003, Astrophys. J., Lett., 589, L45

Araya, R. A. & Harding, A. K. 1996, ApJ, 463, L33

—. 1999, ApJ, 517, 334

Araya-Góchez, R. A. & Harding, A. K. 2000, ApJ, 544, 1067

Arnaud, K. A. 1996, in Astronomical Data Analysis Software and Systems V, ed. J. H. Jacoby & J. Barnes, ASP Conf. Ser. 101, San Francisco, 17

Arquilla, R. & Goldsmith, P. F. 1986, ApJ, 303, 356

Aschenbach, B., Hahn, H., Trümper, J., & Jenkner, H. 1998, The Invisible Sky – ROSAT and the Age of X-Ray Astronomy (New York: Springer-Verlag)

Ashworth, M., Lyne, A. G., & Smith, F. G. 1983, Nature, 301, 313

Baade, W. & Zwicky, F. 1934, Phys. Rev., 45, 130

Barbera, A. L., Burderi, L., Di Salvo, T., Iaria, R., & Robba, N. R. 2001, ApJ, 553, 375

Bardeen, J. & Stephen, M. J. 1965, Physical Review, 140, 1197

Barziv, O., Kaper, L., van Kerkwijk, M. H., Telting, J. H., & van Paradijs, J. 2001, A&A, accepted, astro-ph/0108237

Basko, M. M. & Sunyaev, R. A. 1975, A&A, 42, 311

—. 1976, MNRAS, 175, 395

Baym, G., Pethick, C., & Pines, D. 1969, Nature, 224, 673

Becker, P. A. 1998, ApJ, 498, 790

Beichmann, C. A., Jennings, R. E., Emerson, J. P., et al. 1984, ApJ, 278, L45

Benlloch-Garcia, S. 2003, PhD thesis, University of Tübingen, Tübingen

Bethe, H. A. 1939, Phys. Rev., 55, 434

Bethe, H. A. & Critchfield, C. L. 1938, Phys. Rev., 54, 248

Bevington, P. R. & Robinson, D. K. 1992, Data Reduction and Error Analysis for the Physical Sciences (Boston: McGraw-Hill)

Bhattacharya, D. & Srinivasan, G. 1995, in X-Ray Binaries, ed. W. H. G. Lewin, J. van Paradijs, & E. P. J. van den Heuvel (Cambridge: Cambridge University Press), 495–522

Bhattacharya, D., Wijers, R. A. M. J., Hartman, J. W., & Verbunt, F. 1992, A&A, 254, 198

Bichenkov, E. I. & Shvetsov, G. A. 1997, Journal of Applied Mechanics and Technical Physics, 38, 578

Bildsten, L., Chakrabarty, D., Chiu, J., et al. 1997, Astrophys. J., Suppl. Ser., 113, 367

Bisnovaty-Kogan, G. S., Kazhdan, Y. M., Klypin, A. A., Lutskii, A. E., & Shakura,

N. I. 1979, Astron. Zh., 56, 359
Blum, S. & Kraus, U. 2000, ApJ, 529, 968
Boella, G., Butler, R. C., Perola, G. C., et al. 1997, A&AS, 122, 299
Bondi, H. & Hoyle, F. 1944, MNRAS, 104, 273
Borra, E. F., Landstreet, J. D., & Mestel, L. 1982, ARA&A, 20, 191
Bowyer, S., Byram, E. T., Chubb, T. A., & Friedman, H. 1965, Science, 147, 394
Bradt, H., Rappaport, S., Mayer, W., et al. 1969, Nature, 222, 728
Bradt, H. V., Rothschild, R. E., & Swank, J. H. 1993, A&AS, 37, 355
Braes, L. L. E. & Miley, G. K. 1971, Nature, 232, 246
Brainerd, J. J. & Mészáros, P. 1991, ApJ, 369, 179
Börner, G., Hayakawa, S., Nagase, F., & Anzer, U. 1987, A&A, 182, 63
Brown, E. F. & Bildsten, L. 1998, ApJ, 496, 915
Bulik, T., Gondek-Rosińska, D., Santangelo, A., et al. 2003, A&A, 404, 1023
Burbidge, E. M., Burbidge, G. R., Fowler, W. A., & Hoyle, F. 1957, Rev. Mod. Phys., 29, 547
Burderi, L., Di Salvo, T., Robba, N. R., La Barbera, A., & Guainazzi, M. 2000, ApJ, 530, 429
Burnard, D. J., Arons, J., & Klein, R. I. 1991, ApJ, 367, 575
Burnard, D. J., Klein, R. I., & Arons, J. 1990, ApJ, 349, 262
Canizares, C. R. 1990, Adv. Space Res., 10, 261
Chandrasekhar, S. 1931, ApJ, 74, 81
Choi, C. S., Dotani, T., Day, C. S. R., & Nagase, F. 1996, ApJ, 471, 447
Clark, G. W., Woo, J. W., Nagase, F., Makishima, K., & Sakao, T. 1990, ApJ, 353, 274
Coburn, W. 2001, Ph.D. Thesis, University of California, San Diego
Coburn, W., Heindl, W. A., Gruber, D. E., et al. 2001, ApJ, 552, 738
Coburn, W., Heindl, W. A., Rothschild, R. E., et al. 2002, ApJ, 580, 394
Cocke, W. J., Disney, M. J., & Tayler, D. J. 1969, Nature, 221, 525
Comastri, A., Fiore, F., Giommi, P., et al. 1999, preprint
Comastri, A., Setti, G., Zamorani, G., & Hasinger, G. 1995, A&A, 296, 1
Córdova, F. A.-D. 1995, in X-ray binaries, ed. W. H. G. Lewin, J. van Paradijs, & E. P. J. van den Heuvel, Cambridge Astrophysics Series (Cambridge: Cambridge University Press), 331–390
Cusumano, G., Di Salvo, T., Burderi, L., et al. 1998, A&A, 338, L79
Dal Fiume, D., Orlandini, M., Cusumano, G., et al. 1997, A&A
Davidson, K. & Ostriker, J. P. 1973, ApJ, 179, 585
de Kool, M. & Anzer, U. 1993, MNRAS, 262, 726
Deeter, J. E., Boynton, P. E., Lamb, F. K., & Zylstra, G. 1989, ApJ, 336, 376
Domingo, V., Fleck, B., & Poland, A. I. 1995, Sol. Phys., 162, 1
Dubath, P., Revnivtsev, M., Goldoni, P., et al. 2003, in International Astronomical Union Circular, 1–+
Duncan, R. C. 1992, ApJ, 392, L9
Eddington, A. S. 1930, The Internal Constitution of the Stars (Cambridge: Cambridge University Press)
Eggen, O. J. & Iben, I. J. 1988, AJ, 96, 635
Einstein, A. 1905, Annalen der Physik, 18, 639
Emerson, J. P. 1987, in IAU Symp. 115: Star Forming Regions, 19–30
Finger, M. H., Wilson, R. B., & Hagedon, K. S. 1994a, in International Astronomical Union Circular, 1–+

Finger, M. H., Wilson, R. B., & Harmon, B. A. 1994b, in International Astronomical Union Circular, 1

Fiore, F., La Franca, F., Giommi, P., et al. 1999, MNRAS, preprint

Forman, W., Jones, C., Cominsky, L., et al. 1978, Astrophys. J., Suppl. Ser., 38, 357

Frank, J., King, A., & Raine, D. 1992, Accretion Power in Astrophysics, 2nd edn. (Cambridge, New York, Melbourne: Cambridge University Press)

Fritz, G., Henry, R. C., Meekins, J. F., Chubb, T. A., & Friedmann, H. 1969, Science, 164, 709

Fujimoto, M. Y., Hanawa, T., Iben, I., & Richardson, M. B. 1984, ApJ, 278, 813

Genzel, R. 1992, in The galactic interstellar medium, ed. D. Pfenniger & P. Bartholdi, Saas-Fee Advanced Course (Heidelberg: Springer), 275–393

Geppert, U. & Urpin, V. 1994, MNRAS, 271, 490

Gerthsen, C. & Vogel, H. 1993, Physik (Heidelberg: Springer)

Ghosh, P. & Lamb, F. K. 1978, Astrophys. J., Lett., 223, L83

Ghosh, P. & Lamb, F. K. 1979a, ApJ, 232, 259

—. 1979b, ApJ, 234, 296

Giacconi, R., Gursky, H., Kellogg, E., Schreier, E., & Tananbaum, H. 1971, Astrophys. J., Lett., 167, L67

Giacconi, R., Gursky, H., Paolini, F. R., & Rossi, B. B. 1962, Phys. Rev. Lett., 9, 439

Giacconi, R., Kellogg, E., Gorenstein, P., Gursky, H., & Tananbaum, H. 1971, ApJ, 165, L27

Ginzburg, V. L. 1964, Sov. Phys. – Dokl., 9, 329

Gold, T. 1968, Nature, 218, 731

Gruber, D. E. 1997, private communication

Gruber, D. E., Blanco, P. R., Heindl, W. A., et al. 1996, A&AS, 120, 641

Gruber, D. E., Heindl, W. A., Rothschild, R. E., et al. 2001, ApJ, 562, 499

Gruber, D. E., Matteson, J. L., Nolan, P. L., et al. 1980, ApJ, 240, L127

Grupen, C. 1993, Teilchendetektoren (Mannheim: BI Wissenschaftsverlag)

Haberl, F. & White, N. E. 1990, ApJ, 361, 225

Haigh, N. J., Coe, M. J., Steele, I. A., & Fabregat, J. 1999, MNRAS, 310, L21

Harding, A. K. 1994, in Proc. conf. The Evolution of X-ray Binaries, ed. S. Holt & C. S. Day, AIP Conference Proceedings 308, 429

Harding, A. K. & Daugherty, J. K. 1991, ApJ, 374, 687

Harding, A. K. & Mészáros, P. 1984, ApJ, 369

Hasinger, G. 2002, in Conf. Proc. "New Visions of the X-ray Universe in the XMM-Newton and Chandra Era", ed. F. Jansen, Vol. ESA-SP 488

Hayasaki, K. & Okazaki, A. T. 2003, ArXiv Astrophysics e-prints, astro-ph/0311225

Hayashi, C. 1961, PASJ, 13, 450

Heindl, W., Coburn, W., Kreykenbohm, I., & Wilms, J. 2003, The Astronomer's Telegram, 200, 1

Heindl, W. A. & Chakrabarty, D. 1999, in Highlights in X-ray Astronomy, 25–28

Heindl, W. A., Coburn, W., Gruber, D. E., et al. 1999a, in Proc. 5th. Compton Symposium, AIP Conf. Proc., 510, asotr-ph/0004297

Heindl, W. A., Coburn, W., Gruber, D. E., et al. 2000, AAS/High Energy Astrophysics Division, 32, 2207

—. 1999b, ApJ, 521, L49

—. 2001, ApJ, in press

Herbig, G. 2002, in Physics of Star Formation in Galaxies, ed. F. Palla & H. Zinnecker, Saas Fee Advanced Course (Hei-

delberg: Springer), 1–8
Herold, H. 1979, Phys. Rev. D, 19, 2868
Herrero, A., Kudritzki, R. P., Gabler, R., Vilchez, J. M., & Gabler, A. 1995, A&A, 297, 556
Hertzsprung, E. 1911, Publikationen des Astrophysikalischen Observatoriums zu Potsdam, 63
Hewish, A., Bell, S. J., Pilkington, J. D. H., Scott, P. F., & Collins, R. A. 1968, Nature, 217, 709
Hjellming, R. M. & Wade, C. M. 1971, ApJ, 168, L21
Hoyle, F., Narlikar, J., & Wheeler, J. A. 1964, Nature, 203, 914
Hua, X.-M. & Titarchuk, L. 1995, ApJ, 449, 188
Iben, I. 1991, Astrophys. J., Suppl. Ser., 76, 55
Iben, Jr., I. & Tutukov, A. V. 1984, ApJ, 54, 335
—. 1985, ApJS, 58, 661
Illarionov, A. F. & Sunyaev, R. A. 1975, A&A, 39, 185
Inoue, H., Ogawara, Y., Ohashi, T., & Waki, I. 1984, PASJ, 36, 709
Isenberg, M., Lamb, D. Q., & Wang, J. C. L. 1998a, ApJ, 493, 154
—. 1998b, ApJ, 505, 688
Jahoda, K., Swank, J. H., Giles, A. B., et al. 1996, in EUV, X-ray, and Gamma-Ray Instrumentation for Astronomy VII, Proc. SPIE, ed. O. H. Siegmund & M. A. Gummin, Vol. 2808, SPIE, 59–70
Jurewicz, A. J. G., Burnett, D. S., Wiens, R. C., & Woolum, D. 2000, in Lunar and Planetary Institute Conference Abstracts, 1783
Kaler, J. B. 1994, Sterne und ihre Spektren (Heidelberg: Spektrum Akademischer Verlag)
Kaper, L., Lamers, H. J. G. L. M., Ruymaekers, E., van den Heuvel, E. P., & Zuiderwijk, E. J. 1995, A&A, 300, 446
Karttunen, H., Kröger, P., Oja, H., Poutanen, M., & Donner, K. J. 1990, Astronomie – Eine Einführung (Heidelberg: Springer), 273
Kellogg, E. M. 1975, ApJ, 197, 689
Kendziorra, E., Kretschmar, P., Pan, H. C., et al. 1994, A&A, 291, L31
Kendziorra, E., Mony, B., Kretschmar, P., et al. 1992, in Frontiers of X-Ray Astronomy, Proc. XXVIII Yamada Conf., ed. Y. Tanaka & K. Koyama, Frontiers Science Series, 2, 51–52
Kessler, M. F., Steinz, J. A., Anderegg, M. E., et al. 1996, A&A, 315, L27
King, A. 1995, in X-ray Binaries, ed. W. H. G. Lewin, J. van Paradijs, & E. P. J. van den Heuvel, Cambridge Astrophysics Series (Cambridge: Cambridge University Press), 419–456
Kirk, J. G. & Galloway, D. J. 1981, MNRAS, 195, 45P
Kirk, J. G. & Stoneham, R. J. 1982, MNRAS, 201, 1183
Koh, D. T., Bildsten, L., Chakrabarty, D., et al. 1997, ApJ, 479, 933
Kraft, R. P. 1962, ApJ, 135, 408
Kraus, U., Blum, S., Schulte, J., Ruder, H., & Mészáros, P. 1996, ApJ, 467, 794
Kretschmar, P. 1996, Dissertation, Fakultät für Physik der Eberhard-Karls-Universität Tübingen
Kretschmar, P., Araya, R., Kreykenbohm, I., et al. 2000, in Conf. Proc. of the 4th Integral Workshop ”The Gamma Ray Universe”, ed. A. Gimenez, V. Reglero, & C. Winkler, ESA SP-459, Alicante, 207–210
Kretschmar, P., Kreykenbohm, I., Wilms, J., et al. 1999, in Proc. 5th Compton Symposium, ed. M. McConnell & J. Ryan, AIP Conf. Proc. No. 510, 163
Kretschmar, P., Kreykenbohm, I., Wilms,

J., et al. 1997, in The Transparent Universe, Proc. 2nd INTEGRAL Workshop, ed. C. Winkler, T. J.-L. Courvoisier, & P. Durouchoux, ESA SP 382, Noordwijk, 141–144

Kretschmar, P., Pan, H. C., Kendziorra, E., et al. 1996, A&A

Kreykenbohm, I. 1997, Master's thesis, University of Tübingen, Tübingen

Kreykenbohm, I., Coburn, W., Wilms, J., et al. 2002a, A&A, 395, 129

—. 2002b, VizieR Online Data Catalog, 339, 50129

Kreykenbohm, I., Kretschmar, P., Wilms, J., et al. 2000, in Proc. Conf. X-ray Astronomy 99 - Stellar Endpoints, AGN and the Diffuse Background (Gordon & Breach)

Kreykenbohm, I., Kretschmar, P., Wilms, J., et al. 1999, A&A, 341, 141

Kreykenbohm, I., Wilms, J., Coburn, W., et al. 2004, A&A, submitted

Kundt, W. 2001, Astrophysics. A Primer. (Heidelberg: Springer)

Kunz, M. 1996, Dissertation, Fakultät für Physik der Eberhard-Karls-Universität Tübingen

Kuster, M. 2003, PhD thesis, University of Tübingen, Tübingen

La Barbera, A., Santangelo, A., Orlandini, M., & Segreto, A. 2003, A&A, 400, 993

Lai, D. 2001, Rev. Mod. Phys., 73, 629

Lamb, D. Q., Wang, J. C. L., & Wasserman, I. M. 1990, ApJ, 363, 670

Lamb, F. K., Pethick, C. J., & Pines, D. 1973, ApJ, 184, 271

Lamb, R. C., Markert, T. H., Hartman, R. C., Thompson, D. J., & Bignami, G. F. 1980, ApJ, 239, 651

Lamb, S. A., Iben, Jr., I., & Howard, W. M. 1976, ApJ, 207, 209

Lamers, H. J. G. L. M., can den Heuvel, P. J., & Petterson, J. A. 1976, A&A, 49, 327

Lang, K. R. 1999, Astrophysical Formulae Vol. 1 (Heidelberg: Springer)

Large, M. I., Vaughan, A. E., & Mills, B. Y. 1968, Nature, 220, 340

Latal, H. G. 1986, ApJ, 309, 372

Leahy, D. A. 1991, MNRAS, 250, 310

—. 2002, A&A, 391, 219

Leahy, D. A., Darbo, W., Elsner, R. F., et al. 1983, ApJ, 266, 160

Levine, A. M., Bradt, H., Cui, W., et al. 1996, ApJ, 469, L33

Lightman, A. P. & White, T. R. 1988, ApJ, 335, 57

Lindegren, L. 1992, in Proc. Satellite Symposium No. 3 Space Sciences with particular emphasis on High Energy Astrophysics, ESA SP-349

Lipunov, V. M. 1992, Astrophysics of Neutron Stars (Heidelberg: Springer)

Little, L. T. & Hewish, A. 1966, MNRAS, 134, 221

Litwin, C., Brown, E. F., & Rosner, R. 2001, ApJ, 553, 788

Lodenquai, J., Canuto, V., Ruderman, M., & Tsuruta, S. 1974, ApJ, 190, 141

Longair, M. S. 1997, High Energy Astrophysics Vol. 2 (Cambridge: Cambridge University Press)

Lund, N., Budtz-Jørgensen, C., Westergaard, N. J., et al. 2003, A&A, 411, L231

Lyne, A. G. & Graham-Smith, F. 1998, Pulsar Astronomy, Cambridge Astrophysics Series (Cambridge: Cambridge University Press)

Maeder, A. 1982, A&A, 105, 149

Magdziarz, P. & Zdziarski, A. A. 1995, MNRAS, 273, 837

Maisack, M., Grove, J. E., Kendziorra, E., et al. 1997, A&A, 325, 212

Makishima, K., Maejima, Y., Mitsuda, K., et al. 1986, ApJ, 308, 635

Makishima, K., Mihara, T., Nagase, F., & Murakami, T. 1992, in Frontiers of X-

Ray Astronomy, Proc, XXVIII Yamada Conf., ed. Y. Tanaka & K. Koyama, Frontiers Science Series, 2, 23–32

Makishima, K., Mihara, T., Nagase, F., & Tanaka, Y. 1999, ApJ, 525, 978

Makishima, K. & Ohashi, T. 1990, PASJ, 42, 239

Marano, B., Zamorani, G., & Zitelli, V. 1988, MNRAS, 232, 111

Mas-Hesse, J. M., Giménez, A., Culhane, J. L., et al. 2003, A&A, 411, L261

Mason, K. O., Bignami, G., Brinkman, A. C., & Peacock, A. 1995, Adv. Space Res., 16, 41

Matteo, T. D., Esin, A., Fabian, A. C., & narayan, R. 1998, MNRAS, in press

Matteson, J. L. 1978, in Conf. Proc. ”AIAA, Aerospace Sciences Meeting”

Mauder, H. 1973, A&A, 28, 473

McClintock, J. E., Rappaport, S., Joss, P. C., et al. 1976, ApJ, 206, L99

Mészáros, P. 1977, Nature

—. 1992, High-Energy Radiation from Magnetized Neutron Stars (Chicago: University of Chicago Press)

Mészáros, P. & Bonazzola, S. 1981, ApJ, 251, 695

Mészáros, P., Harding, A. K., Kirk, J. G., & Galloway, D. J. 1983, Astrophys. J., Lett., 266, L33

Mészáros, P. & Nagel, W. 1985, ApJ, 298, 147

Mihara, T. 1995, PhD thesis, RIKEN, Tokio

Mihara, T., Makishima, K., & Nagase, F. 1998, in AllSky Monitor Survey Conference, RIKEN, 135–140

Mihara, T., Makishima, K., Ohashi, T., Sakao, T., & Tashiro, M. 1990, Nature, 346, 250

Mihara, T., Ohashi, T., Makishima, K., et al. 1991, PASJ, 43, 501

Moran, E. C., Kay, L. E., Davis, M., Filippenko, A. V., & Barth, A. J. 2001, ApJ, 556, L75

Morris, S. L. 1994, PASP, 106, 154

Morton, D. C. 1964, ApJ, 140, 460

Motch, C. & Haberl, F. 1998, A&A, 333, L59

Mytrophanov, I. G. & Tsygan, A. I. 1978, A&A, 70, 133

Nagase, F. 1989, PASJ, 41, 1

Nagase, F., Hayakawa, S., Kii, T., et al. 1984, PASJ, 36, 667

Nagase, F., Hayakawa, S., Makino, F., Sato, N., & Makishima, K. 1983, PASJ, 35, 47

Nagase, F., Hayakawa, S., Sato, N., Masai, K., & Inoue, H. 1986, PASJ, 38, 547

Nagel, W. 1980, ApJ, 236, 904

—. 1981a, ApJ, 251, 278

—. 1981b, ApJ, 251, 288

Neugebauer, G., Habing, H. J., van Duinen, R., et al. 1984, Astrophys. J., Lett., 278, L1

Oda, M., Gorenstein, P., Gursky, H., et al. 1971, ApJ, 166, L1

Ohashi, T., Inoue, H., Koyama, K., et al. 1984, PASJ, 36, 699

Oosterbroek, T., Parmar, A. N., Orlandini, M., et al. 2001, A&A, preprint

Oppenheimer, J. R. & Volkoff, G. M. 1939, Phys. Rev., 55, 374

Orlandini, M., Dal Fiume, D., Frontera, F., et al. 1998a, A&A, 332, 121

—. 1998b, Astrophys. J., Lett., submitted

Orlandini, M., Dal Fiume, D., Nicastro, L., et al. 1997, in Fourth Compton Symposium, AIP

Orlandini, M., Dal Fiume, S., Del Sordo, S., et al. 1999, A&A, preprint

Ostriker, E. C., Stone, J. M., & Gammie, C. F. 2001, ApJ, 546, 980

Ostriker, J. P. & Gunn, J. E. 1969, ApJ, 157, 1395

Pacini, F. 1967, Nature, 216, 567

—. 1968, Nature, 219, 145

Paczyński, B. 1974, A&A, 34, 161

Paczyński, B. 1986, ApJ, 304, 1

Parkes, G. E., Mason, K. O., Murdin, P. G., & Culhane, J. L. 1980, MNRAS, 191, 547

Parmar, A. N., White, N. E., & Stella, L. 1989a, ApJ, 338, 373

Parmar, A. N., White, N. E., Stella, L., Izzo, C., & Ferri, P. 1989b, ApJ, 338, 359

Pavlov, G. G., Zavlin, V. E., Trümper, J., & Heuhäuser, R. 1996, ApJ, 472, L33

Payne-Gaposchkin, C. 1984, Sterne und Sternhaufen (Braundschweig, Wiesbaden: Vieweg)

Pelling, M. R., Rothschild, R. E., MacDonald, D. R., Hertel, R., & Nishiie, E. 1991, in EUV, X-ray, and gamma-ray instrumentation for astronomy II; Proceedings of the Meeting, San Diego, CA, July 24-26, 1991 (A93-34376 13-35), 134–146

Perryman, M. A. C., Hassan, H., Batut, T., et al. 1989, The HIPPARCOS mission – Pre-Launch Status Vol. I–III, Vol. SP-1111 (Paris: ESA)

Pethick, C. J. & Ravenhall, D. G. 1991a, Neutron Stars: Theory and Observation (Dortrecht-Holland: Kluwer)

—. 1991b, Neutron Stars: Theory and Observation (Dortrecht-Holland: Kluwer)

Porter, J. M. & Rivinius, T. 2003, PASP, 115, 1153

Pottschmidt, K. 2002, PhD thesis, University of Tübingen, Tübingen

Pravdo, S. H., Bussard, R. W., Becker, R. H., et al. 1978, ApJ, 225, 988

Pravdo, S. H., Day, C. S. R., Angelini, L., et al. 1995, ApJ, 454, 872

Pravdo, S. H. & Ghosh, P. 2001, ApJ, 554, 383

Priedhorsky, W. C. & Terrell, J. 1983, Nature, 303, 681

Pringle, J. E. & Rees, M. J. 1972, A&A, 21, 1

Proctor, R. J., Skinner, G. K., & Willmore, A. P. 1979, MNRAS, 187, 633

Protassov, R., van Dyk, D. A., Connors, A., Kashyap, V. L., & Siemiginowska, A. 2002, ApJ, 571, 545

Quaintrell, H., Norton, A. J., Ash, T. D. C., et al. 2003, A&A, 401, 313

Rappaport, S. & McClintock, J. E. 1975, IAU Circ., 2794

Raubenheimer, B. C. 1990, A&A, 234, 172

Remillard, R. & Marshall, F. 2003, The Astronomer’s Telegram, 197, 1

Roche, E. A. 1849a, Mem. Acad. Sci. Montpellier, 1, 243

—. 1849b, Mem. Acad. Sci. Montpellier, 2, 383

Rosenberg, H. 1911, Astron. Nachr., 186, 71

Rothschild, R. E., Blanco, P. R., Gruber, D. E., et al. 1998, ApJ, 496, 538

Rothschild, R. E. & Soong, Y. 1987, ApJ, 315, 154

Ruderman, M. A. & Sutherland, P. G. 1973, Nature Physical Science, 246, 93

Salpeter, E. E. 1964, ApJ, 140, 796

Sandage, A., Osmer, P., Giacconi, R., et al. 1966, ApJ, 146, 316

Sang, Y. & Chanmugam, G. 1987, ApJ, 363, 597

Santangelo, A., Del Sordo, S., Segreto, A., et al. 1998, A&A, 340, L55

Santangelo, A., Segreto, A., Giarrusso, S., et al. 1999, ApJ, L85

Sato, N., Nagase, F., Kawai, N., et al. 1986, ApJ, 304, 241

Schandl, S. & Meyer, F. 1994, A&A, 289, 149

Schatzman, E. L. & Praderie, F. 1993, The Stars, A&A Library (Heidelberg: Springer)

Scheffler, H. 1988, Interstellare Materie (Braunschweig, Wiesbaden: Vieweg)

Seidov, Z. F. 2003, ArXiv Astrophysics e-prints, astro-ph/0311272

Shakura, N. I. 1973, Soviet Astronomy, 16, 756

Shapiro, S. L. 1983, Black Holes, White Dwarfs and Neutron Stars (New York: Wiley Interscience)

Shapiro, S. L. & Salpeter, E. E. 1975, ApJ, 198, 671

Shepherd, D. S., Nürnberger, D. E. A., & Bronfman, L. 2003, ApJ, submitted

Skinner, G. K., Bedford, D. K., Elsner, R. F., et al. 1982, Nature, 297, 568

Skinner, G. K., Ponman, T. J., Hammersley, A. P., & Eyles, C. J. 1987, Ap&SS, 136, 337

Snowden, S. L. 1996, The South Atlantic Anomaly, `http://rosat.gsfc.nasa.gov/docs/rosat/gallery/misc_saad.html`

Soong, Y., Gruber, D. E., Peterson, L. E., & Rothschild, R. E. 1990, ApJ, 348, 641

Srinivasan, G. 1989, A&AR, 1, 209

—. 1997, in Stellar Remnants, ed. G. Meynet & D. Schaerer, Saas Fee Advanced Course (Heidelberg: Springer), 97–236

Srinivasan, G., Bhattacharya, D., Mulimov, A. G., & Tsygan, A. I. 1990, Current Science, 59, 31

Stailin, D. H. & Reifenstein, E. C. 1968, Science, 162, 1481

Stark. 1997, PCABackEst Information Homepage, `http://ww2.lafayette.edu/~starkm/pca/pcabackest.html`

Starrfield, S., Sparks, W. M., & Truran, J. W. 1985, ApJ, 291, 136

Staubert, R., Kendziorra, E., Pietsch, W., C. Reppin, J. T., & Voges, W. 1980, ApJ, 239, 1010

Stickland, D., Lloyd, C., & Radziun-Woodham, A. 1997, MNRAS, 286

Still, M., O’Brien, K., Horne, K., et al. 2001, ApJ, in press

Sturner, S. J. & Dermer, C. D. 1994, A&A, 284, 161

Sunyaev, R. A., Grebenev, S. A., Lutovinov, A. A., et al. 2003, The Astronomer’s Telegram, 190, 1

Sunyaev, R. A. & Titarchuk, L. G. 1980, A&A, 86, 121

Swank, J. H., Becker, R. H., Boldt, E. A., et al. 1976, ApJ, 209, L57

Taam, R. E. & Fryxell, B. A. 1988, ApJ, 327, L73

Tanaka, Y. 1986, in Radiation Hydrodynamics in Stars and Compact Objects, ed. D. Mihalas & K.-H. A. Winkler, IAU Coll. 89 (Heidelberg: Springer), 198

Tananbaum, H., Gursky, H., Kellogg, E. M., et al. 1972, ApJ, 174, L143

Terrell, N. J. J. 1972, Astrophys. J., Lett., 174, L35

Tjemkes, S. A., Zuiderwijk, E. J., & van Paradijs, J. 1986, A&A, 154, 77

Trümper, J., Pietsch, W., Reppin, C., et al. 1977, in Conf. Proc. "8th Texas symposium on Relativistic Astrophysics"(Boston: Ann. NY Acad. Sci.)

Trümper, J., Pietsch, W., Reppin, C., W. Voges, R. S., & Kendziorra, E. 1978, ApJ, 219, L105

Tsunemi, H. 1989, PASJ, 42, 453

Ubertini, P., Lebrun, F., Di Cocco, G., et al. 2003, A&A, 411, L131

Unsöld, A. & Baschek, B. 1991, Der neue Kosmos (Heidelberg: Springer)

Urpin, V. & Geppert, U. 1995, MNRAS, 275, 1117

van Allen, J. A. 1958, Radiation belts around the earth (San Francisco: Freeman, 1958)

van Allen, J. A., McIlwain, C. E., & Ludwig, G. H. 1959, J. Geophys. Res., 64, 271

van den Heuvel, E. P. J. & Habets, G. M. H. J. 1984, Nature, 309 van Kerkwijk, M. H., van Paradijs, J., Zuiderwijk, E. J., et al. 1995, A&A, 303, 483

van Paradijs, J. & McClintock, J. E. 1995, in X-Ray Binaries, ed. W. H. G. Lewin, J. van Paradijs, & E. P. J. van den Heuvel (Cambridge: Cambridge University Press), 58–125

van Paradijs, J., Zuiderwijk, E. J., Takens, R. J., et al. 1977, A&AS, 30, 195

Vedrenne, G., Roques, J.-P., Schönfelder, V., et al. 2003, A&A, 411, L63

Verbunt, F. & van den Heuvel, E. P. J. 1995, in X-Ray Binaries, ed. W. H. G. Lewin, J. van Paradijs, & E. P. J. van den Heuvel (Cambridge: Cambridge University Press), 457–494

Voges, W., Pietsch, W., Reppin, C., et al. 1982, ApJ, 263, 803

Voigt, H. H. 1991, Abriss der Astronomie (Mannheim: BI Wissenschaftsverlag)

Walter, R., Rodriguez, J., Foschini, L., et al. 2003, A&A, 411, L427

Wang, J. C. L., Wasserman, I., & Lamb, D. Q. 1993, ApJ, 414, 815

Wang, J. C. L., Wasserman, I. M., & Salpeter, E. E. 1989, ApJ, 338, 343

Wang, Y.-M. & Frank, J. 1981, A&A, 93, 255

Weidemann, V., Jordan, S., Iben, I. J., & Casertano, S. 1992, AJ, 104, 1876

Weizsäcker, C. F. 1937, Phys. Z., 38, 176

—. 1938, Phys. Z., 39, 633

Wheaton, W. A., Doty, J. P., Primini, F. A., et al. 1979, Nat, 282, 240

White, N. E. 1989, A&AR, 1, 85

White, N. E., Mason, K. O., Huckle, H. E., Charles, P. A., & Sanford, P. W. 1976a, ApJ, 209, L119

White, N. E., Mason, K. O., Sanford, P. W., & Murdin, P. 1976b, MNRAS, 176, 201

White, N. E., Parkes, G. E., & Sanford, P. W. 1978, Nat, 274, 664

White, N. E., Pravdo, S. H., Becker, R. H., et al. 1980, ApJ, 239, 655

White, N. E., Swank, J. H., & Holt, S. S. 1983, ApJ, 270, 711

Willingale, R., Aschenbach, B., Griffiths, R. G., et al. 2001, A&A, 365, L212

Willmore, A. P., Bertram, D., Watt, M. P., et al. 1992, MNRAS, 258, 621

Wilms, J. 1998, PhD thesis, Eberhard-Karls Universtät Tübingen

Wilms, J., Allen, A., & McCray, R. 2000, ApJ, 542, 914

Wilms, J., Nowak, M. A., Dove, J. B., Fender, R. P., & Di Matteo, T. 1999, ApJ, 522, 460

Wilson, R. B., Harmon, B. A., Fishman, G. J., & Finger, M. H. 1994, in International Astronomical Union Circular, 2

Winkler, C., Courvoisier, T. J.-L., Di Cocco, G., et al. 2003, A&A, 411, L1

Woltjer, L. 1964, ApJ, 140, 1309

Woosley, S. E., Heger, A., & Weaver, T. A. 2002, Reviews of Modern Physics, 74, 1015

Woosley, S. E. & Weaver, T. A. 1986, ARA&A, 24, 205

XTE-Staff. 1995, Appendix F: The XTE Technical Appendix

Yahel, R. Z. 1979, ApJ, 229, L73

Zel'dovich, Y. B. 1964, Sov. Phys. – Dokl., 9, 195

Zel'dovich, Y. B. & Shakura, N. I. 1969, SvA, 13, 175

Zuiderwijk, E. J., van den Heuvel, E. P. J., & Hensberge, G. 1974, A&A, 35, 353

APPENDIX A

Fit results for Vela X-1

This appendix contains tables for all fit results from the 1998 and 2000 observation of Vela X-1. All uncertainties are on a 90% confidence level. The model in use is the Negative Positive EXponential (NPEX) model (with Γ_2 always fixed to -2 Mihara 1995), modified by photoelectric absorption, an additive iron line at ~6.4keV, and none, one, or two cyclotron resonant scattering features at ~25 keV and ~50keV. For a description of the individual parameters, see Chapter 5, Section 5.3.1. The data presented here is also available in electronic form from the CDS (Kreykenbohm et al. 2002b).

A.1 The 1998 data

For the 1998 data, six phase bins were used: rise and fall of the main pulse, rise and fall of the secondary pulse, and the two pulse minima (see Fig. 5.13).

Rise of the main pulse

Paramter	w/o CRSF	1 CRSF	2 CRSFs
Fe [keV]	$1.9^{+0.3}_{-1.0}$	$1.4^{+0.5}_{-0.9}$	$2.4^{+0.2}_{-1.3}$
σ_{Fe} [keV]	$6.32^{+0.05}_{-0.05}$	$6.28^{+0.07}_{-0.05}$	$6.33^{+0.05}_{-0.06}$
Γ_1	$0.27^{+0.07}_{-0.10}$	$0.29^{+0.07}_{-0.08}$	$0.29^{+0.07}_{-0.08}$
Γ_2	$0.54^{+0.06}_{-0.06}$	$0.51^{+0.06}_{-0.07}$	$0.68^{+0.09}_{-0.12}$
E_{F}	2	2	2
E_{Cut}	$5.94^{+0.04}_{-0.04}$	$6.07^{+0.06}_{-0.06}$	$6.54^{+1.13}_{-0.58}$
$E_{\mathrm{C,1}}$ [keV]	—	—	$25.9^{+2.5}_{-1.6}$
$\sigma_{\mathrm{C,1}}$ [keV]	—	—	$7.6^{+4.4}_{-2.2}$
$\tau_{\mathrm{C,1}}$	—	—	$0.33^{+0.06}_{-0.13}$
$E_{\mathrm{C,2}}$ [keV]	—	$50.5^{+1.9}_{-1.3}$	$52.8^{+6.0}_{-3.1}$
$\sigma_{\mathrm{C,2}}$ [keV]	—	$2.3^{+1.8}_{-1.7}$	$9.0^{+6.3}_{-5.9}$
$\tau_{\mathrm{C,2}}$	—	$1.1^{+0.4}_{-0.3}$	$1.1^{+0.8}_{-0.7}$
χ^2	136	84	41
DOF	64	61	58

Fall of the main pulse

Paramter	w/o CRSF	1 CRSF	2 CRSFs
Fe [keV]	$1.9^{+0.5}_{-0.9}$	$1.8^{+0.3}_{-1.3}$	$2.9^{+0.4}_{-1.2}$
σ_{Fe} [keV]	$6.25^{+0.08}_{-0.05}$	$6.22^{+0.11}_{-0.05}$	$6.31^{+0.05}_{-0.07}$
Γ_1	$0.28^{+0.08}_{-0.09}$	$0.31^{+0.08}_{-0.08}$	$0.31^{+0.09}_{-0.08}$
Γ_2	$0.36^{+0.06}_{-0.07}$	$0.29^{+0.07}_{-0.07}$	$0.58^{+0.10}_{-0.11}$
E_{F}	2	2	2
E_{Cut}	$6.14^{+0.03}_{-0.03}$	$6.28^{+0.04}_{-0.04}$	$6.02^{+0.17}_{-0.05}$
$E_{\mathrm{C,1}}$ [keV]	—	—	$23.3^{+1.3}_{-0.6}$
$\sigma_{\mathrm{C,1}}$ [keV]	—	—	$4.9^{+1.9}_{-0.8}$
$\tau_{\mathrm{C,1}}$	—	—	$0.15^{+0.07}_{-0.02}$
$E_{\mathrm{C,2}}$ [keV]	—	$53.8^{+2.3}_{-1.9}$	$54.5^{+5.0}_{-2.8}$
$\sigma_{\mathrm{C,2}}$ [keV]	—	$3.7^{+1.6}_{-1.6}$	$5.3^{+5.1}_{-2.8}$
$\tau_{\mathrm{C,2}}$	—	$0.8^{+0.5}_{-0.2}$	$0.5^{+0.3}_{-0.1}$
χ^2	258	174	61
DOF	64	61	58

Pulse minimum 1

Paramter	w/o CRSF	1 CRSF	2 CRSFs
Fe [keV]	$2.4^{+0.5}_{-0.8}$	$2.5^{+0.4}_{-1.8}$	$2.4^{+0.9}_{-0.6}$
σ_{Fe} [keV]	$6.32^{+0.03}_{-0.07}$	$6.26^{+0.07}_{-0.05}$	$6.34^{+0.04}_{-0.07}$
Γ_1	$0.30^{+0.06}_{-0.08}$	$0.33^{+0.06}_{-0.06}$	$0.35^{+0.06}_{-0.06}$
Γ_2	$0.72^{+0.04}_{-0.07}$	$0.61^{+0.06}_{-0.06}$	$0.81^{+0.12}_{-0.08}$
E_{F}	2	2	2
E_{Cut}	$6.36^{+0.03}_{-0.03}$	$6.38^{+0.09}_{-0.06}$	$6.37^{+0.08}_{-0.07}$
$E_{\mathrm{C},1}$ [keV]	—	—	$21.1^{+0.7}_{-0.7}$
$\sigma_{\mathrm{C},1}$ [keV]	—	—	$4.1^{+1.6}_{-0.7}$
$\tau_{\mathrm{C},1}$	—	—	$0.13^{+0.05}_{-0.02}$
$E_{\mathrm{C},2}$ [keV]	—	$53.0^{+1.6}_{-1.2}$	$52.8^{+1.9}_{-1.4}$
$\sigma_{\mathrm{C},2}$ [keV]	—	$4.9^{+1.2}_{-0.9}$	$4.7^{+1.5}_{-1.2}$
$\tau_{\mathrm{C},2}$	—	$1.3^{+0.3}_{-0.2}$	$1.1^{+0.3}_{-0.2}$
χ^2	424	144	62
DOF	64	61	58

Rise of the secondary pulse

Paramter	w/o CRSF	1 CRSF	2 CRSFs
Fe [keV]	$3.2^{+0.8}_{-0.5}$	$3.2^{+0.4}_{-0.9}$	$2.9^{+0.1}_{-1.4}$
σ_{Fe} [keV]	$6.34^{+0.03}_{-0.02}$	$6.34^{+0.02}_{-0.06}$	$6.31^{+0.04}_{-0.04}$
Γ_1	$0.26^{+0.33}_{-0.21}$	$0.30^{+0.05}_{-0.06}$	$0.20^{+0.05}_{-0.06}$
Γ_2	$0.65^{+0.06}_{-0.06}$	$0.60^{+0.06}_{-0.06}$	$0.66^{+0.07}_{-0.10}$
E_{F}	2	2	2
E_{Cut}	$6.34^{+0.07}_{-0.07}$	$6.09^{+0.15}_{-0.11}$	$5.93^{+0.16}_{-0.13}$
$E_{\mathrm{C},1}$ [keV]	—	—	$20.2^{+4.0}_{-1.6}$
$\sigma_{\mathrm{C},1}$ [keV]	—	—	$2.2^{+1.3}_{-0.9}$
$\tau_{\mathrm{C},1}$	—	—	$0.07^{+0.04}_{-0.03}$
$E_{\mathrm{C},2}$ [keV]	—	$43.8^{+2.2}_{-1.8}$	$43.1^{+1.8}_{-1.5}$
$\sigma_{\mathrm{C},2}$ [keV]	—	$3.3^{+2.3}_{-1.7}$	$2.5^{+2.8}_{-1.9}$
$\tau_{\mathrm{C},2}$	—	$0.4^{+0.4}_{-0.2}$	$0.43^{+0.1}_{-0.1}$
χ^2	96	73	59
DOF	64	61	58

Fall of the secondary pulse

Paramter	w/o CRSF	1 CRSF	2 CRSFs
Fe [keV]	$3.4^{+0.4}_{-1.2}$	$2.9^{+0.6}_{-1.0}$	$3.3^{+0.6}_{-1.2}$
σ_{Fe} [keV]	$6.30^{+0.07}_{-0.06}$	$6.28^{+0.06}_{-0.04}$	$6.30^{+0.05}_{-0.05}$
Γ_1	$0.34^{+0.06}_{-0.07}$	$0.35^{+0.06}_{-0.06}$	$0.35^{+0.06}_{-0.06}$
Γ_2	$0.32^{+0.07}_{-0.07}$	$0.28^{+0.07}_{-0.08}$	$0.34^{+0.14}_{-0.12}$
E_{F}	2	2	2
E_{Cut}	$5.83^{+0.07}_{-0.07}$	$6.03^{+0.14}_{-0.11}$	$5.89^{+0.22}_{-0.22}$
$E_{\mathrm{C,1}}$ [keV]	—	—	$20.3^{+11.3}_{-5.8}$
$\sigma_{\mathrm{C,1}}$ [keV]	—	—	$3.9^{+\infty}_{-3.8}$
$\tau_{\mathrm{C,1}}$	—	—	$0.03^{+0.67}_{-0.03}$
$E_{\mathrm{C,2}}$ [keV]	—	$49.5^{+5.4}_{-3.4}$	$49.3^{+7.3}_{-5.0}$
$\sigma_{\mathrm{C,2}}$ [keV]	—	$3.9^{+3.8}_{-3.0}$	$3.9^{+4.7}_{-1.9}$
$\tau_{\mathrm{C,2}}$	—	$0.6^{+2.7}_{-0.3}$	$0.5^{+0.3}_{-0.3}$
χ^2	82	57	53
DOF	64	61	58

Pulse minimum 2

Paramter	w/o CRSF	1 CRSF	2 CRSFs
Fe [keV]	$4.2^{+0.6}_{-1.1}$	$4.4^{+0.1}_{-1.7}$	$4.4^{+0.4}_{-1.2}$
σ_{Fe} [keV]	$6.32^{+0.04}_{-0.05}$	$6.30^{+0.05}_{-0.05}$	$6.33^{+0.04}_{-0.06}$
Γ_1	$0.35^{+0.06}_{-0.06}$	$0.34^{+0.06}_{-0.06}$	$0.36^{+0.06}_{-0.06}$
Γ_2	$0.69^{+0.07}_{-0.08}$	$0.61^{+0.07}_{-0.08}$	$0.75^{+0.15}_{-0.14}$
E_{F}	2	2	2
E_{Cut}	$5.68^{+0.04}_{-0.03}$	$5.83^{+0.04}_{-0.04}$	$5.81^{+0.38}_{-0.09}$
$E_{\mathrm{C,1}}$ [keV]	—	—	$24.4^{+4.1}_{-2.1}$
$\sigma_{\mathrm{C,1}}$ [keV]	—	—	$6.2^{+4.9}_{-2.5}$
$\tau_{\mathrm{C,1}}$	—	—	$0.09^{+0.04}_{-0.03}$
$E_{\mathrm{C,2}}$ [keV]	—	$50.4^{+3.0}_{-2.0}$	$51.2^{+5.2}_{-2.5}$
$\sigma_{\mathrm{C,2}}$ [keV]	—	$3.3^{+1.9}_{-1.7}$	$5.0^{+4.3}_{-2.2}$
$\tau_{\mathrm{C,2}}$	—	$1.0^{+1.2}_{-0.3}$	$0.8^{+0.3}_{-0.2}$
χ^2	136	64	45
DOF	64	61	58

A.2 The 2000 data

For the 2000 data, nine phase bins were used: rise, center, and fall of the main pulse, rise part 1, rise part 2, center, and fall of the secondary pulse, and the two pulse minima (see Fig 5.7).

Rise of the main pulse

Paramter	w/o CRSF	1 CRSF	2 CRSFs
Fe [keV]	$4.2^{+0.4}_{-1.2}$	$4.4^{+0.3}_{-1.9}$	$4.1^{+0.1}_{-1.5}$
σ_{Fe} [keV]	$6.36^{+0.02}_{-0.07}$	$6.32^{+0.05}_{-0.05}$	$6.35^{+0.04}_{-0.05}$
Γ_1	$0.35^{+0.06}_{-0.06}$	$0.34^{+0.07}_{-0.06}$	$0.36^{+0.06}_{-0.06}$
Γ_2	$0.80^{+0.03}_{-0.10}$	$0.67^{+0.06}_{-0.08}$	$0.81^{+0.03}_{-0.11}$
E_{F}	2	2	2
E_{Cut}	$5.94^{+0.03}_{-0.02}$	$6.15^{+0.04}_{-0.03}$	$6.12^{+0.03}_{-0.03}$
$E_{\mathrm{C,1}}$ [keV]	—	—	$23.2^{+1.1}_{-0.8}$
$\sigma_{\mathrm{C,1}}$ [keV]	—	—	$4.5^{+1.1}_{-0.3}$
$\tau_{\mathrm{C,1}}$	—	—	$0.10^{+0.02}_{-0.02}$
$E_{\mathrm{C,2}}$ [keV]	—	$53.0^{+2.5}_{-1.9}$	$54.8^{+2.9}_{-2.8}$
$\sigma_{\mathrm{C,2}}$ [keV]	—	$5.5^{+1.5}_{-1.3}$	$8.6^{+1.7}_{-2.0}$
$\tau_{\mathrm{C,2}}$	—	$0.7^{+0.2}_{-0.1}$	$0.7^{+0.1}_{-0.2}$
χ^2	208	84	41
DOF	64	61	58

Center of the main pulse

Paramter	w/o CRSF	1 CRSF	2 CRSFs
Fe [keV]	$4.2^{+0.5}_{-0.9}$	$4.2^{+0.2}_{-1.3}$	$4.2^{+0.6}_{-0.8}$
σ_{Fe} [keV]	$6.33^{+0.04}_{-0.06}$	$6.31^{+0.04}_{-0.05}$	$6.33^{+0.04}_{-0.05}$
Γ_1	$0.33^{+0.06}_{-0.06}$	$0.33^{+0.06}_{-0.05}$	$0.35^{+0.06}_{-0.06}$
Γ_2	$1.04^{+0.04}_{-0.08}$	$0.98^{+0.06}_{-0.07}$	$1.07^{+0.06}_{-0.08}$
E_{F}	2	2	2
E_{Cut}	$5.95^{+0.04}_{-0.03}$	$6.14^{+0.09}_{-0.06}$	$6.04^{+0.08}_{-0.07}$
$E_{\mathrm{C,1}}$ [keV]	—	—	$20.1^{+1.3}_{-1.6}$
$\sigma_{\mathrm{C,1}}$ [keV]	—	—	$2.8^{+1.4}_{-0.9}$
$\tau_{\mathrm{C,1}}$	—	—	$0.06^{+0.03}_{-0.02}$
$E_{\mathrm{C,2}}$ [keV]	—	$50.5^{+3.9}_{-2.4}$	$50.6^{+4.9}_{-2.7}$
$\sigma_{\mathrm{C,2}}$ [keV]	—	$4.9^{+2.6}_{-2.5}$	$5.4^{+3.4}_{-2.4}$
$\tau_{\mathrm{C,2}}$	—	$0.6^{+0.4}_{-0.2}$	$0.5^{+0.2}_{-0.2}$
χ^2	121	75	50
DOF	64	61	58

Fall of the main pulse

Paramter	w/o CRSF	1 CRSF	2 CRSFs
Fe [keV]	$3.9^{+0.6}_{-0.8}$	$3.7^{+0.6}_{-0.8}$	$3.3^{+0.3}_{-1.4}$
σ_{Fe} [keV]	$6.40^{+0.03}_{-0.14}$	$6.40^{+0.03}_{-0.08}$	$6.34^{+0.04}_{-0.05}$
Γ_1	$0.0^{+0.28}_{-0.0}$	$0.26^{+0.05}_{-0.08}$	$0.28^{+0.06}_{-0.06}$
Γ_2	$0.52^{+0.06}_{-0.06}$	$0.47^{+0.06}_{-0.07}$	$0.51^{+0.12}_{-0.07}$
E_{F}	2	2	2
E_{Cut}	$5.86^{+0.10}_{-0.09}$	$5.96^{+0.14}_{-0.12}$	$6.02^{+0.13}_{-0.05}$
$E_{\mathrm{C},1}$ [keV]	—	—	$23.0^{+1.2}_{-2.1}$
$\sigma_{\mathrm{C},1}$ [keV]	—	—	$4.8^{+5.5}_{-1.3}$
$\tau_{\mathrm{C},1}$	—	—	$0.09^{+0.04}_{-0.04}$
$E_{\mathrm{C},2}$ [keV]	—	$45.6^{+3.6}_{-9.5}$	$44.5^{+2.7}_{-2.9}$
$\sigma_{\mathrm{C},2}$ [keV]	—	$4.3^{+2.8}_{-3.9}$	$6.8^{+3.0}_{-2.0}$
$\tau_{\mathrm{C},2}$	—	$0.2^{+0.1}_{-0.2}$	$0.3^{+0.1}_{-0.2}$
χ^2	96	92	70
DOF	64	61	58

Pulse minimum 1

Paramter	w/o CRSF	1 CRSF	2 CRSFs
Fe [keV]	$26.8^{+1.8}_{-1.6}$	$27.1^{+0.6}_{-3.1}$	$25.1^{+2.7}_{-5.6}$
σ_{Fe} [keV]	$6.36^{+0.01}_{-0.01}$	$6.36^{+0.01}_{-0.01}$	$6.34^{+0.02}_{-0.01}$
Γ_1	$0.33^{+0.02}_{-0.02}$	$0.34^{+0.02}_{-0.02}$	$0.37^{+0.02}_{-0.02}$
Γ_2	$2.35^{+0.07}_{-0.07}$	$2.35^{+0.08}_{-0.07}$	$2.43^{+0.07}_{-0.12}$
E_{F}	2	2	2
E_{Cut}	$5.41^{+0.01}_{-0.02}$	$5.47^{+0.01}_{-0.02}$	$5.99^{+0.02}_{-0.02}$
$E_{\mathrm{C},1}$ [keV]	—	—	$25.2^{+1.4}_{-0.8}$
$\sigma_{\mathrm{C},1}$ [keV]	—	—	$5.3^{+1.0}_{-0.8}$
$\tau_{\mathrm{C},1}$	—	—	$0.18^{+0.05}_{-0.04}$
$E_{\mathrm{C},2}$ [keV]	—	$49.9^{+2.9}_{-2.4}$	$53.5^{+4.0}_{-2.4}$
$\sigma_{\mathrm{C},2}$ [keV]	—	$3.7^{+2.1}_{-3.2}$	$12.3^{+3.3}_{-2.3}$
$\tau_{\mathrm{C},2}$	—	$0.4^{+1.9}_{-0.2}$	$0.9^{+0.1}_{-0.1}$
χ^2	141	99	46
DOF	61	58	55

Rise of the secondary pulse, part 1

Paramter	w/o CRSF	1 CRSF	2 CRSFs
Fe [keV]	$23.4^{+1.2}_{-1.4}$	$22.3^{+0.8}_{-1.8}$	$22.0^{+2.2}_{-0.9}$
σ_{Fe} [keV]	$6.35^{+0.02}_{-0.02}$	$6.34^{+0.02}_{-0.01}$	$6.35^{+0.01}_{-0.01}$
Γ_1	$0.32^{+0.02}_{-0.02}$	$0.33^{+0.02}_{-0.02}$	$0.33^{+0.02}_{-0.02}$
Γ_2	$2.31^{+0.08}_{-0.08}$	$2.37^{+0.10}_{-0.08}$	$2.34^{+0.10}_{-0.08}$
E_{F}	2	2	2
E_{Cut}	$5.93^{+0.01}_{-0.01}$	$6.04^{+0.02}_{-0.02}$	$6.01^{+0.01}_{-0.01}$
$E_{\mathrm{C,1}}$ [keV]	—	—	$23.4^{+1.3}_{-1.2}$
$\sigma_{\mathrm{C,1}}$ [keV]	—	—	$3.4^{+1.7}_{-3.1}$
$\tau_{\mathrm{C,1}}$	—	—	$0.06^{+0.02}_{-0.02}$
$E_{\mathrm{C,2}}$ [keV]	—	$52.7^{+1.5}_{-1.2}$	$52.7^{+1.8}_{-1.3}$
$\sigma_{\mathrm{C,2}}$ [keV]	—	$3.3^{+1.3}_{-1.3}$	$3.9^{+1.7}_{-1.5}$
$\tau_{\mathrm{C,2}}$	—	$0.9^{+0.8}_{-0.3}$	$0.8^{+0.5}_{-0.2}$
χ^2	226	96	73
DOF	61	58	55

Rise of the secondary pulse, part 2

Paramter	w/o CRSF	1 CRSF	2 CRSFs
Fe [keV]	$17.5^{+1.0}_{-0.3}$	$15.8^{+1.9}_{-0.6}$	$20.1^{+0.7}_{-2.6}$
σ_{Fe} [keV]	$6.35^{+0.02}_{-0.01}$	$6.34^{+0.01}_{-0.01}$	$6.35^{+0.02}_{-0.01}$
Γ_1	$0.37^{+0.02}_{-0.03}$	$0.37^{+0.02}_{-0.02}$	$0.36^{+0.02}_{-0.02}$
Γ_2	$2.68^{+0.03}_{-0.15}$	$2.71^{+0.03}_{-0.13}$	$2.49^{+0.01}_{-0.13}$
E_{F}	2	2	2
E_{Cut}	$5.56^{+0.02}_{-0.02}$	$5.63^{+0.02}_{-0.02}$	$5.59^{+0.02}_{-0.02}$
$E_{\mathrm{C,1}}$ [keV]	—	—	$21.6^{+1.2}_{-1.0}$
$\sigma_{\mathrm{C,1}}$ [keV]	—	—	$2.8^{+1.3}_{-2.6}$
$\tau_{\mathrm{C,1}}$	—	—	$0.05^{+0.02}_{-0.03}$
$E_{\mathrm{C,2}}$ [keV]	—	$49.9^{+1.7}_{-1.6}$	$49.6^{+3.4}_{-2.0}$
$\sigma_{\mathrm{C,2}}$ [keV]	—	$3.1^{+1.6}_{-1.2}$	$2.9^{+3.0}_{-2.3}$
$\tau_{\mathrm{C,2}}$	—	$0.6^{+0.3}_{-0.2}$	$0.6^{+1.2}_{-0.3}$
χ^2	109	73	63
DOF	61	58	55

Center of the secondary pulse

Paramter	w/o CRSF	1 CRSF	2 CRSFs
Fe [keV]	$27.6^{+2.7}_{-4.9}$	$25.3^{+2.1}_{-4.5}$	$23.9^{+5.5}_{-7.7}$
σ_{Fe} [keV]	$6.37^{+0.02}_{-0.02}$	$6.37^{+0.01}_{-0.01}$	$6.35^{+0.02}_{-0.01}$
Γ_1	$0.34^{+0.02}_{-0.02}$	$0.35^{+0.02}_{-0.03}$	$0.38^{+0.02}_{-0.02}$
Γ_2	$2.35^{+0.04}_{-0.05}$	$2.43^{+0.06}_{-0.08}$	$2.63^{+0.04}_{-0.08}$
E_{F}	2	2	2
E_{Cut}	$5.77^{+0.02}_{-0.02}$	$5.90^{+0.02}_{-0.02}$	$6.33^{+0.02}_{-0.02}$
$E_{\mathrm{C,1}}$ [keV]	—	—	$28.8^{+1.4}_{-1.1}$
$\sigma_{\mathrm{C,1}}$ [keV]	—	—	$6.7^{+0.9}_{-0.8}$
$\tau_{\mathrm{C,1}}$	—	—	$0.15^{+0.02}_{-0.02}$
$E_{\mathrm{C,2}}$ [keV]	—	$51.7^{+2.9}_{-2.1}$	$54.2^{+1.6}_{-1.6}$
$\sigma_{\mathrm{C,2}}$ [keV]	—	$5.2^{+2.2}_{-1.3}$	$9.7^{+0.7}_{-1.1}$
$\tau_{\mathrm{C,2}}$	—	$0.5^{+0.2}_{-0.1}$	$0.9^{+0.1}_{-0.1}$
χ^2	175	85	65
DOF	61	58	55

Fall of the secondary pulse

Paramter	w/o CRSF	1 CRSF	2 CRSFs
Fe [keV]	$29.6^{+1.3}_{-3.1}$	$25.8^{+2.4}_{-5.0}$	$25.3^{+4.4}_{-7.3}$
σ_{Fe} [keV]	$6.39^{+0.01}_{-0.01}$	$6.36^{+0.02}_{-0.01}$	$6.34^{+0.02}_{-0.01}$
Γ_1	$0.34^{+0.01}_{-0.04}$	$0.39^{+0.02}_{-0.02}$	$0.41^{+0.02}_{-0.02}$
Γ_2	$2.19^{+0.05}_{-0.05}$	$2.35^{+0.03}_{-0.12}$	$2.81^{+0.01}_{-0.14}$
E_{F}	2	2	2
E_{Cut}	$5.81^{+0.01}_{-0.01}$	$5.95^{+0.02}_{-0.03}$	$6.83^{+0.03}_{-0.02}$
$E_{\mathrm{C,1}}$ [keV]	—	—	$26.6^{+2.3}_{-1.1}$
$\sigma_{\mathrm{C,1}}$ [keV]	—	—	$4.5^{+1.6}_{-1.8}$
$\tau_{\mathrm{C,1}}$	—	—	$0.07^{+0.02}_{-0.01}$
$E_{\mathrm{C,2}}$ [keV]	—	$51.0^{+11.2}_{-9.9}$	$56.2^{+3.8}_{-1.8}$
$\sigma_{\mathrm{C,2}}$ [keV]	—	$5.8^{+0.4}_{-0.4}$	$15.2^{+0.5}_{-1.0}$
$\tau_{\mathrm{C,2}}$	—	$0.5^{+0.7}_{-0.2}$	$1.1^{+0.2}_{-0.1}$
χ^2	303	156	96
DOF	61	58	55

Pulse minimum 2

Paramter	w/o CRSF	1 CRSF	2 CRSFs
Fe [keV]	$19.2^{+0.1}_{-2.5}$	$18.4^{+1.5}_{-3.6}$	$16.6^{+0.3}_{-1.5}$
σ_{Fe} [keV]	$6.35^{+0.02}_{-0.01}$	$6.34^{+0.02}_{-0.01}$	$6.34^{+0.01}_{-0.01}$
Γ_1	$0.39^{+0.02}_{-0.02}$	$0.40^{+0.02}_{-0.02}$	$0.41^{+0.02}_{-0.02}$
Γ_2	$2.38^{+0.04}_{-0.05}$	$2.53^{+0.04}_{-0.11}$	$2.62^{+0.02}_{-0.12}$
E_{F}	2	2	2
E_{Cut}	$5.38^{+0.02}_{-0.01}$	$5.50^{+0.02}_{-0.02}$	$5.61^{+0.02}_{-0.01}$
$E_{\mathrm{C,1}}$ [keV]	—	—	$23.2^{+4.3}_{-1.7}$
$\sigma_{\mathrm{C,1}}$ [keV]	—	—	$0.3^{+5.1}_{-0.3}$
$\tau_{\mathrm{C,1}}$	—	—	$0.04^{+\infty}_{-0.04}$
$E_{\mathrm{C,2}}$ [keV]	—	$62.8^{+14.6}_{-10.2}$	$60.1^{+\infty}_{-\infty}$
$\sigma_{\mathrm{C,2}}$ [keV]	—	$10.7^{+2.6}_{-5.4}$	$9.5^{+1.2}_{-2.6}$
$\tau_{\mathrm{C,2}}$	—	$0.6^{+0.9}_{-0.1}$	$0.8^{+0.5}_{-0.4}$
χ^2	99	73	71
DOF	61	58	55

Acknowledgments

Many people have helped me in some way or another during my PhD years and the writing of this thesis.

Most of all, however, I would like to thank my advisor Prof. R. Staubert for offering me the possibility to write a thesis in his group in the first place. I am very grateful for his continued support throughout the whole time and I would like to thank him very much for the help he provided.

Dr. Jörn Wilms, Prof. Stauberts assistant and now himself a lecturer at the University of Warwick, introduced me to astronomical research already during my Diploma thesis and together we ventured around (or through) the many pitfalls of research. I thank him very much for the many things I learned from him during the $\sim$6 years we spent together at the IAAT – not only in Astronomy, but also in UNIX system administration, LaTeX, science fiction, and many more subjects! Furthermore Jörn Wilms started many projects from which I could benefit including visits at the University of California, La Jolla, the University of Alicante, and a fascinating observing run at the ESO 1.5 m telescope at La Silla, Chile.

Very important for me and my work were my three visits at the Center for Astrophysics and Space Sciences (CASS) at the University of California, San Diego in La Jolla, where I enjoyed the hospitality of Rick Rothschild and his group, namely William "Biff" Heindl, Wayne Coburn, Duane Gruber, and others. Biff and Wayne not only helped me with my research, but also showed me some of the many beauties of California. A second equally very important collaboration developed with Jose Miguel Torrejon from the University of Alicante. He made my four visits there not only productive from the scientific point of view, but also very enjoyable.

Many thanks also to Markus Kuster and Peter Kretschmar for the interesting, merry, and extensive discussions about various subjects in and outside astronomy (often while having a tea).

As always, special thanks go to the "Espressorunde" for many funny and/or interesting discussions during lunch break and also to all other members of the IAAT for creating a fantastic atmosphere and making the institute one of the best places to work at.

Furthermore I would like to thank my various office mates I had during my time at the IAAT (Jörn Wilms, Beate Stelzer, Heiko Egeler, Robert Weiss, and Kolja Giedke) as well as my office neighbors (Katja Pottschmidt, Sara Benlloch, and Heinz Lenhart) for being good companions and making my stay in Tübingen enjoyable.

I would also like to thank the following institutions which either alleviated my work, supported me, or made this thesis possible in the first place: the DLR for

my part time position at the IAAT during the last years; the DAAD for sponsoring the trips to San Diego and Alicante; ESO for the inspiring observing run in La Silla; ADS for their extremely helpful publications data base; the HEASARC for access to archival *RXTE* data and providing software; CDS/Simbad for their astronomical databases, and LEO for their online dictionary.

Last but not least I want to dearly thank my parents for enabling me to study physics/astronomy and supporting me in any conceivable way.

Curriculum Vitae

11. June 1972	born in Weingarten, Germany
09.1978 – 06.1982	Elementary school Dormettingen/Dotternhausen
09.1982 – 06.1991	Gymnasium (High School) Balingen
06.1991	Abitur (High School Graduation)
10.1991 – 09.1997	Eberhard-Karls Universität Tübingen major: physics
07.1996 – 07.1997	preparation of the Diploma-Thesis: “Beobachtungen von Vela X-1 mit RXTE” under the supervision of R. Staubert at the IAAT
09.1997	Diploma
10.1997 – 12.1997	Scientific Co-Worker at the IAAT
01.1998 – 10.1998	Military Service (German Air Force)
11.1998 – 09.2003	Scientific employee at the IAAT (part time)
11.1998 – 04.2004	Preparation of this thesis entitled “X-ray spectra of highly magnetized neutron stars in binary systems” under the supervision of R. Staubert at the IAAT
10.2003 –	Scientific employee at the IAAT (full time) SPI instrument specialist at the ISDC

Awards:
Ehrenmedaille der Bundeswehr (Medal of Honor of the German Army)

My academic teachers have been the professors and lecturers:

Applied Physics : K.-H. Gaukler, E. Kasper, E. Plies, R. Schief
Astronomy : M. Bässgen, R. Hanuschick, H. Mauder, T. Richtler, H. Ruder, R. Staubert, J. Wilms
Chemistry : H. Ebert, J. Strähle
Experimental Physics : M. Baumann, H. Clement, F. Gönnenwein, W. Hartmann, R. Hübener, O. Lutz, A. Schwenk, G. Wagner
Mathematics : H. Fischer
Theoretical Physics : H. Pfister, H. Reinhardt, H. Stumpf

Lebenslauf

11. Juni 1972	geboren in Weingarten
09.1978 – 06.1982	Grundschule Dormettingen/Dotternhausen
09.1982 – 06.1991	Gymnasium Balingen
06.1991	Abitur
10.1991 – 09.1997	Eberhard-Karls Universität Tübingen Studiengang: Physik Diplom
07.1996 – 07.1997	Anfertigung der Diplomarbeit “Beobachtungen von Vela X-1 mit RXTE” unter Anleitung von R. Staubert am IAAT
09.1997	Diplom
10.1997 – 12.1997	Wissenschaftlicher Angestellter (Teilzeit) am IAAT
01.1998 – 10.1998	Grundwehrdienst
11.1998 – 09.2003	Wissenschaftlicher Angestellter (Teilzeit)
11.1998 – 04.2004	Anfertigung der Dissertation “X-ray spectra of highly magnetized neutron stars in binary systems” unter Anleitung von R. Staubert am IAAT
10.2003 –	Wissenschaftlicher Angestellter am IAAT, entsandt als SPI Instrument Spezialist an das ISDC, Genf

Auszeichnungen:
Ehrenmedaille der Bundeswehr

Meine akademischen Lehrer waren:

Angewandte Physik : K.-H. Gaukler, E. Kasper, E. Plies, R. Schief
Astronomie : M. Bässgen, R. Hanuschick, H. Mauder, T. Richtler, H. Ruder, R. Staubert, J. Wilms
Chemie : H. Ebert, J. Strähle
Experimentalphysik : M. Baumann, H. Clement, F. Gönnenwein, W. Hartmann, R. Hübener, O. Lutz, A. Schwenk, G. Wagner
Mathematik : H. Fischer
Theoretische Physik : H. Pfister, H. Reinhardt, H. Stumpf